Author:
Yue, Keren

Title:
Soft robotics technologies to treat laryngeal disorders

Soft robotics technologies to treat laryngeal disorders

By

KEREN YUE

Department of Engineering Mathematics
UNIVERSITY OF BRISTOL

A dissertation submitted to the University of Bristol in accordance with the requirements of the degree of DOCTOR OF PHILOSOPHY in the Faculty of Engineering.

NOVEMBER 2019

Word count: 36155

Abstract

Laryngeal disorders may be caused by infection, stroke and injury from surgery or trauma. The condition can be extremely uncomfortable and, in extreme cases, life threatening. Symptoms include hoarseness, shortness of breath, pain in the throat and dangerous aspiration of food and liquids. The discomfort, difficulties in coughing and changes in voice quality can have a significant negative impact on quality of life.

To address the limitations of current surgical and non-surgical solutions, this research aims to investigate new soft robotic solutions for treating severe laryngeal disorders such as vocal fold paralysis, as well as to improve quality of life after surgery such as laryngectomy. This thesis establishes a paradigm for future studies in the development of medical devices for respiratory support and presents four main contributions:

Firstly, a respiratory simulator was designed and built to simulate human breathing and coughing. This simulator provides a powerful platform to advance the development of novel treatments, prostheses and therapies. The comparison between physiological values of breathing and coughing and the values achieved utilising the respiratory simulator shows that the latter is able to accurately reproduce peak flow rates and volumes.

Secondly, a novel assistive coughing device, CoughAid, was developed to mimic the function of the glottis and trachea in the upper respiratory system. Experimental results show a significant increase in peak cough flow rate and peak cough pressure among 33 control participants using CoughAid. Preliminary results with a smaller cohort of post laryngectomy patients show improvement in peak cough pressure using CoughAid. Applications of CoughAid include simulation of vocal folds and respiratory conditions, and as a test-bed for the development of medical devices for respiratory support.

Thirdly, the physiology of vocal folds was studied, which identified that the kinematics of vocal folds and their associated cartilages are not well understood in the literature. A motor-controlled mechanical model of the arytenoid cartilage was designed and built for the visualization of vocal folds movement. Artificial vocal folds using soft material were fabricated for benchtop testing of assist device prototypes without cadaver or animal models.

Lastly, soft fluid-driven actuators were investigated to provide a potential soft actuating method in the human body. A bellows-shaped single balloon actuator was fabricated and tested in a pig larynx to quantify forces that are required for vocal fold adduction. Novel bistable balloon actuators were designed and prototyped which exploit the snap-through phenomenon. These were experimentally characterised in pressurized chambers and demonstrated controllable and stable actuation in tissue substitutes.

Dedication and acknowledgements

I would like to first thank my supervisors, Prof. Jonathan Rossiter and Dr. Andrew Conn, for the constant encouragement and guidance throughout the last four years. I would also like to thank my collaborators from UCL and from within the SoftLab, for inspiring me with ideas and providing assistance when I needed them.

I would like to dedicate this thesis to my parents, for their love and supports throughout the years.

AUTHOR'S DECLARATION

I declare that the work in this dissertation was carried out in accordance with the requirements of the University's Regulations and Code of Practice for Research Degree Programmes and that it has not been submitted for any other academic award. Except where indicated by specific reference in the text, the work is the candidate's own work. Work done in collaboration with, or with the assistance of, others, is indicated as such. Any views expressed in the dissertation are those of the author.

SIGNED: .....KEREN YUE..... DATE: .....11/11/2019.....

TABLE OF CONTENTS

List of Tables

Table **Page**

List of Figures

CHAPTER 1

INTRODUCTION

This thesis investigates the importance of vocal folds in the upper respiratory system, by considering two scenarios: vocal folds paralysis treatment and post-laryngectomy care, and exploring potential ways to improve current treatments by utilising soft robotics technologies.

1.1 Research motivation

Vocal fold paralysis (VFP) (Figure 1.1, on the left) is a laryngeal disorder where one or both sides of the vocal folds are immobilised. Possible causes could be surgical trauma, stroke, tumor, infections or neurological disorders [27, 28, 29]. Patient who suffer from this condition typically experience reduced voice quality, shortness in breath, chronic coughing and swallowing difficulties that impact their quality of life. The most common type of vocal fold paralysis is unilateral vocal fold paralysis (UVFP) [30]. Current treatments of UVFP include voice therapy, vocal fold injection, medialization thyroplasty and nerve-reinnervation, among which medialization thyroplasty is the most performed surgical procedure. This is done by pushing the paralysed vocal fold towards the midline by the insertion of an implant made from a silicone elastomer such as silastic, Gore-Tex or titanium. Limitations arise from this procedure include the static altering of the glottal gap, therefore the resulting voice quality is still limited, and breathing difficulties that due to the reduced airway.

Total laryngectomy (Figure 1.1, on the right) is a procedure that involves the removal of the entire larynx and the upper tracheal cartilage rings [31]. It is indicated for the curative treatment of laryngeal cancer where the tumour is considered to be too advanced for radiotherapy or partial resection. Cancer Research UK statistics reported around 11,900 new cases of head and neck cancers yearly between 2014-2016, and around 2,400 new cases of laryngeal cancer each year [32].

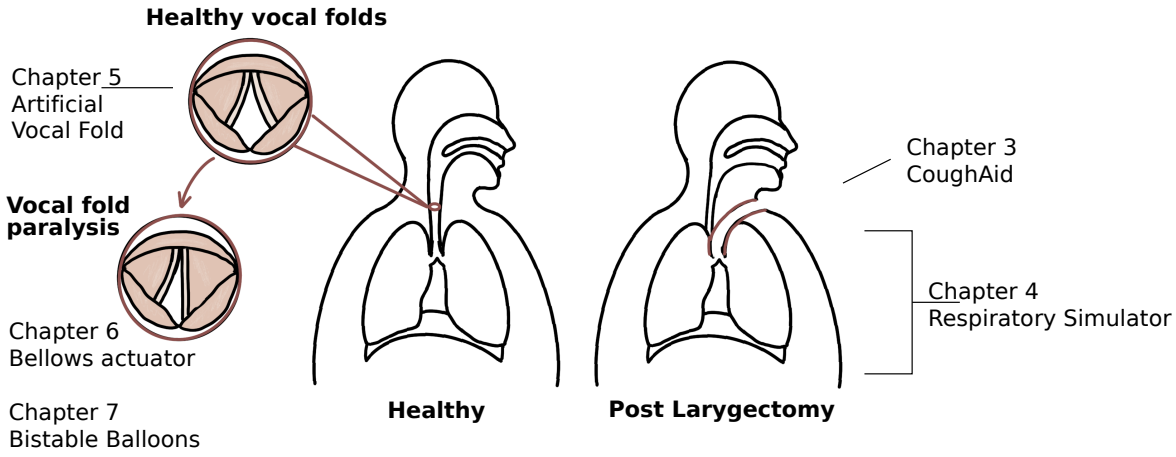

Figure 1.1: Illustration of thesis structure.

Although this type of cancer is considered to be rare, the after-care treatment still remains a great concern for patients. In a study carried out by Ganly et al., 40% of patients developed postoperative complications such as local complications, swallowing and airway problems etc [33]. The absence of the glottis in post-laryngectomy patients, and the direct exit of the trachea through the stoma, causes reduced cough efficiency. This can have a serious impact on patients' quality of life, and inevitably increasing health care costs. Current cough argumentation methods generally fall into three categories: Mechanical insufflation-exsufflation (MI-E) technique, Intermittent positive-pressure breathing (IPPB) devices and manually assisted coughing (MAC). Although these devices can effectively increase cough efficiency, they have limitations in immediate cough relief and lack personalised control and portability. Additionally, most of the current devices are used in primary care settings and there is consequently a large unmet need for cough assist devices in secondary and at-home care.

To address these limitations, We conduct research in this thesis through two parallel routes: firstly, our aim is to understand the problem from first principle, by studying the physiological structure in upper respiratory airway, aiming to find new novel solutions; secondly, we explore ways to make prototype devices that can directly address the limitations of current technologies. We approach this by exploiting a mixture of conventional rigid robotics control and soft robotic technologies. In Chapter 3: CoughAid and Chapter 4: Respiratory Simulator, where precision control is needed, we used conventional rigid robotics methods. Subsequently, in Chapter 5: Artificial vocal folds and Chapter 6: Bellows actuator, we utilise soft robotic technologies using soft, compliant and biocompatible materials. The softness and shape-changing abilities of these structures safely bridges the gap between robot and humans. In contract, the hard-soft interfacing that results from the implantation of rigid materials often causes problems. In Chapter 7: Bistable balloons, we explore a potential soft actuation method to address two of the important challenges

facing soft robotics: the development of soft pumps and the improvement of actuation method. Figure 1.2 shows a flow diagram of the development of the main chapters and Figure 1.3 shows the simulators and devices developed in this research.

The user base for the proposed solution also includes stroke sufferers, where a loss of laryngopharyngeal control results in difficulties in swallowing, vocalisation and coughing. Approximately 800,000 people per year (USA) have strokes and 23%-50% of these suffer dysphagia [34]. In addition, between 118,000 and 166,000 patients (USA pa) undergo thyroidectomy per year with at least 4%experiencing laryngeal nerve injury [35]. Up to 10,000 further patients suffer fold paralysis from idiopathic, traumatic and neoplastic causes. By extrapolation, these figures equate to 45,000 potential users in the UK per annum. The per-patient post-thyroidectomy cost is at least £2,000 pa [36] and the estimated cost to the NHS alone of treating the target group is £90M p.a. Societal costs including loss of jobs and social lives means overall impact is even greater.

The main aims of this thesis are as follows:

Main aims

1. Building a device that can help post-laryngectomy patients better clear their airways, and investigate the importance of glottal closure in coughing.
2. Build a physical platform to model the mechanism of the respiration system, with a focus on the upper respiratory tract.
3. Design a soft valve that can replicate the size and functionality of vocal folds.
4. Design and fabricate a fluidic elastomer actuator that addresses the current limitations in treating unilateral vocal fold paralysis.
5. Propose and test a new bistable soft actuation method for implantation in living organisms.

1.2 Thesis structure

This thesis contains 9 main chapters and 2 appendix chapters:

- Chapter 1 introduces the main aims and gives an overview of this thesis.
- Chapter 2 reviews the anatomy of larynx, the causes and treatment of vocal folds paralysis and the use of soft robotic technologies in medical applications.
- Chapter 3 presents a novel assistive coughing device, CoughAid, that can improve cough efficiency in people who have undergone laryngectomy.

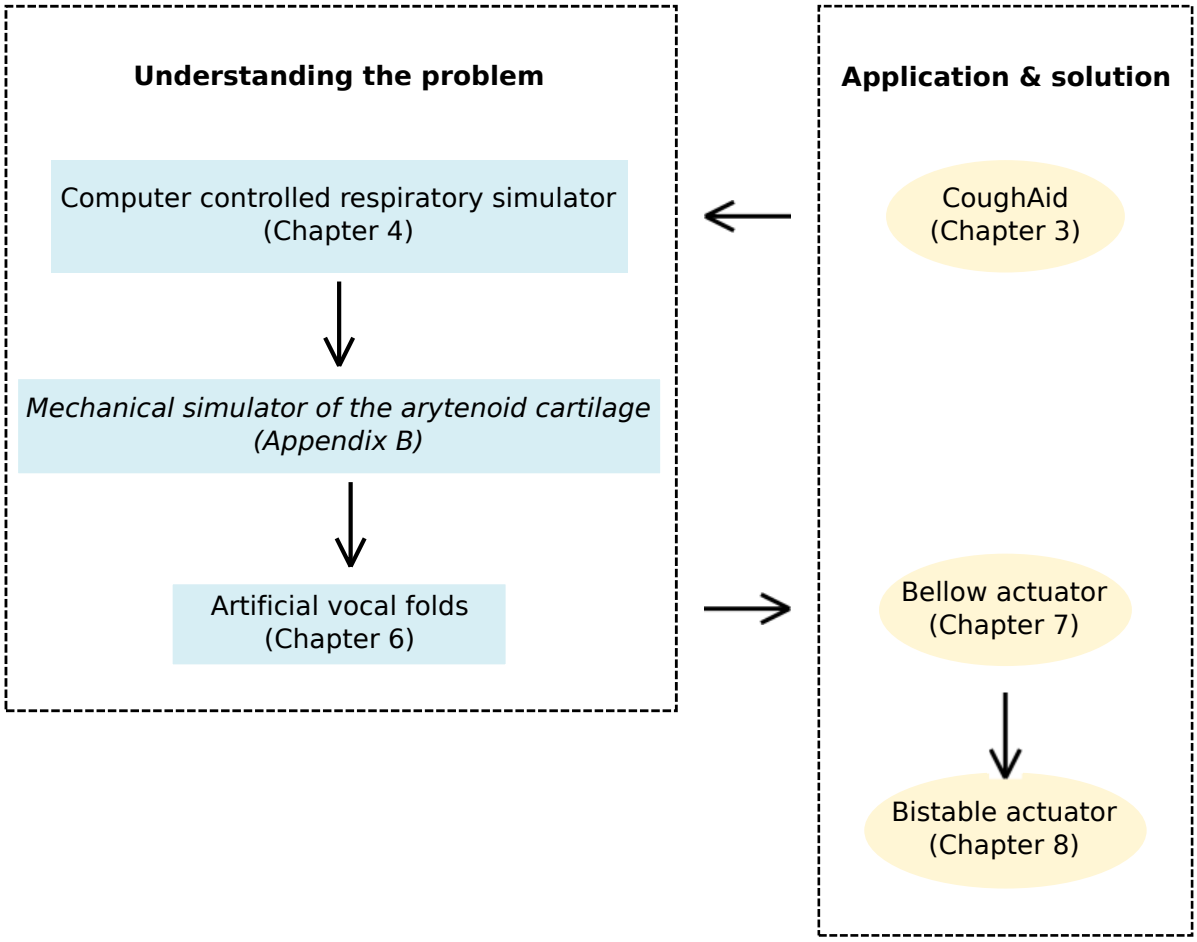

Figure 1.2: Thesis structure flow chart.

- Chapter 4 presents a computer-controlled respiratory simulator that can reproduce key characteristic of human breathing and coughing.
- Chapter 5 describes preliminary analysis on a pneumatically actuated soft valve that was designed and fabricated, inspired from the shape and function of vocal folds.
- Chapter 6 illustrates the design and fabrication of a pneumatically actuated bellow actuator which can effectively close the vocal folds of a pig larynx.
- Chapter 7 proposes a novel bistable fluidic elastomer actuation method harnessing snap-through instabilities in hyperelastic materials that allows distance control, using flat condom membranes, latex balloons and catheters.
- Chapter 8 concludes the thesis, identifies contributions and addresses future developments.
- Appendix A shows the design specifications of the respiratory simulator 1.0

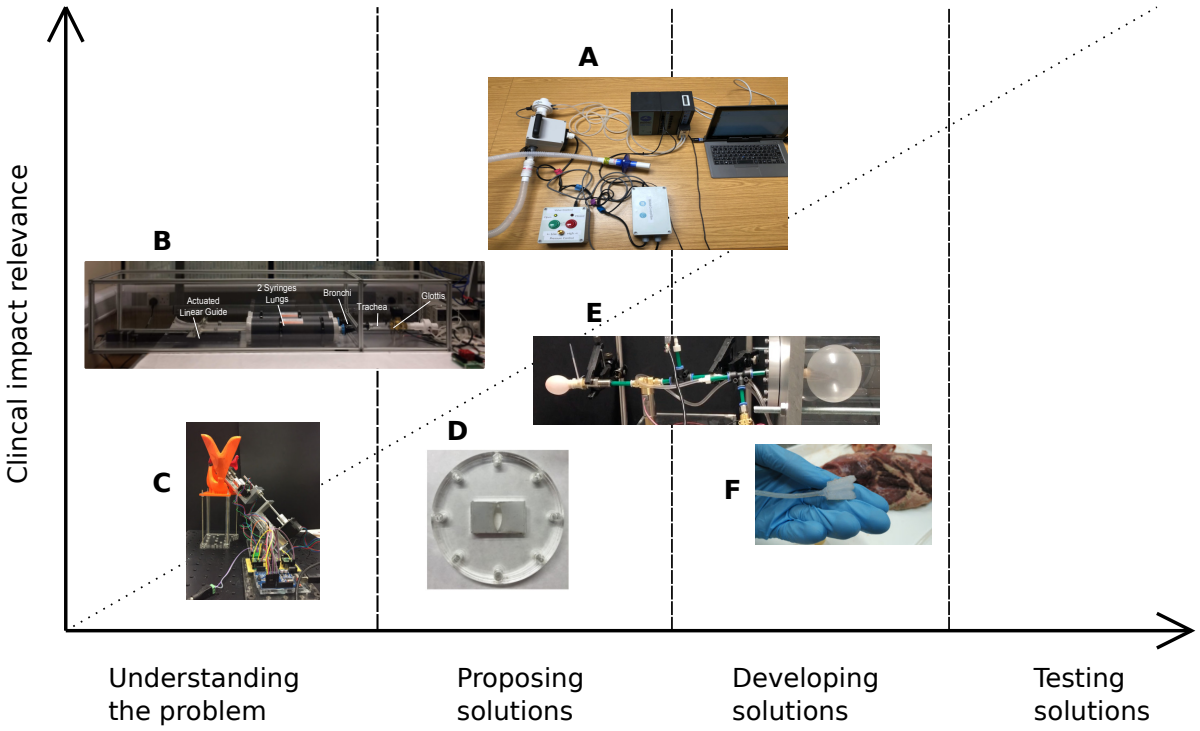

Figure 1.3: Simulators and devices developed in this thesis with regard to clinical relevance. A: CoughAid (Chapter 3), B: Respiratory simulator (Chapter 4), C: Mechanical simulator of arytenoid cartilage (Appendix B), D: Artifical vocal folds (Chapter 5), E: Bistable balloons actuator (Chapter 7), F: Bellows actuator (Chapter 6).

- Appendix B investigates the action of the arytenoid cartilages, the cartilages that are directly involved in the movement of vocal folds, through the design and fabrication of a mechanical simulator.

1.3 Publications arising from this research

[37] M. E. GIANNACCINI, K. YUE, J. GRAVESTON, M. BIRCHALL, A. CONN, AND J. ROSSITER, Respiratory simulator for robotic respiratory tract treatments, in 2017 IEEE International Conference on Robotics and Biomimetics (ROBIO), IEEE, 2017, pp. 2314–2319

CHAPTER 2

LITERATURE REVIEW

This chapter introduces the background and fundamental concepts that will be used throughout this thesis. It will begin with the introduction of the morphological and physiological background on the larynx, where we describe the nerves, muscles and cartilages that are involved to enabling the functioning of vocal folds. We will then introduce vocal fold disorders with a focus on vocal fold paralysis as the fundamental problem this thesis addresses. This will include pathology of vocal folds paralysis, current treatments and prognosis, and the challenges faced that are yet to be solved. Finally we discuss the development of medical implants over the past decades and how soft robotics have been integrated to explore new ways of actuation in human body.

2.1 Larynx

The larynx, also commonly known as the voice box, is situated in the neck of amphibians, reptiles, and mammals. It is critical for breathing, phonation, swallowing and coughing. It houses the vocal cords (also called vocal folds), which are situated just below the point where the tract of the pharynx splits into the trachea and the esophagus as can be seen in Figure 2.1. The vocal cords adduct (close) and vibrate for speech and phonation, and abduct (open) when breathing. These motions are regulated by nerves, of which the hierarchy is shown in Figure 2.5. The abduction and adduction of the vocal cords are controlled via two branches of vagus nerve shown in Figure 2.4, namely the recurrent laryngeal nerve (RLN) and the superior laryngeal nerve (SLN), and fulfilled by the movement of 6 laryngeal cartilages and 5 intrinsic laryngeal muscles.

Laryngeal cartilages include 3 unpaired cartilages: epiglottis, thyroid cartilage, cricoid cartilage; and 3 paired cartilages: arytenoid cartilages, corniculate cartilages and cuneiform cartilages. The shape of each cartilage is shown in Figure 2.2. The epiglottis is a leaf shaped plate of elastic cartilage which is situated at the root of the tongue, with its end attaching to the back of the

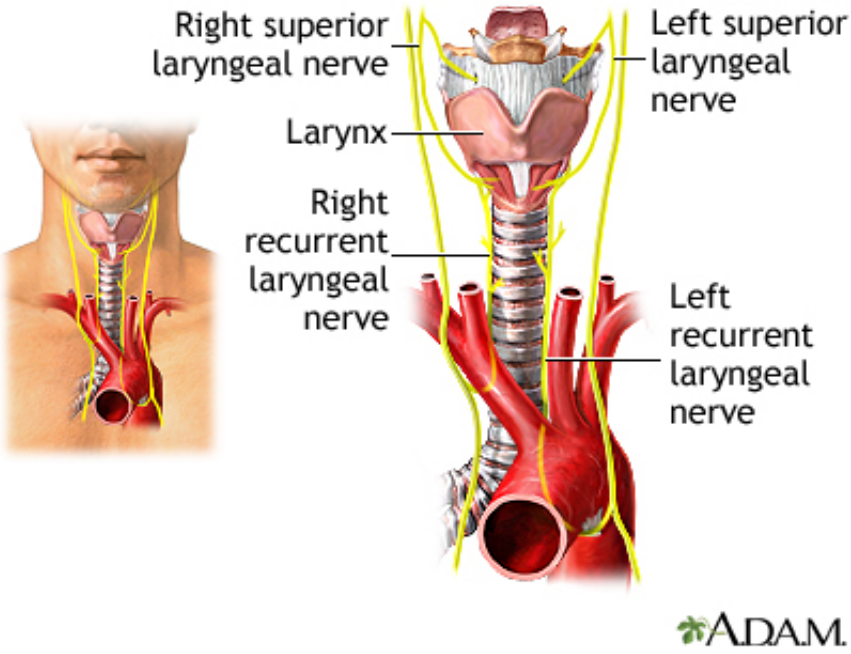

Figure 2.1: Structure of a larynx. Figure reproduced from [8].

thyroid cartilage. During swallowing, the epiglottis folds back to cover the larynx and prevent aspiration [38]. The thyroid cartilage locates between epiglottis and cricoid cartilage. It is largely encircles the vocal folds. The inferior surface of the thyroid cartilage articulats with the cricoid cartilage. The criocoid cartilage has a complete ring shape, attaches to the inferior of the thyroid cartilage and its ligaments at the inferior end attach to the first ring of the trachea. The superior surface of the cricoid cartilage articulates with two arytenoid cartilages mounted on the cricoid ring. The intrinsic laryngeal muscles consist of 5 muscles: posterior cricoarytenoid (PCA), lateral cricoarytenoid (LCA), thyroarytenoid (TA), cricothyroid (CT) and interarytenoid (IA) muscle, where IA contains transverse and oblique muscle components . PCA are paired muscles which connect posterior cricoid cartilage to arytenoid cartilage. They are the only muscles responsible for opening the vocal folds and achieve this by rotating the arytenoids laterally [39]. LCA connect the lateral cricoid to the muscular process of the arytenoid, and close the vocal folds by rotating the arytenoids medially. TA is a thin muscle that forms part of the vocal folds, which shortens and relax the vocal folds by moving the arytenoids towards the thyroid cartilage. CT attach to the lateral cricoid cartilage side. CT is the only muscle to aid phonation by elongation and tensioning vocal folds [40, 39]. This is done by tilting the cricoid ring anterior. IA situates at the posterior side of the arytenoids, and aids the adduction of vocal folds [41].

As illustrated in Figure 2.5, the RLN control all intrinsic muscles of the larynx except for the CT, which is innervated by the SLN. The RLN carry sensory information from the mucous membranes of the larynx below the lower surface of the vocal fold, and are responsible for

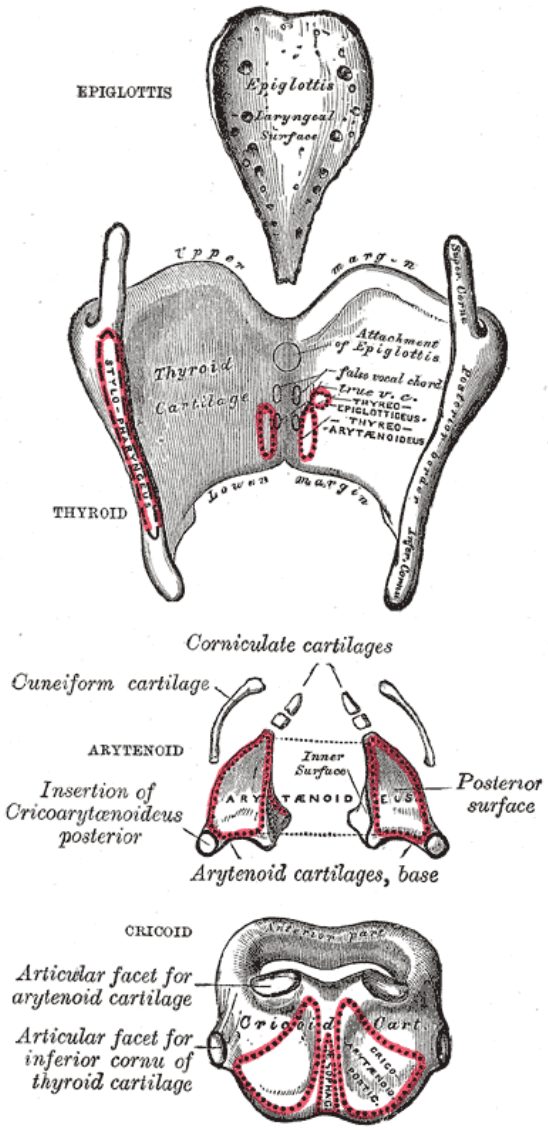

Figure 2.2: The cartilages of the larynx. Posterior view. Figure reproduced from [9]

motor input to the vocal folds [42, 43], whereas the SLN carries sensory information from the membranes of the larynx above the vocal folds.

2.2 Vocal Fold Paralysis

Vocal cord paralysis or paresis is the total or partial interruption of nerve impulse resulting in no movement or weak movement of laryngeal muscles. The paralysis can be unilateral or bilateral and may involve the abnormal function of RLN, SLN or both nerves [44]. Symptoms of RLN paralysis are usually hoarseness in voices, throat pain, shortages of breath as well as aspiration of food/drink,glottal insufficiency and changes in voice pitch. Symptoms from SLN

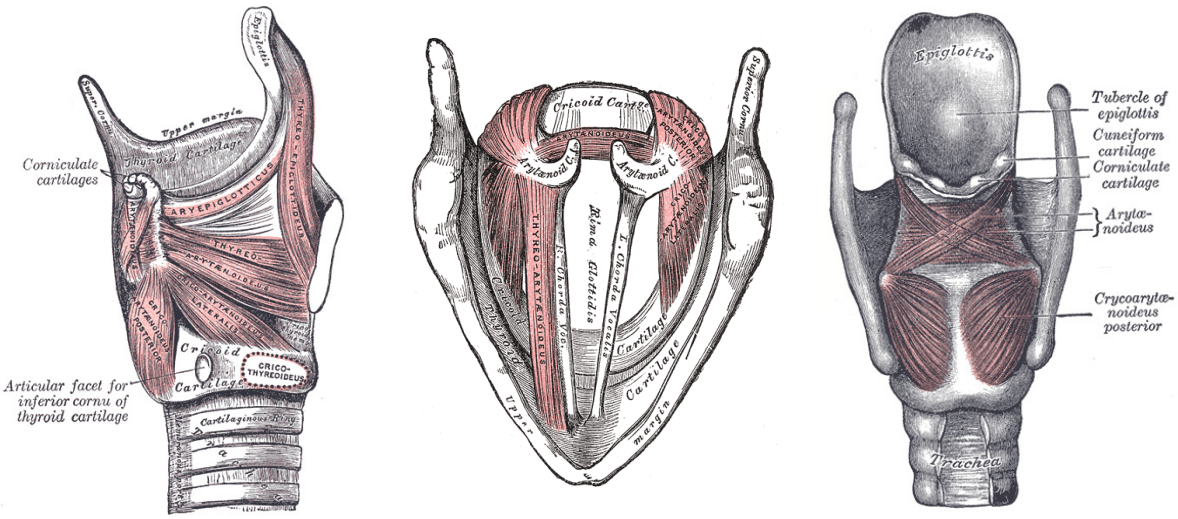

Figure 2.3: Side, anterior and posterior views of the larynx, illustrating the positions of laryngeal muscles. Figure reproduced from [9].

Position of vocal fold	Distance from midline(mm)	Diagnose
Median	Midline	RLN paralysis
Paramedian	1.5	RLN paralysis
Intermediate	3.5	RLN + SLN parlaysis
Gentle abduction	7.5	Paralysis of adductors
Full abduction	9	N/A

Table 2.1: Position of paralysed vocal folds from the midline.

paralysis are swallowing difficulties, chronic coughing, pain from vocal use and loss of voice in high pitch ranges [45, 46, 47]. The left RLN is found to be more prone to paralysis because it has a much longer course as compared to the right RLN as can be seen from Figure 2.4. A bilateral paralysis will cause impaired air flow through vocal folds, result in breathing difficulties depends on the position of pluralisation. Figure 2.6 shows a comparison between the movement of healthy and paralysed vocal cords during respiration and phonation.

The paralysed vocal fold may be immobilized in various positions: median, paramedian (most frequent position) or, less often, intermediate or lateral [44]. The distance of each positions to the midline of vocal folds is tabulated in Table 2.1.

The most widely accepted theory, developed by Wagner and Grossman, states that in complete paralysis of the recurrent laryngeal nerve the cord lies in the paramedian position because the intact cricothyroid muscle adducts the cord. If the superior laryngeal nerve is also paralysed the cord will assume an intermediate position because of the loss of adductive force [48].

The paralysed vocal cords may be flaccid but in most cases rigid, or become rigid over time, because the muscle tension is maintained. The reason is believed to be an undirected regrowth of the nerve from the site of the injury to the inner larynx muscles. This usually provides tension in

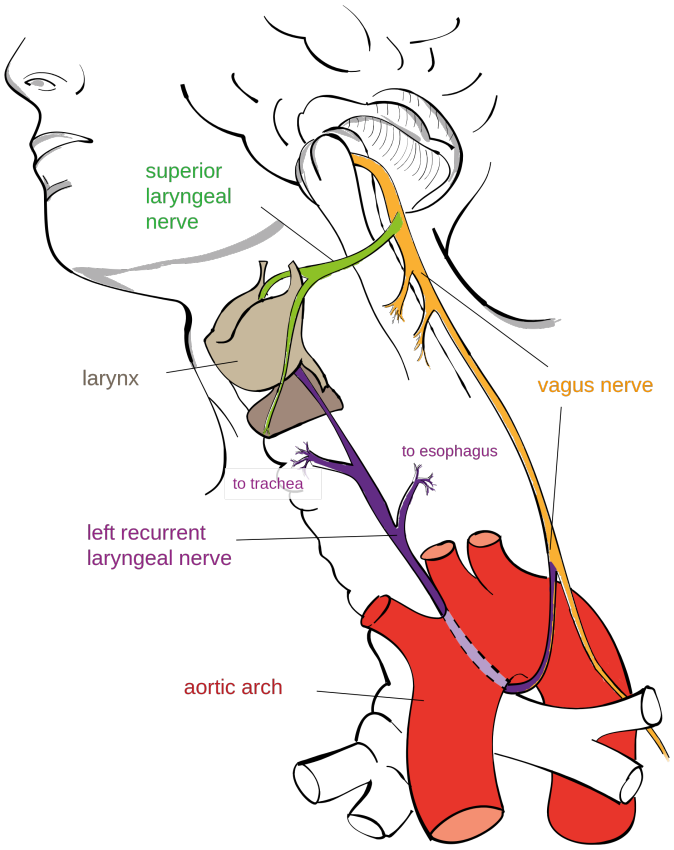

Figure 2.4: Drawings showing the course of SLN and RLN. Figure reproduced from [10].

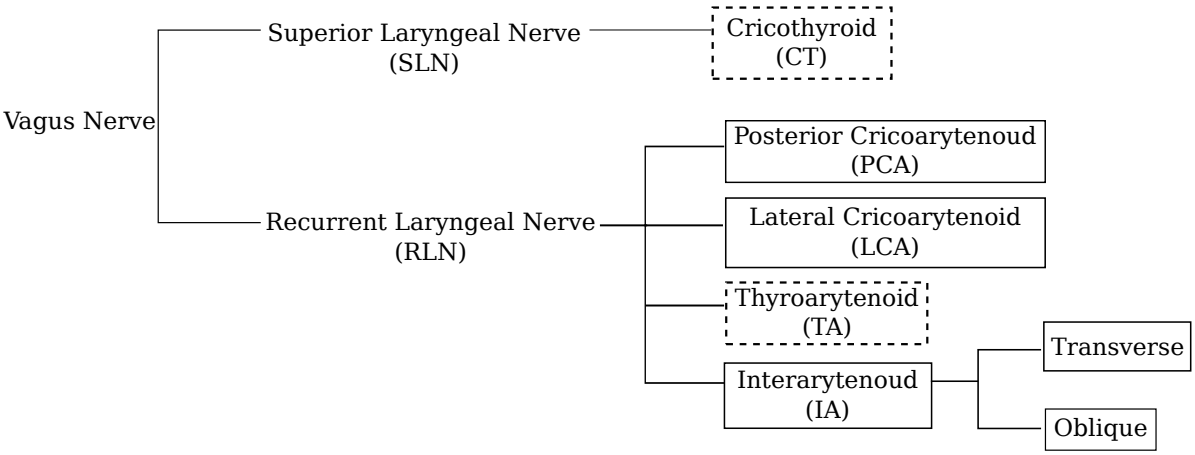

Figure 2.5: Nerves controlling the motion of vocal folds. Dashed boxes show muscles for pitch altering, and solid boxes show muscles for the opening and closing of vocal folds.

the muscles but does not lead to mobility of the vocal fold [49].

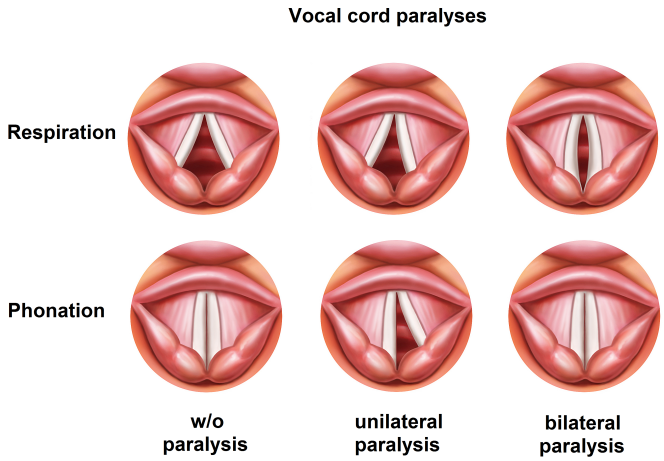

Figure 2.6: Illustration diagram of Vocal fold paralysis. Image reproduced from [11].

2.2.1 Causes

Causes of vocal folds paralysis could be either iatrogenic (illness caused by medical examination or treatment) or idiopathic (disease or condition which arises spontaneously or for which the cause is unknown). Previous case studies show the most common iatrogenic etiology was surgical trauma, others include non-laryngeal malignancy, stroke, external neck trauma and inflammation or scarring at cartilage joints. Among surgical trauma, thyroid surgery was the most reported cause [27, 28, 29].

2.2.2 Current Treatments

Depends on the causes of vocal fold paralysis, different treatments are used to treat the condition. These include voice therapy, vocal folds injection, phonosurgery and nerve-muscle pedicle (NMP) reinnervation. For bilateral vocal folds paralysis, if the vocal folds are paralysed at the midline and airflow is obstructed, tracheostomy is required. We will briefly discuss the procedures and identify challenges faced by each treatment in the following sections.

2.2.2.1 Voice therapy

The voice therapy is provided by speech and language therapists and aims to help patients improve their speech by exercising laryngeal muscles or leaning ways to control breath and pitch during speech. It could be the only treatment needed for some vocal fold paralysis cases as the vocal folds can recover and resolve its functions over 6 months to one year; or it could be combined with surgical procedures to help the patient improve speech after surgery.

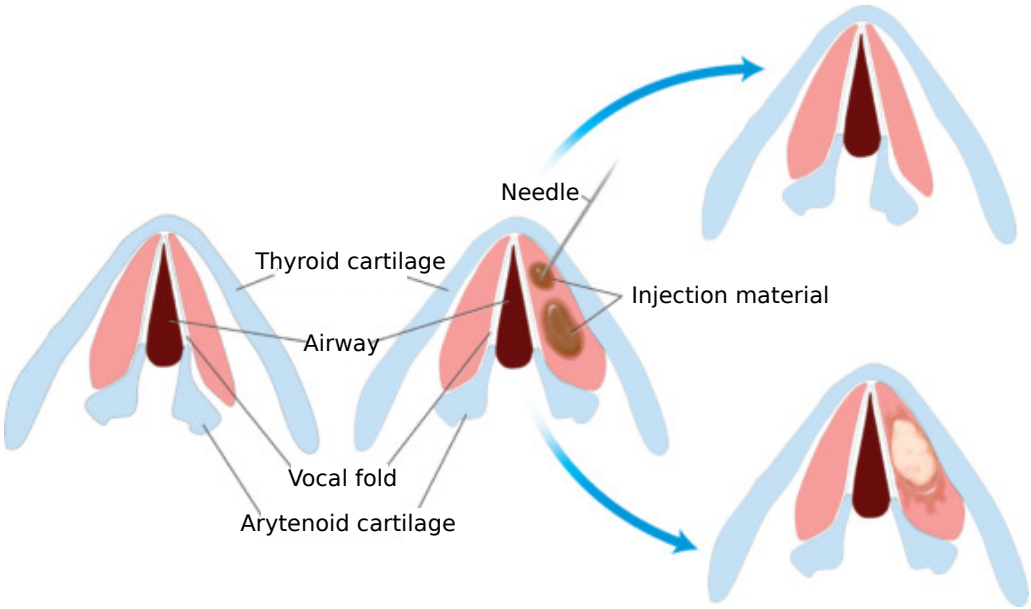

Figure 2.7: Illustration of the vocal fold injection procedure, image reproduced from [12]

2.2.2.2 Vocal folds injection

Vocal fold injection (VFI) is a procedure intended to medialise the vocal folds. It could be temporary or permanent and involves a deep injection of soft materials into the lateral thyroarytenoid or lateral cricoarytenoid muscle using a laryngeal needle, which then pushes the vocal folds to the middle and corrects for glottal insuffciency. This procedure, as shown in Figure 2.7 serves a similar purpose to type 1 thyroplasty (medialisation thyroplasty), but is usually only feasible for glottic gaps up to 3mm [50].

Materials used for temporary injection include hyaluronic acid (Restylane™, Hyalaform™, Juvederm™), bovine-based collagen(Zyplast™), human based collagan (Cymetra™)), tissue engineered human based collagen (Cosmoplast™, Cosmoderm™), bovin-based gelatin (Gelfoam™, Surgifoam™) and sodium carboxymethylcellulose (CMC) (Radisse Voice gel™). Temporary injection could last 1-6 months, and is suitable for situations in which paralysis may be temporary, with patients for whom an open operative procedure must be delayed, or in circumstances where it is desirable to determine the effect of vocal cord injection prior to placement of non-absorbable material.

Materials used for long-term vocal fold injection include silicone polymer polydimethylsiloxane (PDMS) (Bioplastique™), autologous fascia, autologous fat, CaHA (calcium phosphorus in the form of microspheres in a gel carrier) (Radiesse™), polytetrafluoroethylene (Teflo™). These materials can lasts from 2-10 years although absorption could happen during the course, therefore over-injection is generally required in the surgery.

One main advantage about vocal fold injection is that the procedure could be carried out in office while patient remains awake at the whole time. This provide real-time feedback on the

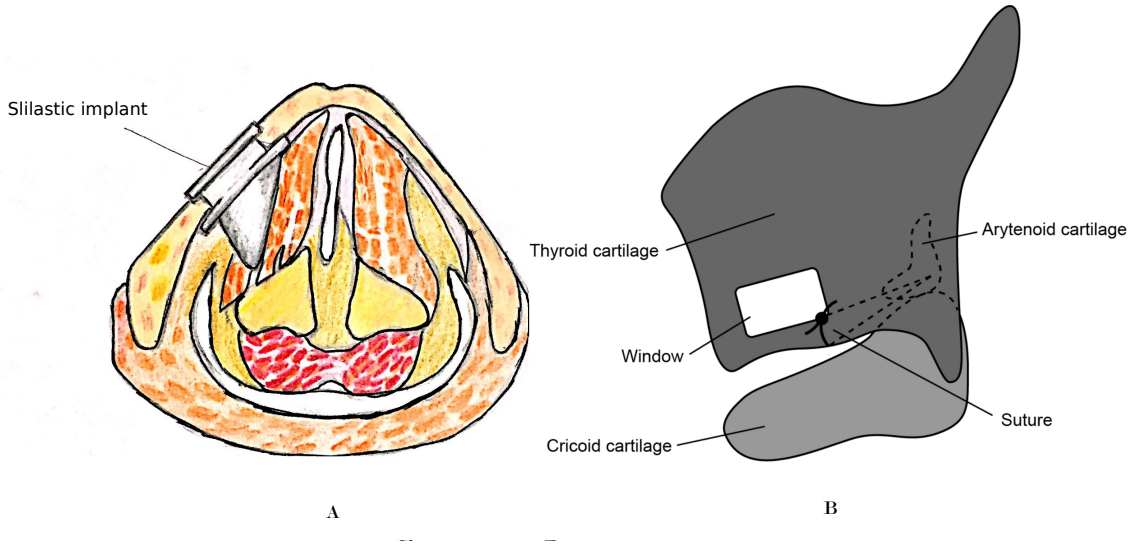

Figure 2.8: Images of the medialization procedures. A: Thyroplasty, image reproduced from [13]. B: Arytenoid adduction, image reproduced from [14].

glottal closure during injection and thus provide promising prognosis results with the aid of voice therapy.

2.2.2.3 Medialization Thyroplasty

Medialization thyroplasty (also known as type 1 thyroplasty) is the most performed procedure for unilateral vocal fold paralysis. It involves inserting an implant via a rectangular window cut on the thyroid cartilage, pushing the vocal folds towards midline. Materials used for implant including silicones such as silastic (Montgomery Thyroplasty Implant system), pure titanium (TVFMI system), hydroxyapatite (VoCoM system) and Gore-Tex (Gore-Tex Implant system). The procedure is done under local anaesthesia [51]. Arytenoid adduction (AA) is usually carried out in conjunction with type 1 thyroplasty, to provide further medialization of the posterior glottis. This is done by permanently suturing the arytenoid cartilage to the thyroid cartilage, which rotates the arytenoid and therefore closes the vocal folds [52]. Illustrations of the procedures are shown in Figure 2.8.

The main advantages of medialization thyroplasty are that it is reversible if not achieving desirable results and that the effect is long lasting.

2.2.2.4 Nerve-muscle pedicle flap implantation

Nerve-muscle pedicle (NMP) flap implantation is a nerve reinervation method that has shown promising results. Some patient do not respond well to thyrolasty. This could be because VFI, type 1 thyroplasty and AA all provide static medialization, such that the modified paralysed vocal fold does not move. As a consequence, the thyroarytenoid (TA) muscle remains static during

phonation, with no elongation and relaxation of vocal folds, and results in little contribution to voice production and pitch tuning. To restore the function of TA, clinical trials have been carried out using the NMP flap implantation method. In 1977, Tucker introduced the procedure of implanting NMP flap on lateral TA muscle through the thyroid window and was further shown to be effective by May et. al [53, 54]. Yumoto et al. implemented NMP flap implantation together with AA and showed excellent restoration of vocal function [55]. Comparing type 1 thyroplasty and NMP flap implatation methods, Paniello et al. concluded there is no significant difference, while in a recent study [56], Kodama et al. have shown significant improvement of maximum phonation time and regularity for vocal fold vibration, during over 12 months follow up period after AA combined with the refined NMP, as compared to patients who have undertaken type 1 thyroplasty [57].

The main advantage of this method is that it can restore some mobility in the paralysed vocal folds and therefore is now proposed as an alternative to the conventional type 1 thyroplasty and injection methods.

2.2.3 Limitations of current treatments

In the previous sections we introduced current treatments for unilateral vocal folds paralysis and some advantages in each of them. However, these treatments raise some common limitations.

First of all, the size of the conventional implants are fixed and they can be hard to fit optimally on individual cases. In vocal fold injection procedures, although direct feedback can be provided by patient phonation, over injection is usually required to prepare for the potential absorbtion of the material. In type 1 thyroplasty, although Montgomery and VoCoM both offer implants with varied sizes, it is still a challenge to achieve optimal alteration to the vocal fold position. Surgeons also customise the size of the implant by trimming the implant with a scalpel during surgery, but a more robust solution could be developed for more precise control of sizes of implants.

Secondly, most conventional surgical procedures only achieve static alteration of the position of the paralysed vocal folds, although some vibration function has been restored with the new nerve reinnervation method. But there is no movement in the lateral directions, and as such the glottis opening is limited, and can only be controlled by one side of the vocal folds. This could cause serious problems including difficulty in breathing.

Because of the challenges identified, we look into potential solutions that could aid the problems, by utilising soft robotics technologies.

2.3 Soft robotics technologies in medical applications

Soft robotics is a growing field derived from conventional robotics. It takes inspiration from living organisms for their fexible locomotion and ability to adapt to unpredictable surroundings, and explores new ways to construct robotic devices that are made from soft, compliant materials [58].

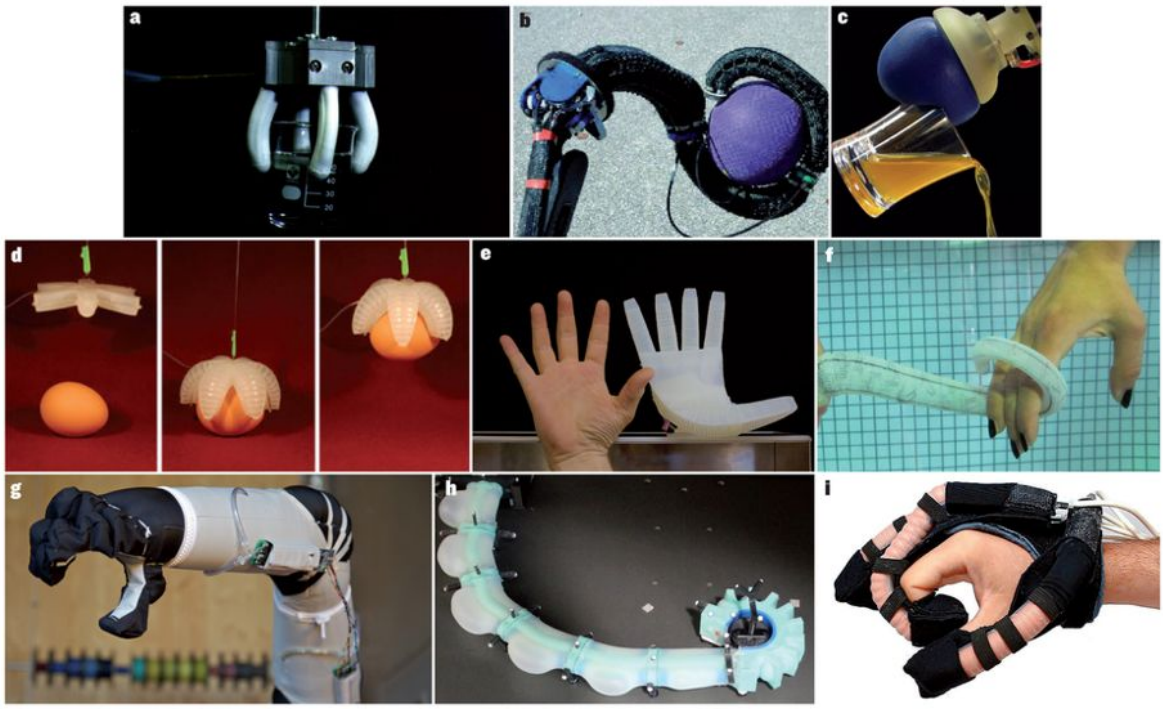

Figure 2.9: Examples of soft robots. Figure reprodecued from [15].

Some examples of soft robots are shown in Figure 2.9. The compliance and softness of soft robots have enabled research into the field of smart materials, smart sensors, energy harvesting, artificial muscles, smart actuators, soft transducers, soft matter computing and also medical applications, where biocompatibility and softness are attaractive properties for patient-robot interactions [59]. Figure 2.10 shows examples of the development in branches of soft robotics.

Among applications, medical technologies were advanced rapidly in the past decades, from open surgery to minimally invasive procedures (MIS), and from rigid tools to soft, more biocompatitable tools. Rigid medical devices have limitations in terms of flexibility and manoeuvrability, and are also at risk of causing damage or discomfort to human or animal tissue. This could be solved utilising soft materials. One example is the development of flexible endoscopic arms, equipped with multiple miniature tools on the tip, for the use in natural orifice transluminal endoscopic surgery (NOTES) [60]. Wearable devices are also developed using pneumatic artificial muscles for rehabilitation and assisted living, such as walking assistance [61], ankle–foot rehabilitation [62] and soft exosuits to assist human locomotion [63]. In-vivo devices have also been made utilising soft materials. Examples include a heart sleeve that made from artificial silicone muscles which uses compressed air to power, and can mimic the movements of the normal human heart [64]; drug delivery by an ice-encapsulated origami robot, made from biodegradable composite material sheets embedded with a drug layer, for delivery through the esophagus using magnetic fields [65]; robotic implant for the lengthening of esophagus to treat long-gap esophageal

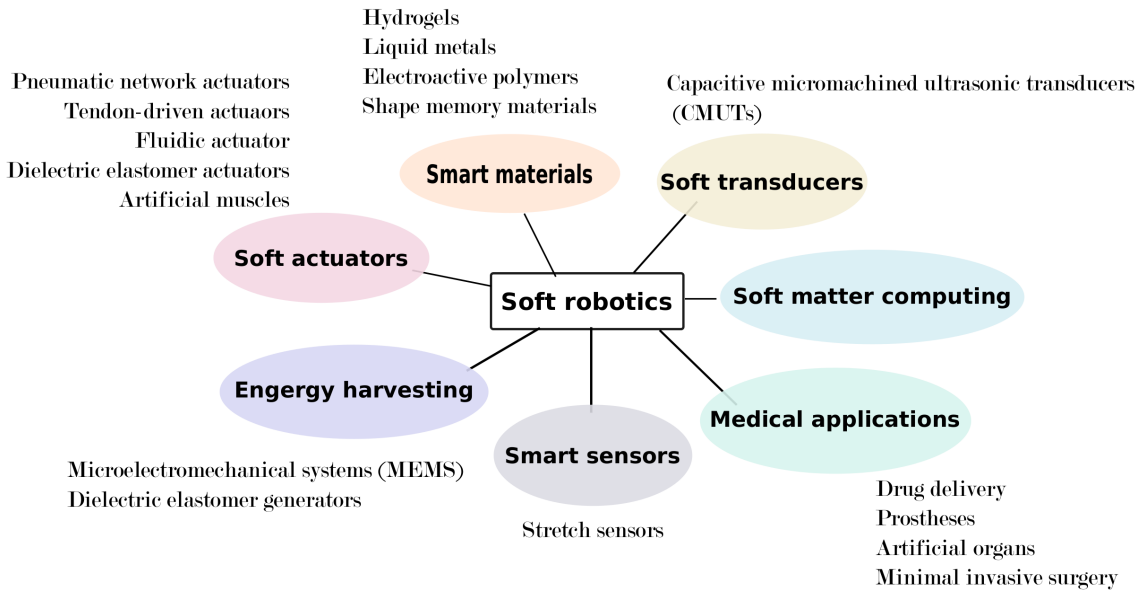

Figure 2.10: Soft robotics, its core techniques and its applications.

atresia [66]; soft shape memory alloy (SMA) valves to treat urethral sphincters by controlling the opening of urethra [67]; active catheters with embedded SMA actuation system [68] or by micro-fluidic actuation (FEAs) system in multiple segments [69] to ease their insertion through body, and many other applications utilising smart materials and structures.

However, soft medical devices have drawbacks. One main problem rises from the lack of precise force and displacement control and sensing abilities, as well as low force exertion [70]. Some applications can also be limited due to material properties, for example electroactive polymers (EAP) typically work under high voltage, which could be potantially dangerous for the human body, and SMAs dissipate high levels of heat energy when actuated and therefore need to be encapsulated. The portability of some of the mentioned medical devices is limited because of the need for external power source such as compressed air [71]. The hyperelastic materials used in many soft robotic devices display highly non-linear behaviours which can be difficult to model analytically and computationally expensive to model numerically (e.g using Finite Element Analysis, FEA), and the motion of the device may therefore be hard to predict [59, 15].

Nevertheless, the overall advantages exhibited in soft materials and soft robotics opens new opportunities for surgical solutions. Main advantages of soft materials in medical applications include often biocompatitable, they can be biodegradable, they have low cost and can be personalised using rapid prototyping. They can also achieve large shape change in a short period of time with relatively small input force and can adapt to uneven surfaces.These characteristics are much needed when approaching the challenges identified in this research; to investigate an implant that can be personalised in size and shape, and which can be actively actuated to aid

Challenges from current solution	**Proposed solution**	**Characteristics required**	**Technology to use**
Coughing incapabilities after laryngectomy	CoughAid (Chapter3)	Precise control	Rigid robotics
Coughing simulation with a focus on upper respiratory tract	Respiratory simulator (Chapter4)	Profile simulation	Rigid robotics
Visualise the movement of cartilages in larynx	Arytenoid simulator(Appendix B)	Motion control	Rigid robotics
Rigid valves are not biocompatable	Artificial vocal folds (Chapter5)	Soft, can be actuated, biocompatible	Soft robotics
Fixed size, static thyroplasty implant	Bellows actuator (Chapter6)	Size customisable and actuatable implant	Soft robotics
Power source are either rigid or cannot be use in body	Bistable balloons actuator (Chapter7)	Biocompatible, small input force, large volume change, snap through ability	Soft robotics

Table 2.2: Challenges addressing in each chapter.

vocal fold movement. As discussed in the previous section, the current implants used to treat vocal fold paralysis are available in limited sizes and are static (they are non-actuating). A soft robotic device could overcome these limitation: the shape changing property of soft structures can be exploited to ensure the implant fits to the patient and operating conditions, and the fluidic actuation methods that are widely used in soft robotics can be used to deliver a dynamic implantable device which adjusts to the physiology and needs of the patient. Actuation is explored in more detail in Chapter 6 and a new concept of bistable fluidic actuation is presented in Chapter 7. Bistable actuation can help to address the challenge of limited power supply capacity in medical implants. More detailed challenges are discussed in each chapter and strategies to tackle them are outlined in Table 2.2.

This thesis addresses the limitations and advantages of soft materials and contributes to the development of active and passively actuated fluidic soft robotic devices in medical applications.

CHAPTER 3

COUGHAID

This chapter presents an assistive coughing device (CoughAid) that can help post-larygectomy patients with airway clearance, which artificially controls the accumulation and exhalation of the lung pressure to replicate the function of the glottis during coughing. This is a collaborative research between University of Bristol (UoB) and University College London (UCL). I lead the research carried out in UoB, which include the design and manufacturing of CoughAid, conducting experiments with control group, participating in experiments with post-laryngectomy group lead by UCL, and analysing the results. UCL obtained the ethics approval for tests with a post-laryngectomy group, provided the BIOPAC data acquisition system, assisted with statistical analysis, and provided clinical insights on the topic.

In this chapter we first introduce the design and specification of CoughAid, then move on to experiment procedures with control and post-laryngectomy participants. Finally we analyse and discuss the results generated from both groups using CoughAid.

Main contributions

- Design and fabrication of an assistive coughing device, CoughAid.
- Development of the control algorithm enabling auto-data collection of the device.
- Conducting experiments in control post-laryngectomy participants which shown promising results and motivate future development of the CoughAid system.

3.1 Introduction

Total laryngectomy is a procedure that involves the removal of the entire larynx and the upper tracheal cartilage rings [31]. Post laryngecotomy patients are no longer at the risk of aspiration pneumonia, however some patients have difficulties in coughing.Coughing in healthy subjects, as can be seen from Figure 3.1a, typically involves three phases: inhalation, compression and exhalation [72]. In the inhalation phase, air is inhaled and expiratory muscles are engaged; In the compression phase, the glottis is closed, and expiratory muscles contract, allowing intrathoracic pressure to build up in the airway; In the exhalation phase, the glottis opens and a rapid exhalation follows [73]. Expiratory pressure and flow profiles during coughs are shown in Figure 3.2. Cough is vital for clearing excessive secretions in the airway. However, the absence of the glottis in post-laryngectomy patients, and the direct exit of the trachea through the stoma, causes reduced cough efficiency (Figure 3.1b), such that daily sputum production, coughing and the need for frequent forced expectoration are among the most common complaints made by patients [74]. Although some patients find limited relief through the use of heat and moisture exchangers, which condition inspiratory air and thereby treat pulmonary symptoms and aid stoma cleaning [75], the coughing ability of post-laryngectomy patients is far below healthy people.

Clinically there are many potential factors that can be used to assess cough efficiency. For example, maximal respiratory mouth pressure and coughing gastric pressure are typically used to assess the strength of expiratory muscles [76], which are associated with coughing effectiveness [77]. The effectiveness of a cough can also be affected by the adhesion and cohesion of mucus [78, 79]. By simulating cough flow rates using a pressurized chamber, the influence of rheological properties on mucus clearance have been investigated [80]. Mechanical experiments have also shown that increasing the pressure and flow rate improves mucus clearance [81], and that increases in expiratory flow and pressure can be achieved using mechanical assistance for patients with motor-neuron diseases [82]. Studies show for effective mucus expectoration, peak cough flow (PCF) must exceed 160 to 200 L/min [83, 84]. PCF above 250 to 270 L/min could prevent pneumonia in patients with neuromuscular disorders [84, 85]. For laryngectomised patients, a lack of signals arising from the larynx may result in a reduction of cough volume acceleration and the intensity of abdominal muscle contractions during a reflex cough. These factors may contribute to facilitate the onset and/or the persistence of chest infections [86].

Medical robotics has advanced rapidly through past decades, from surgical robots such as the da Vinci surgical system and surgical tools developed for minimal invasive surgeries, to rehabilitation exoskeletons and implantable robotics such as heart sleeves [64, 87] and drug delivery robots [88]. Despite this growth, there has been a dearth of research into robotics to assist respiratory conditions and, more specifically, cough insufficiency. Current cough argumentation methods generally fall into three categories: Mechanical insufflation-exsufflation (MI-E) technique such as Cough Assist, where a positive pressure is applied during inhalation and a fast negative

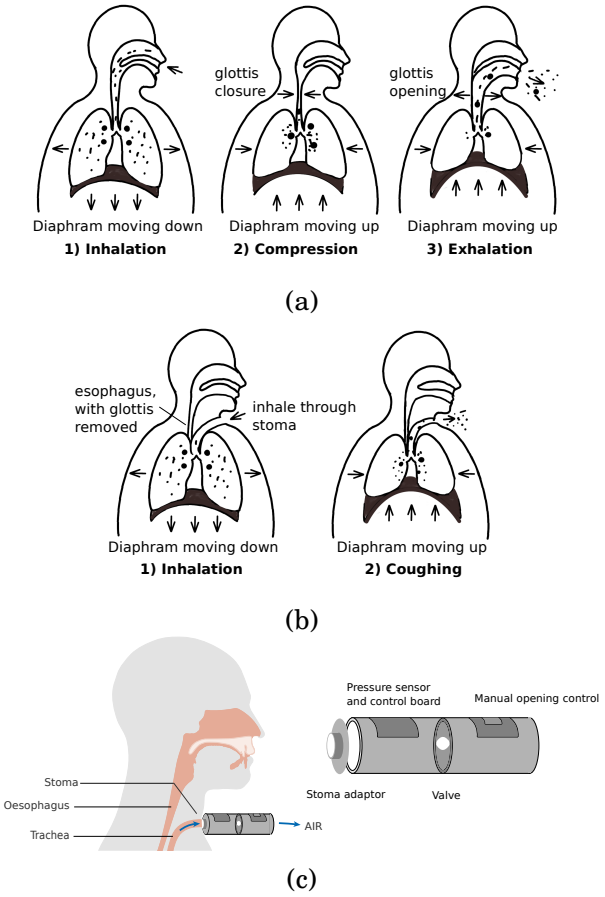

Figure 3.1: (a) Three phases of coughing in healthy people. (b) Coughing in laryngectomy patients is limited by the lack of a functional glottis. (c) Proposed cough assistive device.

pressure is applied for exhalation to improve cough, and rehabilitation devices to improve the cough flow [89]; Intermittent positive-pressure breathing (IPPB) devices which provide a constant positive pressure during the inhalation phase followed by a passive exhalation phase where the positive pressure returns to atmospheric, thereby improving cough capacity by increasing the inhalation volume [90]; and manually assisted coughing (MAC), where abdominal thrust or lateral costal compression is applied. Although these devices can effectively increase cough efficiency, they have limitated effect on immediate cough relief and lack personalised control and portability. Additionally, most of the current devices are used in primary care settings and there is consequently a large unmet need for cough assist devices in secondary and at-home care.

To overcome these limitations, we propose a comfortable, wearable prototype portable device (Figure 3.1c) to improve cough sufficiency. In this chapter a preliminary design of the CoughAid coughing device, that mimics the function of the glottis in the respiratory system, was built and tested.

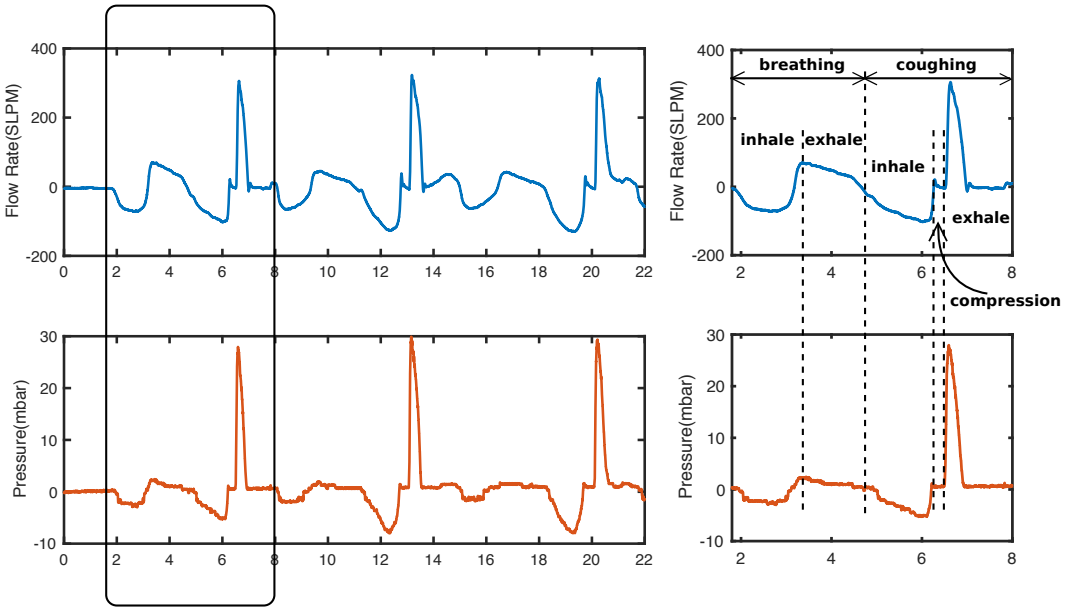

Figure 3.2: Flow rate and respiratory mouth pressure during three consecutive coughs by participants with a single cough profile enlarged on the right.

3.2 Design of CoughAid

Increased coughing efficiency is indicated by either an increased glottis pressure or an increased Peak Cough Flow rate (PCF), which can be achieved by increasing the expiratory muscle strength or by increasing the pressure resistance of the vocal folds. In this study we focus primarily on the function of the vocal folds and hence expiratory pressure (peak cough pressure) and peak cough flow rate were measured and analysed. CoughAid is designed to have the following characteristics: fast opening and closing, air tight closure, pressure feedback, expiratory flow feedback, pressure controlled opening, fail safe opening mechanism and patient override.

Figure 3.3 presents a photo of the CoughAid system design and Figure 3.4 shows an illustration of the connections of CoughAid . A disposable cardboard mouthpiece was used to connect to disposable anti-bacterial and anti-viral filter (BIOPAC, AFT4 VBMax, 35mm), which was then connected to a normally open solenoid valve (ASCO SCE210C35) via a respiratory tube (22cm diameter). For laryngectomy patient studies, a 3D printed stoma adaptor was used in place of the cardboard piece to ensure a air-tight connection around stoma. The solenoid valve was used to mimic the human glottis function during coughing; it controls the air flow by sealing and building up pressure in the respiratory tube. High speed photography analysis have shown the glottis opening time is around 25-30 ms [91]. The chosen valve could achieve a comparable fast opening time (15ms at fastest) and is also portable, low-cost and can maintain high pressure (9 bar), showing advantages over alternative valve types such as butterfly or ball valves, which are larger, slower or have lower maximum pressures. The valve automatically opens when MEP reaches a

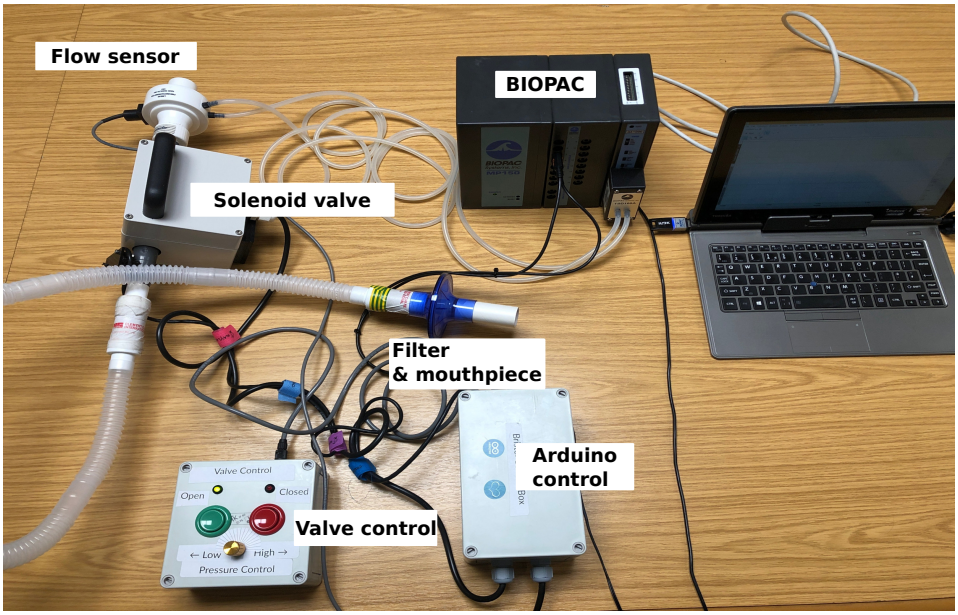

Figure 3.3: Photo of CoughAid.

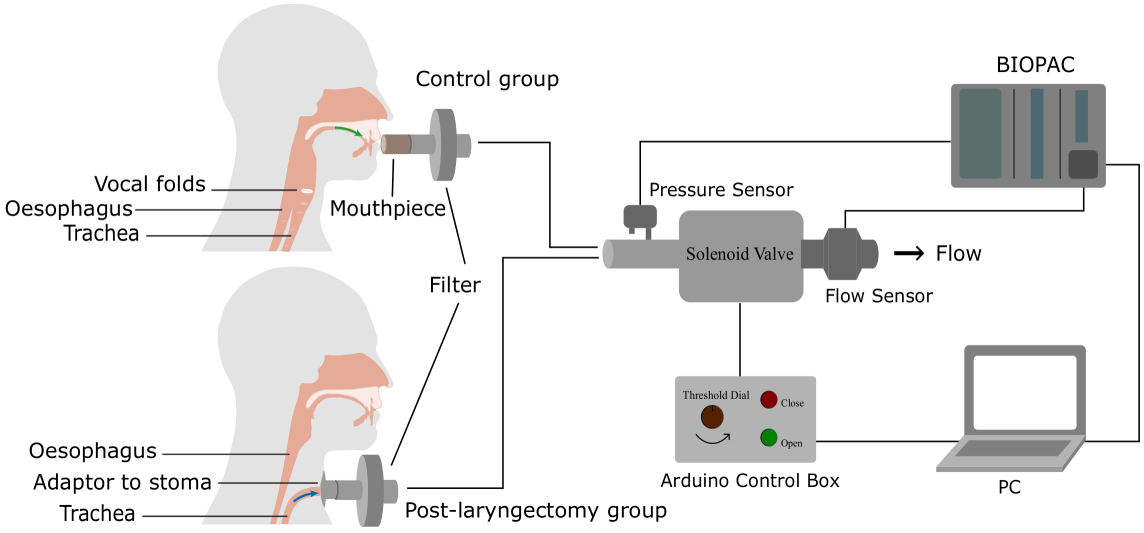

Figure 3.4: System design of CoughAid.

certain threshold (p_{th}), mimicking the way vocal folds open during a human cough. During the inhalation phase, the valve opens, allowing air to be inhaled by participants. In the compression phase, the valve is activated and closes, allowing pressure to build up. In the exhalation phase, the valve opens once more, allowing air to be rapidly expelled. The pressure is monitored in real time by a pressure sensor (Honeywell SSCSNBN015PDAA5) in the respiratory tube before the valve, thereby approximating glottis pressure. A Pneumotachometer (TSD160A) is attached to the expiratory flow end of the CoughAid to record cough flow rate using a BIOPAC MP150 data acquisition system.Using portable peak flow meters could increase the portability of CoughAid,

however studies have shown inconsistent flow results from various portable flow meters [92, 93]. Therefore a precision pheumotacheometer was chosen in this study because of its accuracy. All tubing is of standard size (22mm) used in clinical settings.

Since pressure thresholds can vary from person to person and as coughing conditions vary, a dial located on the control box allows participants to alter the pressure threshold p_{th} to a comfortable value. Manual override is available using two buttons on the control box (one for closing and one for opening the solenoid). Users can therefore open the valve at any time. The operation of the CoughAid is as follows: 1. The valve is open and the user inhales fully. 2. The valve is closed using the appropriate button, replicating the closing of the glottis in preparation for a cough. 3. The user increases pressure in their lungs against the closed valve, generating the pressure needed for the cough. 4. When the pressure measured in the respiratory tube reaches p_{th} the valve opens, rapidly releasing the pressurised air in the lungs and initiating an artificial cough.

3.2.1 Ethical Approvals

Ethical approval was obtained for this study from the University of Bristol Engineering Faculty Research Ethics Committee (UOB ID84502), and the University College London Research Ethics Committee (ID: 5697/006). Approval from both institutes was required because tests were performed at both. Informed consent was sought from all participants before their involvement in the study following UoB and UCL guidance.

3.2.2 Subjects

33 control participants were recruited (24 male and 9 female: ages 24 to 48; median age 28). Inclusion criteria for control participants were: any person between the age of 18 to 64; who does not have any condition or disease affecting their voice; and does not have any neuromuscular disorder. 5 post-laryngectomy participants were recruited at University College London (4 male and 1 female; ages 53 to 79; median age 72).

A power calculation was carried out using the software package “G*Power 3.1.9.2” [94], and data from an n = 5 control and m = 5 post-laryngectomy participant pilot study was used. Two tailed Wilcoxon signed-rank tests assumed, alpha = 0.05, beta = 0.8. A minimum sample size of 28 control participants was calculated for the difference in medians between CoughAid and voluntary coughs. A minimum sample size of 4 post-laryngectomy participants was calculated for the difference in peak cough pressure medians between CoughAid and voluntary cough, and 69 post-laryngectomy participants was calculated for the difference in peak cough flow medians between CoughAid and voluntary cough. The limited availability of post-laryngectomy participants restricted this group to m = 5.

3.2.3 Experiments

Experiments were carried out with n = 33 control participants and a pilot study was carried out with m = 5 post-laryngectomy participants to test the effectiveness of CoughAid. Peak Cough Flow (PCF, L/min), Peak Cough Pressure (PCP, cmH_2O) and expiratory acceleration (L/s^2) were measured during voluntary cough and CoughAid assisted cough. Results were compared between the control and the post-laryngectomy group.

In both voluntary and CoughAid cough tests, the control group was provided with a mouthpiece whereas the post-laryngectomy group was provided with a 3D printed adapter which ensured a good seal around the stoma. Mouthpiece was chosen over facemask because it gives higher peak flow rate [95]. Both groups were asked to breath in and out naturally through the mouthpiece/adapter several times to relax and to familiarise themselves with the device.

Participants were first asked to cough voluntarily with the valve kept open, giving a baseline for a peak voluntary cough. They were then asked to emulate a cough using CoughAid by performing a peak expiration manoeuvre. In both tests participants were asked to cough five consecutive times into the device. In tests using CoughAid, the cough pressure threshold was set by each participant to a level that they found comfortable.

In voluntary cough tests, the participant was instructed to cough as forcefully as they could (patient group users exhaled as forcefully as possible if unable to cough). In CoughAid cough tests, the pressure threshold (p_{th}) was fine-tuned by each participant using the dial. Detailed instructions were given and participants were given time to adjust the dial and attempt coughs at different pressure thresholds until they found a pressure threshold for which they could cough comfortably. For the control group, three different threshold settings were tested to ascertain its effect on cough effectiveness. Participants were asked to tune the threshold to mimic the situation of a “strong cough”, that is, to cough using maximum effort. Then the threshold was lowered a medium level, to mimic the condition of a moderate cough. The threshold was then lowered further to a point where participants felt it easy to cough, analogous to an instance of “throat clearing”. In the patient group, only one threshold setting was tested for safety reasons, when it felt most comfortable and natural to cough through the device.

3.2.4 Statistical analysis

All results are presented as mean ± standard deviation or median ± interquartile range where appropriate. Paired t-tests were used to determine differences in mean response to voluntary and CoughAid cough within the control group. Alpha cutoff was set to 0.05. Wilcoxon signed-rank tests were used to determine differences in mean response to voluntary and CoughAid cough within the post-laryngectomy group.

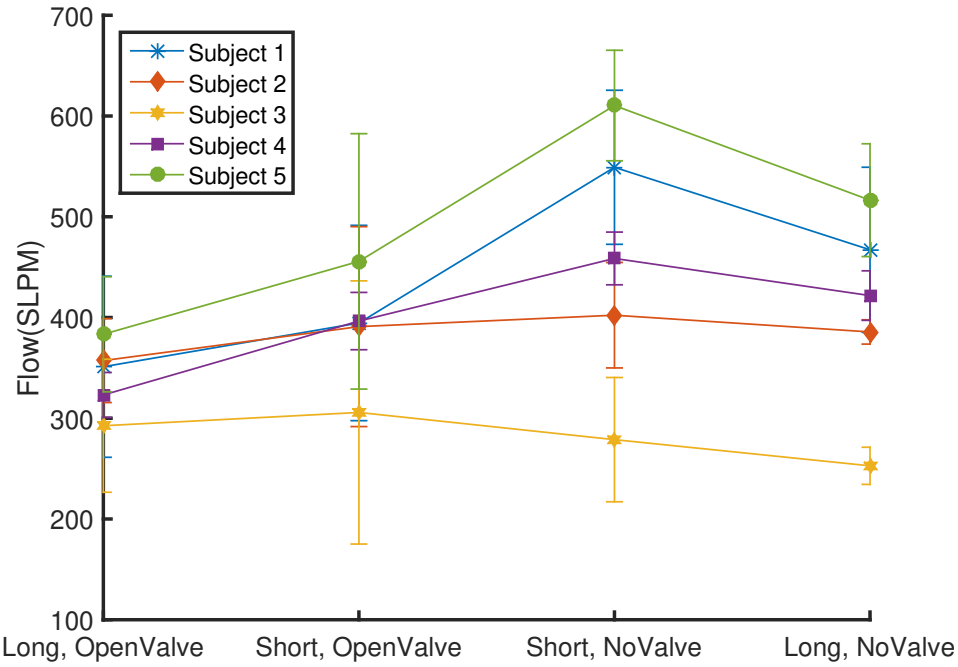

Figure 3.5: Peak flow rate with varied tube lengths and with/without valve.

3.3 Results

A pilot experiment was carried out with n = 5 control participants to investigate the effect of the valve and the tube length on air flow and recorded pressure. Two respiratory tube lengths, 17cm and 102cm, were tested and readings were taken with and without the presence of solenoid valve. Before the beginning of each test, subjects were asked to sit down and relax for a few minutes to avoid artefacts in the measurements due to any preceding aerobic activities. All subjects were instructed to inhale and then cough as hard as they could into the mouthpiece while standing. They were coached to pinch lips around the mouthpiece to prevent air leak during manoeuvres. Tests are carried out as follows: Test 1: Coughing through long tube, with opened valve. Test 2: Coughing through short tube, with opened valve.Test 3: Coughing through short tube, without valve in system. Test 4: Coughing through long tube, without valve in system.The effects of tubing length and the presence of valve on peak cough flow is presented in Figure 3.5. It can be seen that in most cases, flow is highest for test 3 (short tube and no valve in the system). However 102cm tubing is chosen for easy handling in CoughAid experiments.

Figure 3.6 and Figure 3.7 show a sample coughing profile of one participant from the control group and one from the post-laryngectomy group. It can be seen from the graphs that when comparing voluntary and CoughAid coughs, CoughAid generates a higher peak flow rate and a higher peak cough pressure, and takes a longer time to return to baseline. It is to be noted that the peak cough pressure measured in voluntary coughs is equivalent to MEP, while that recorded in CoughAid coughs is equivalent to glottal pressure. Cough acceleration, also known as volume

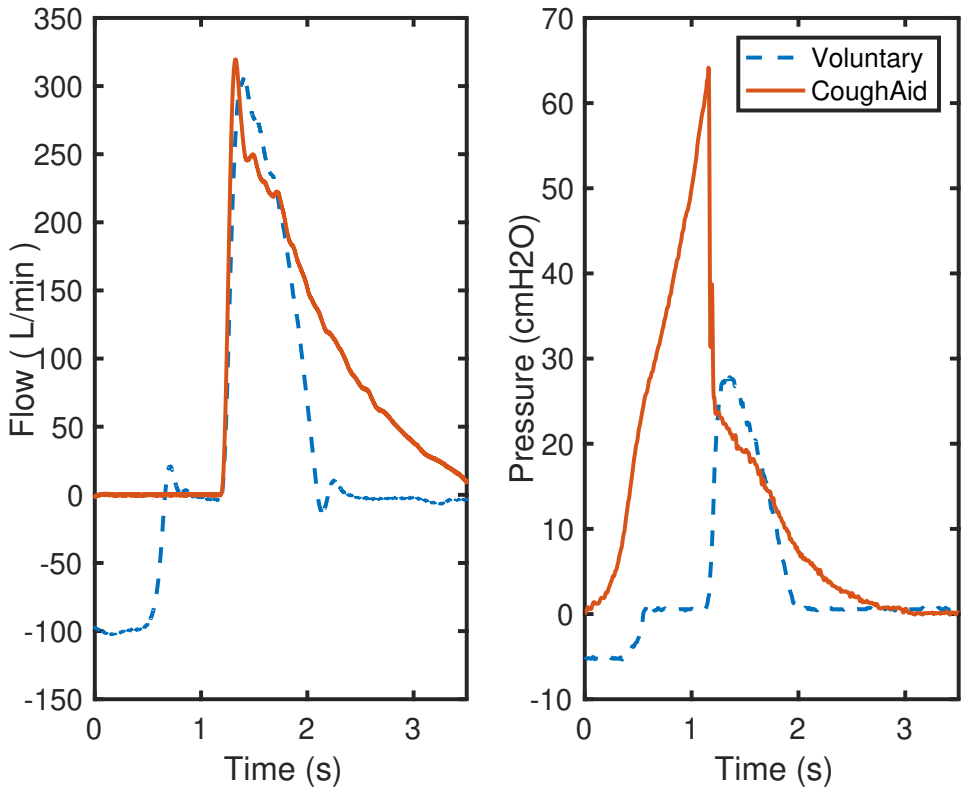

Figure 3.6: Example cough flow and pressure profiles from control group during voluntary and CoughAid assisted cough.

	Peak Cough Flow (L/min)	Peak Cough Pressure (cmH_2O)	Acceleration (L/s^2)
Voluntary Cough	236.8 ± 69.5	19.8 ± 4.0	45.3 ± 13.5
Low p_{th} CoughAid	279.3 ± 67.1	58.8 ± 18.2	74.2 ± 14.1
Medium p_{th} CoughAid	290.6 ± 74.3	69.1± 22.1	78.5 ± 14.5
High p_{th} CoughAid	329.1 ± 82.9	94.4± 32.7	91.0 ± 19.0

Table 3.1: Summary of coughing characteristics in control group, expressed as mean ± one standard deviation.

acceleration, calculated as the ratio of cough peak flow to the time to peak, represented as the gradient rise to peak cough flow [96, 97], was also higher in CoughAid coughs.

In CoughAid experiments, only pressure and flow rate data were collected using the BIOPAC system, pressure threshold was back-calculated from pressure and flow rate profiles based on the fact that the valve will only open when the pressure threshold is reached. It is assumed that the threshold pressure is reached when exhalation begins. To take into account delays in system processing and valve opening, a constant 80ms delay was assumed between reaching p_{th} and the CoughAid actuating.

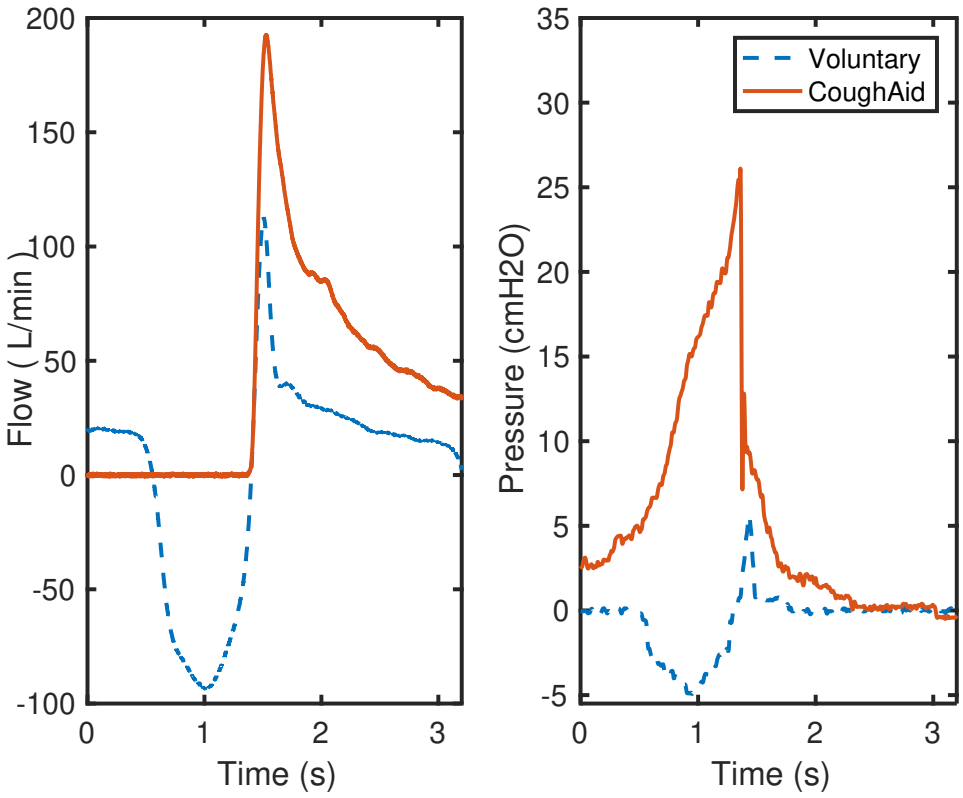

Figure 3.7: Example cough flow and pressure profiles from post-laryngectomy group during voluntary and CoughAid assisted cough.

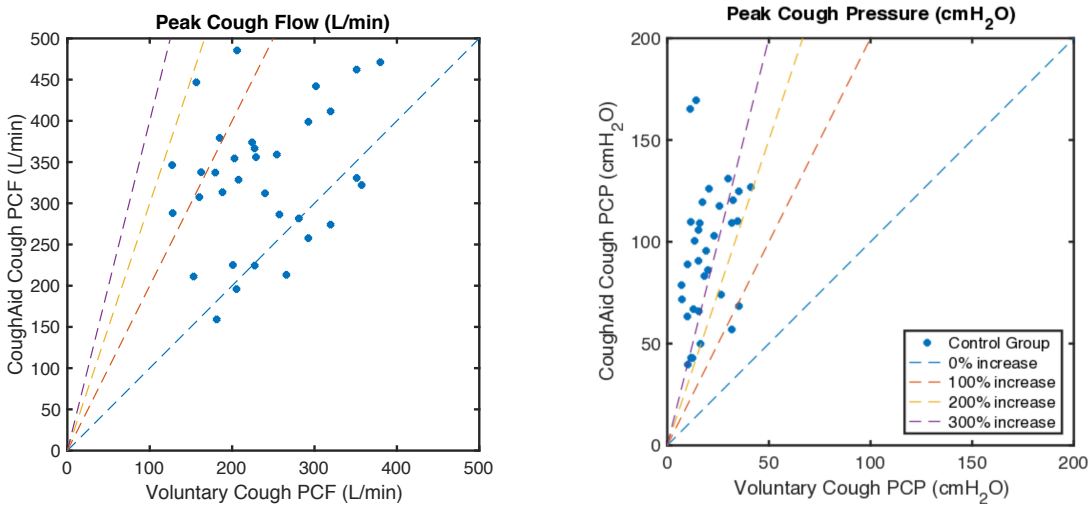

Figure 3.8: Mean peak cough flow (PCF) and peak cough pressure (PCP) with and without CoughAid for all control participants. Lines showing percentage increase of CoughAid with respect to voluntary are shown for reference.

Table 3.1 summarises the mean PCF, PCP and cough acceleration in all control group tests. Compared with voluntary coughs, all CoughAid tests generate higher mean PCF, PCP and

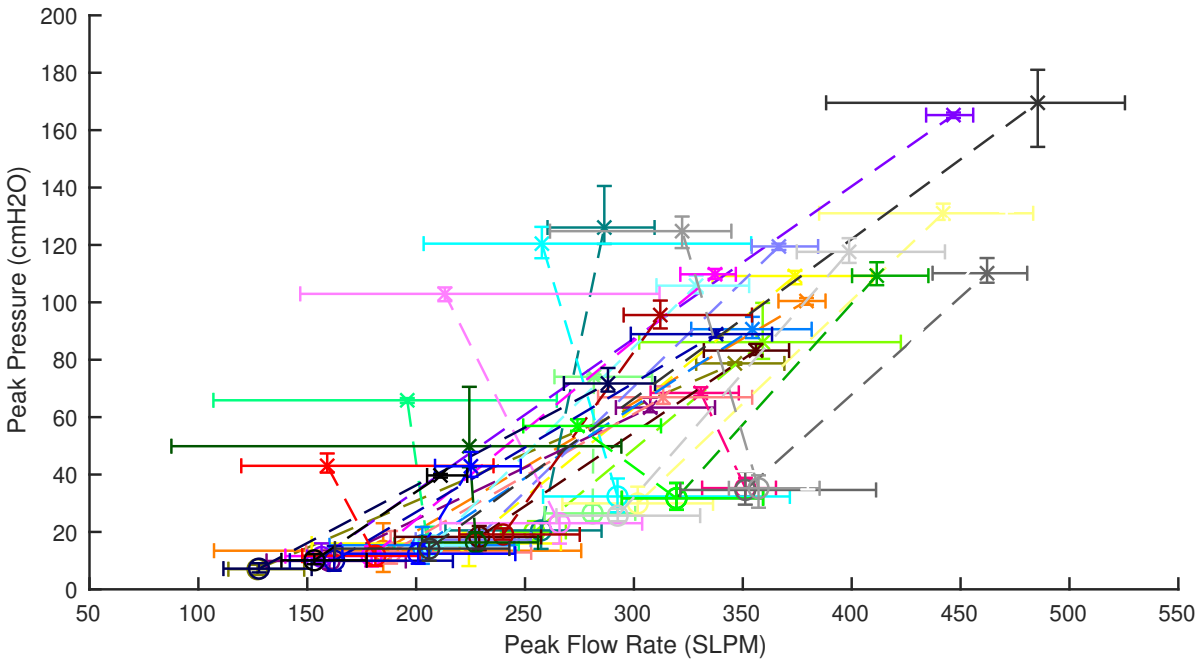

Figure 3.9: Scatter plot of coughing characteristics in control group with each participants marked in different colours. ◯ representing mean voluntary cough; × representing mean CoughAid cough at high pressure threshold; horizontal lines showing error bar of peak cough flow; vertical lines showing error bar of peak cough pressure; dotted lines show the change in mean value before and after using the CoughAid.

acceleration. Within the CoughAid tests, the mean values of all parameters were seen to increase with pressure threshold.

Figure 3.8 shows how mean PCF and mean PCP change with and without using CoughAid in control group, with illustrative lines marking 0, 100, 200 and 300% increase of CoughAid with respect to voluntary cough. Figure 3.9 shows coughing characteristics in control group. Error bar was plotted for each participant with dotted lines marking the mean values with and without using CoughAid. Figure shows a gradient increase in most cases.

It can be seen that PCP was greater during CoughAid cough (94.4±32.7 cmH_2O) than during voluntary cough (19.8±4.0 cmH_2O) (paired t-test, t(64)=12.6, p<0.0001). PCF increased during CoughAid cough (329.1±82.9 L/min) compared with during voluntary cough (236.8±69.5 L/min) (paired t-test, t(64) = 4.9, p < 0.0001). Comparison between mean PCP and PCF with and without using CoughAid show that PCF increase can be found in 25/33 participants while PCP has increased significantly (p < 0.0001) in all participants. Peak cough flow differences before and during using CoughAid are further shown in Figure 3.12. Cough acceleration is also evaluated since it is one indicator on an effective cough. It has also increased significantly (t(64) = 4.39, p<0.01) using CoughAid, as shown in Table 3.1.

Table 3.2 tabulates the mean PCP and PCF value in post-laryngectomy participants with and

	Peak Cough Flow (L/min)	Peak Cough Pressure (cmH_2O)	Acceleration (L/s^2)
Voluntary Cough	182.3 ± 86.9	11.9 ± 6.5	36.4 ± 14.6
CoughAid	226.5 ± 141.4	46.2 ± 29.3	115.9 ± 165.9

Table 3.2: Coughing characteristics in post-laryngectomy group.

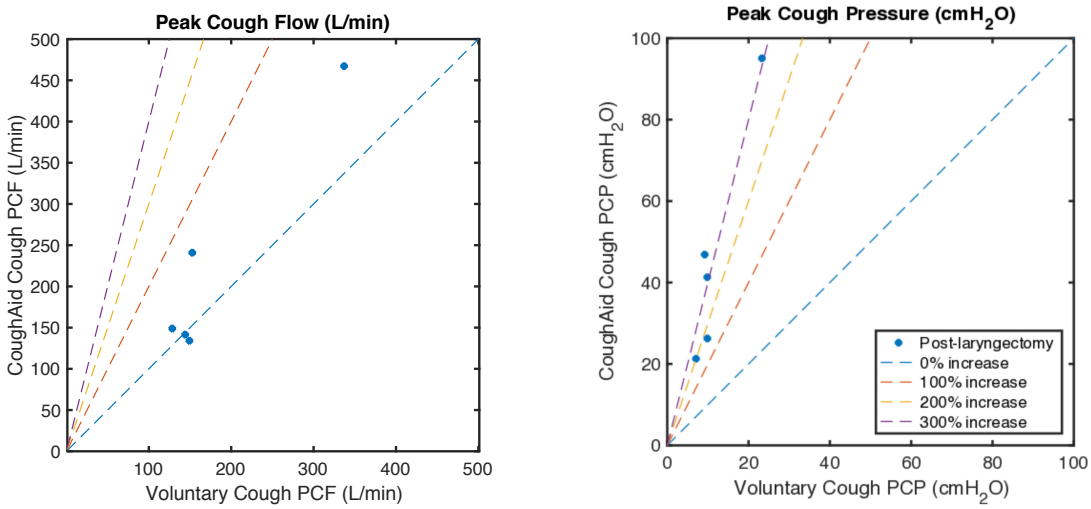

Figure 3.10: Mean peak cough flow (PCF) and peak cough pressure (PCP) with and without CoughAid for all post-laryngectomy participants.

without CoughAid. Figure 3.10 shows how PCF and PCP change with and without CoughAid in the post-laryngectomy group, with illustrative lines marking 0, 100, 200, 300% increase of CoughAid with respect to voluntary cough. In these CoughAid tests, only one comfortable pressure threshold was set and tested for each post-laryngectomy participant. Figure 3.11 shows coughing characteristics in post-laryngectomy group. Error ellipse was plotted for each participant with solid lines marking the mean values with and without using CoughAid. It shows significant gradient increases in two cases. A Wilcoxon rank sum test shows a significant increase in pressure ($p = 0.0159$) with and without using CoughAid whereas peak flow ($p = 1$) does not show notable differences among the cohort. Results show an improvement in flow rate in 3/5 post-laryngectomy participants as can be seen more clearly from the ordered data in Figure 3.12.

When comparing data from post-laryngectomy group to control group, using the CoughAid, post-laryngectomy coughs also reached similar peak cough flow to the control group's natural cough (Wilcoxon rank sum test, $Z = -0.9933$, $p = 0.32$), and achieved higher peak cough pressure (Wilcoxon rank sum test, $Z = 2.6775$, $p = 0.0074$).

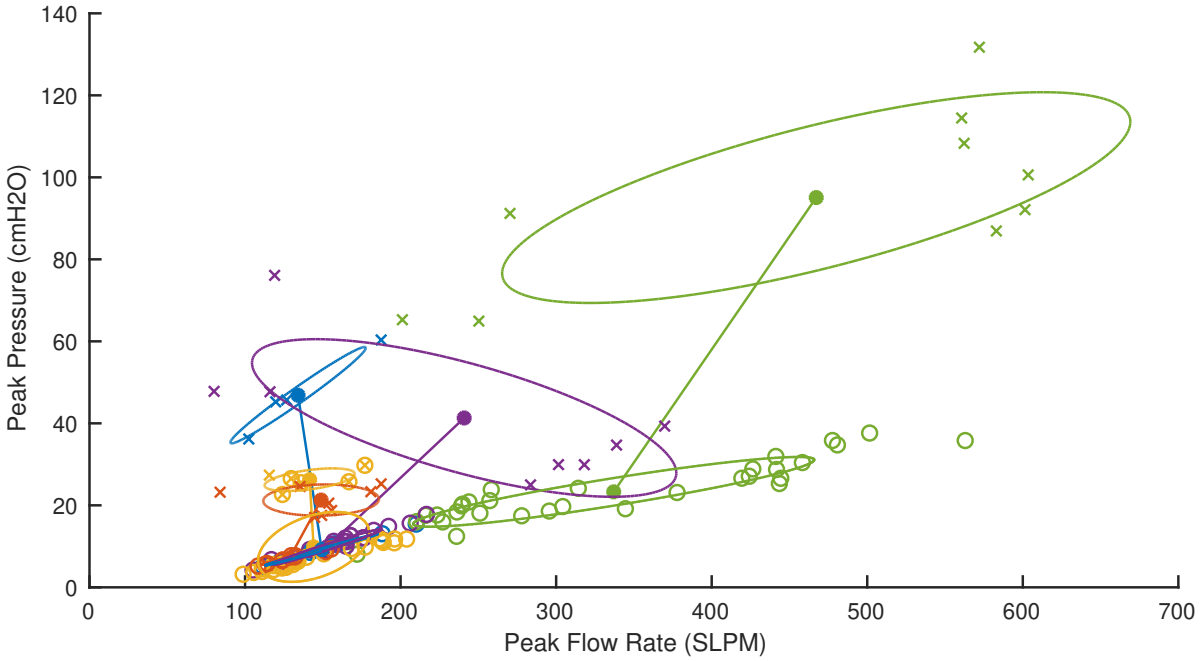

Figure 3.11: Scatter plot of coughing characteristics in post-laryngectomy group with confidence ellipse, with each participant marked in different colours. ◯ representing voluntary cough; × representing CoughAid cough; ⋆ representing the centroids of cough data; error ellipses showing variance of data at 95% confidence level; lines show the change in mean value before and after using the CoughAid.

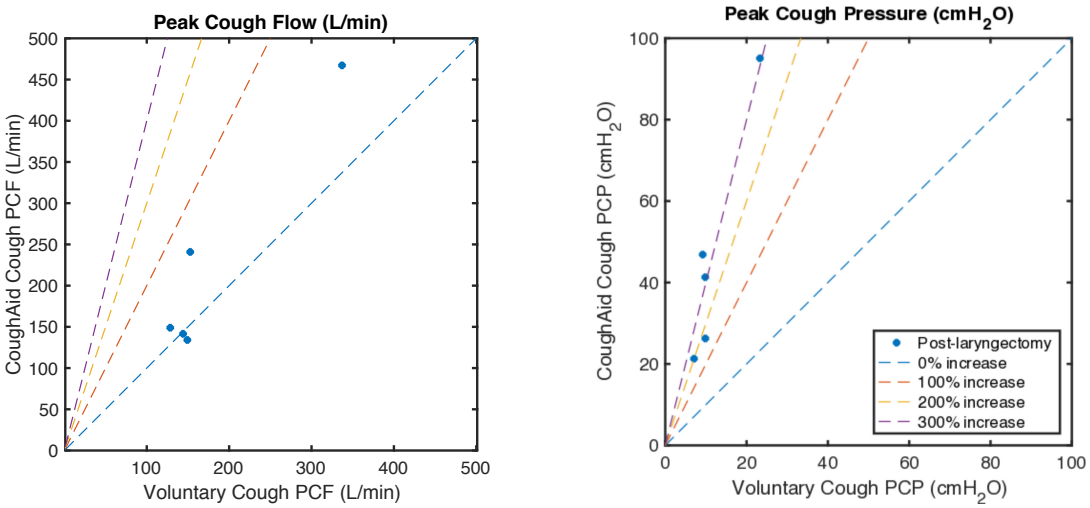

Figure 3.12: Difference in mean Peak Cough Flow in control group (Left) and post-laryngectomy group (Right), after using CoughAid. Subjects ordered in ascending peak flow rate.

3.4 Discussion

In this study all cough data was analysed and there was no subjective data selection post experiments. The data collected therefore shows the natural dynamics of a series of voluntary and CoughAid coughs. We found that the CoughAid coughing assist device improved peak cough pressure and peak cough flow rate. The average percentage increase in peak flow rate was observed at 49% (paired t-test, $t(64)=4.9$, $p<0.0001$) in the control group and 20% (Wilcoxon rank sum test, $p = 1$) in the post-laryngectomy group, while the average percentage increase in peak cough pressure was observed at 467% (paired t-test, $t(64)=12.6$, $p<0.0001$) in control group and 281% (Wilcoxon rank sum test, $p = 0.0159$) in the post-laryngectomy group. Note that the pressure sensor is located before the valve but after all tubing in the system. Measured pressure is therefore equivalent to expiratory pressure at the mouth in voluntary coughs and gastric pressure in CoughAid coughs. An effective cough can be dependent on several factors, including expiratory airflow rate, gas-mucus interactions, mucus properties, the inhalation volume and expiratory muscle strengths [98, 73]. Studies show that inhaling high volumes, combined with glottis closure prior to the expiration phase, could enable respiratory muscles to generate high intrathoratic pressures. This pressure acts as a high driving force for the airflow during cough and hence contributes to high peak flow rate [98]. In the absence of the larynx (eg: laryngectomy, tracheotomy), coughing can still be generated with low airfow by performing a huffing manoeuvre (a forced expiration against open glottis), although the cough is less effective [99, 86, 73]. Maximum expiratory pressure is a commonly used parameter to assess the strength of respiratory muscles [76, 77], and has been shown to positively correlate with improved cough capacity [100, 101, 102].

In voluntary experiments, the peak cough pressure and flow from both control and post-laryngectomy groups are lower than average published values in healthy adults [77, 86]. This is attributed to the tubing in the system as well as the presence of the solenoid valve slightly restricting air flow. The 102cm respiratory tube represents a total dead volume in the CoughAid of approximately 0.39 litres, which is approximately 6.5 % of an average male's lung capacity and 9.3 % of an average female's lung capacity [103]. Other possible causes could be leakage around mouthpieces during coughing experiments or participnats coughing while not fully prepared. Additionally, while undertaking the experiments, participants were asked to cough 5 times consecutively into the tube. This could result in a decrease in peak cough flow rate and pressure due to tiredness.

The control and post-laryngectomy groups had different age profiles, and age related factors were not taken into account when analysing the results. According to Cardoso et al [104], as age increases, peak cough flow decreases. However, the post-laryngectomy group (median age 72) had comparable PCP values to the control group (median age 28). This may be due to the post-laryngectomy group having stronger diaphram muscles than non-laryngecotomies of the same age group because they may use a technique called diaphragmatic breathing (also called

abdominal breathing) to help breathing and coughing after laryngectomy [105].

In this study, pressure thresholds were set by each post-laryngectomy participant and were subjective and limited to voluntary cough manoeuvres. An alternative way of controlling the opening of the valve is to assess the activity of expiratory and accessory muscles through real-time EMG monitoring. Research has shown ways to characterise the difference between voluntary and reflex coughs using EMG signals [106]. The integration of an EMG signal into the valve control would expand the capability of the CoughAid to wider coughing scenarios. Replacing the solenoid valve with a valve with lower restriction could potentially increase cough effectiveness due to the reduced pressure drop across the valve [80]. Further investigation will also be carried out to quantify the relationship between peak cough pressure, threshold pressure, cough acceleration and peak flow rate produced by the CoughAid.

Results from this study show that CoughAid is a promising approach to increasing cough efficiency. It shows a comparable PCF increase to using MI-E and MI-E + MAC methods, although less effective than using IPPB + MAC in neuromuscular patients [107, 83]. CoughAid could be integrated in a patient's everyday life easily as it can be light weight, easy to use and each component is separable for handling and cleaning. Scaling CoughAid down to the size of a peak flow meter (approximately 22cm long and 6cm wide) could effectively aid larygecotomy patients to cough when needed and the ultimate goal is to integrate CoughAid into a comfortable, wearable device.

3.5 Conclusion

This chapter presents an approach to assist post-laryngectomy patients cough more effectively. The rationale is that increasing the coughing pressure and flow rate would increase coughing effectiveness. This is usually achieved by increasing the strength of respiratory muscles. In this study, we explored an alternative, where an increase in the strength of an artificial glottis closure influences coughing pressure and peak air flow. To achieve this we designed and built the CoughAid, which mimics the function of the glottis. We then tested and compared the peak cough flow and peak cough pressure in control and post-laryngectomy groups through a series of respiratory experiments. Results show a significant increase ($t(64) = 4.9$, $p < 0.0001$) in peak cough flow rate and peak cough pressure ($t(64) = 12.6$, $p < 0.0001$) among 33 control participants using CoughAid. A pilot study with a smaller cohort of laryngectomy patients shows improvement in peak cough pressure ($p = 0.0159$) using CoughAid. Preliminary results also show that post-laryngectomy coughs achieved similar peak cough flow ($Z = -0.9933$, $p = 0.32$) to the control group's natural cough. Coughing capabilities could be improved through using CoughAid. This work paves the way for new treatments for cough insufficiency in respiratory disease sufferers and may additionally have potential for the rehabilitation of coughing following respiratory conditions such as COVID19.

Further investigations will be carried out to analyse different pressure threshold settings in order to quantify the relationship between glottal strength and cough characteristics.

CHAPTER 4

RESPIRATORY SIMULATOR

Section 4.3 of this chapter is based on the work presented in the paper:

[37] M. E. Giannaccini, K. Yue, J. Graveston, M. Birchall, A. Conn, and J. Rossiter, "Respiratory simulator for robotic respiratory tract treatments," in *2017 IEEE International Conference on Robotics and Biomimetics (ROBIO)*, pp. 2314–2319, IEEE, 2017

The author contributions to the work presented in section 1.4 are as follows. K.Y. conducted experiments with human participants, developed the control programme for simulated coughing, collected data and performed analysis on results. M.E.G. designed and manufactured the mechanical trachea and glottis in the respiratory simulator. J.G. and M.B. provided clinical insights. A.C. and J.R. supervised the project.

Main contributions

- Design and manufacturing of a respiratory simulator.
- Developed a control system to simulate breathing and coughing profile that matches the characteristics from human participants.

4.1 Introduction

In the previous chapter, we investigated a potential solution to improve cough efficiency through a detailed patient and volunteer study, leading to the development of the CoughAid device. CoughAid can effectively increase peak cough pressure and peak cough flow. In this chapter

we further investigate respiratory airflow characteristics by building a computer-controlled respiratory test rig that can simulate respiratory functions. The simulator uses the same solenoid valve as CoughAid to mimic glottal function. This chapter describes the development of a computer controlled respiratory simulator to simulate breathing and coughing. Two versions of the simulator, Respiratory Simulator 1.0 and Respiratory Simulator 2.0, were designed and built. Respiratory Simulator 1.0 was used to conduct preliminary tests, the results of which then led to the design of the more advanced Respiratory Simulator 2.0. In this chapter we present the full design and experimental results of Respiratory Simulator 2.0, with preliminary test results from Respiratory Simulator 1.0 listed in Appendix A.

4.2 Background

This section introduces the physiological background on the human respiratory system and the development of computational and mechanical models of the respiratory system.

4.2.1 Physiology of the human respiration system

In humans, a typical respiratory system is the respiratory tract, as shown in Figure 4.1. The respiratory tract is divided into two parts: the upper respiratory tract (nasal cavity, pharynx and larynx), and the lower respiratory tract (trachea, bronchi and lungs). Together it provides vital functions such as breathing, sound production, olfactory assistance and protecting the airway from dust and microbes entering the body through mucus production and coughing.

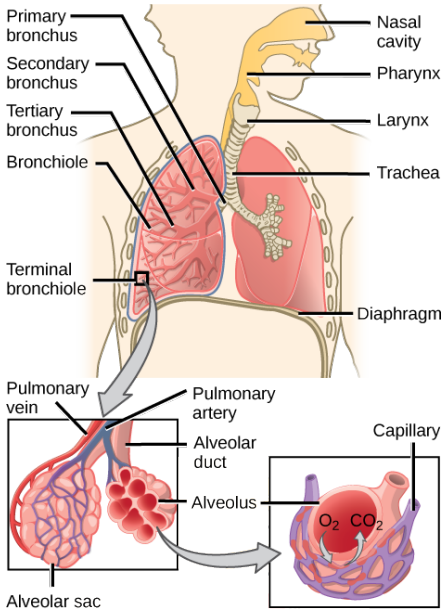

Figure 4.1: Anterior view of the respiratory system. Figure reproduced from [16].

Volume	men (L)	women (L)
Inspiratory reserve volume(IRV)	3.1	1.9
Tidal volume(TV)	0.5	0.5
Expiratory reserve volume(ERV)	1.2	0.7
Residual volume(RV)	1.2	1.1

Table 4.1: Average lung volumes in adults [1]

During breathing, air enters from the nasal cavity where a layer of nasal mucosa acts as filter to prevent pollutants from entering the respiratory tract [108]. Air then flows through the pharynx and larynx and moves into the trachea, which then branches into the left and right bronchi and the lungs. Each of the bronchi subdivides at successive intervals, forming a branching structure known as the respiratory tree or tracheobronchial tree. At its smallest scale, tiny bronchioles connect with the alveoli that provide the essential functions of gas exchange.

There are approximately 300 million alveoli, 14 million alveoli ducts and 280 billion capillary segments in a pair of human lungs [109]. Studies have been carried out to understand the morphometric characterisation of the lung by investigating micro-anatomy using a method called stereology. The goal is to define the architecture of airways and blood vessels in the lung, to estimate alveolar surface area and volume to understand pulmonary diffusing capacity and to understand lung pathology through cell biology [110].

The lungs, which are protected by the rib cage and the diaphragm, are located in the thoracic cavity. During inhalation, the diaphragm contracts, thereby engaging intercostal muscles, and the rib cage is pulled upwards and outwards resulting in an increased in chest cavity volume. During exhalation, the diaphragm and muscle relaxes, and air flows out of the lung [111].

The average total lung capacity (TLC) is 6L for men and 4.2L for women [103], and can vary with height, weight and living area. Inspiratory reserve volume (IRV), tidal volume (TV), expiratory reserve volume (ERV) and residual volume (RV) are some critical characteristic values that can be directly measured by spirometer in a pulmonary function test, to distinguish between restrictive and obstructive pulmonary diseases. Typical values are presented in Table 4.1. The average breathing rate is 30-60 breaths for newborns and decreases to 12-20 breaths for adults, as detailed in Table 4.2.

4.2.2 Modelling human respiratory system

Robotic healthcare is a growing and multi-faceted field where robots help perform surgery, remotely provide care to patients, aid in supplying various physical therapies and further medical research. Robotic simulators of human physiology provide a powerful platform to advance the development of novel treatments, prostheses and therapies.

Average resting respiratory rates (L/min)	
birth to 6 weeks:	30 - 40
6 months:	25 - 40
3 years:	20 - 30
6 years:	18 - 25
10 years:	17 - 23
Adults:	12 - 18
Elderly $\geqslant$ 65 years old:	12 - 28
Elderly $\geqslant$ 80 years old:	10 - 30

Table 4.2: Average resting respiratory rates in different age groups [2] [3] [4] [5]

In past decades, different approaches have been made to model the respiratory system. In 1945, Gray developed the first mathematical model describing the chemical control of ventilation. In 1954, Grodins et al. presented the first dynamic analysis of the system with CO_2 inhalation as a single input force [112]. The model was then refined and extended using computational modelling to include lung-blood-tissue gas transport and exchange, chemical transport and acid-base buffering, concentration equilibria, blood flow behavior and a control equation defining the carotid chemo-receptors for dependence ventilation [113]. Physiological aspects of the system such as Hering-Breuer reflex, the varying lung volume and dead volume was then brought into the well-developed chemical control models [114]. Mathematical models were also used to simulate different lung pathologies [115].

Despite models that focused on simulating chemical changes, computational fluid dynamics (CFD) modelling has also been widely used to simulate the air flow pattern through the respiratory system. Examples include the simulation of flow in the upper airway tract where pressure and velocity distributions were considered [116]; to analyse the deposition patterns of inhaled aerosols under multiple physiologic, geometric, and particle characteristics conditions [117, 118, 119] as well as with different breathing patterns [120]. More recent studies have also taken into account the complexity of the multiscale geometry of the broncho-pulmonary tree with the aid of CT and MRI scan to generate more accurate 3D CFD simulation [121], and to assist operations such as Video-assisted thoracoscopic surgery [122].

Mechanical respiratory simulators have also been developed and used in clinician education, guiding therapies, evaluating new devices and techniques, validating numerical models, aerosol inhalation studies and to improve our understanding of the internal respiratory system [123, 124, 125]. They simulate some physiological characteristic of the pulmonary system and can be used to simulate certain pathological conditions [126].

In past decades, mechanical simulators focused on the mechanical ventilation system where dynamic characteristics such as lung pressures and air flow dynamics were the primary focus

of simulation. Some have piston-driven bellows or air sacs to provide varied volume for ventilation [127, 128, 129, 130], and others use a fixed volume but utilise cranial pressure for the simulation of active breathing [131]. Anatomical features , such as latex expandable chambers to mimic the lungs or porcine lungs as human analogues, have also been added to the system to improve the simulated breathing pattern [132]. Some representative examples of different types of respiratory simulators as well as some commercialised lung simulators are listed in Table 4.3.

More robust and accurate simulators are still needed in research and as can be seen from Table 4.3, there are still gaps in the capability of current systems that need to be further investigated. For instance, most respiratory simulators simulate healthy and pathological breathing patterns and are used to study neonatal applications, aerosol dispersion or diseases related to lungs, but very few investigate active coughing simulation. Also, despite advances in mechanical lungs, few mechanical simulators have included the upper airway structures (trachea, bronchi,vocal folds, nasal cavity) in designs, although numerical and computational studies have shown those structures can affect airway dynamics [133, 134, 135]. In this work we present a new physical simulator that includes the mechanical trachea and bronchi structure, which aims to replicate the breathing and coughing characteristics of healthy humans, providing a first-stage evaluative tool for the development of robotic healthcare solutions for cough-related respiratory conditions, and to generate a platform for implantable assistive medical devices in the future.

4.3 Respiratory Simulator 2.0

The computer-controlled respiratory simulator 2.0 was designed to replicate as closely as possible the dimensions, shape and function of the human respiratory system in the hardware design. It was an improved version of the Respiratory Simulator 1.0, of which some preliminary characteristic test results are listed in Appendix I. The primary goal is to simulate the human breathing and coughing profile, and therefore micro-anatomy was not taken into account in the design process.

4.3.1 System Design

Respiratory simulator 2.0 was designed to approximate a 1:1 replica of the human respiratory system. Approximations were made to simplify the physical design of the structure. All components of the simulator are rigid, contrary to the nature of the human respiratory system, which is prevalently composed of soft and compliant structures.

Product	**Lung Simulator**	**Upper-airway simulator**	**Design feature**	**Main function**
i-Lung [132]	Yes	No	primed porcine lung	breathing simulation
DML phantom [130]	Yes	No	Lucite cylinder and latex balloon	simulate and reproduce 3D nonisotropic lung deformations
Mechanical lung [128]	Yes	No	computer-controlled, piston driven	modele static and dynamic compliance of the respiratory system and nonlinear flow-resistance properties.
Bellows-less Lung [131]	Yes	No	fixed-volume pressure controller	breathing simulation
XPulm [125]	Yes	No	latex bags, primed porcine lungs combined with mathematical model	Realistic breathing pattern simulation
Cough Simulator [136]	No	Yes	pressurized gas tank, nebulizer, ejector and solenoid valve	study transmission of disease by human coughing
ASL 5000 [137]	Yes	No	Product by INGMAR medical	Adult/Neonatal breathing simulating
Training & Test Lung [138]	Yes	No	Product by Michigan Instruments	Simulating symmetrical or asymmetrical lung disease
ACCU LUNG [139]	Yes	No	Product by FLUKE biomedial	For evaluating ventilator performance

Table 4.3: Representative examples of respiratory simulators.

Technical specification		**Respiration capabilities**	
Total volume	6L	Vital capacity	0 - 6 L
Actuator force	0 - 80 N	Max. flow rate	112 L/min
Actuator speed	0 - 280 mm/s	Rate at 4.8L VC	23 breaths/min
Accuracy	45 μm		

Table 4.4: Technical specification and respiration capabilities of the rig

	men (mm)	**womem (mm)**
Left bronchus length	47.8	43.5
Right bronchus length	15.3	13.2
Left bronchus diameter	12.9	10.1
Right bronchus diameter	15.2	12.5

Table 4.5: Length and diameter of the semi-bronchi[6].

As illustrated in Figure 4.2, Simulator 2.0 comprises five components: actuation system, lungs, bronchi, trachea and glottis. It has a 450mm computer-controlled Zaber linear actuator (X-LSQ450B-E01) to model the movement of diaphragm, two 3L pneumatic syringes (KoKo KRS007) configured in parallel to give 6L total lung capacity, exceeding the average vital capacity of both men (4.6L) and women (3.1L). The Zaber linear slide has a maximum speed of 280mm/s and is able to hold 75N, which is more than sufficient to simulate breath. In this configuration the actuator and syringes can generate flows up to 112L/min, providing the full range of human-like respiratory flow rates.

Table A.1 summarises the technical specification and the respiration capabilities of the respiration test rig.

As mentioned in the previous section, the bronchi is a complicated branching structure that goes deep into the lungs, therefore to simply we only included the main bronchi in this design.

Two flange connectors were used to secure the the syringes to the PLA 3D printed channels that imitate the bronchi. The diameter of the channels were gradually reduced to the physiological dimension of 12.7mm and converged into one channel with a 70 degrees angle between the two channels, according to the average anatomically-correct value in anatomical studies of the angle of tracheal bifurcation, which is approximately 70 degrees [140]. This semi-bronchi component was 29mm long, taking the average value from Table 4.5.

A further flange connector was used to connect the semi-bronchi component to a 19mm internal diameter, 108mm long acrylic tube which imitates the function of the trachea. The

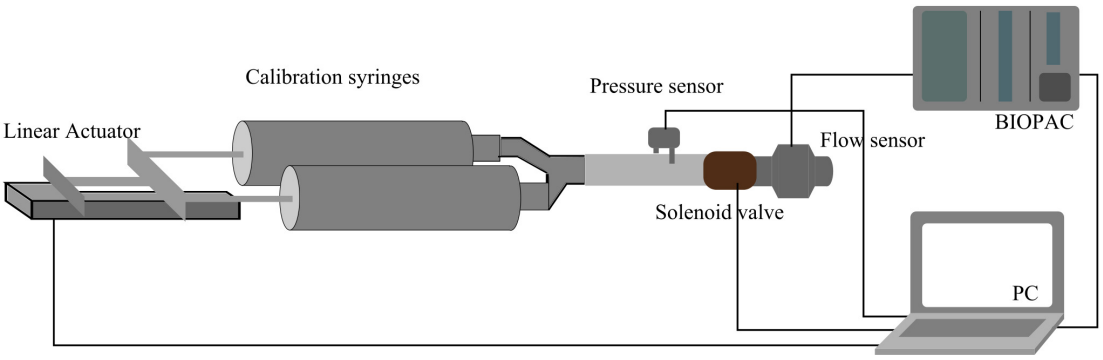

Figure 4.2: Respiratory Simulator 2.0

dimensions are chosen to be an average value within the range from literature [141, 142, 143, 144, 145]. The cross section of the human trachea varies, with sections showing elliptical, C-shaped, D-shaped, triangular and circular shapes [146]. It also have cartilage rings on its walls, which can affect the upper airflow and can be important factors in analysing air-borne diseases, inhaled pollutants and inhaled medications [135]. For this study the main focus is on simulating breathing and coughing, and therefore a rigid and smooth wall was used, and the circular shape was chosen because it was mostly readily fabricated.

A differential pressure sensor (SIP, NB 015PD TruStability, Honeywell) was inserted into a hole in the trachea. The same normally open, two port, solenoid valve (SCE210C35-24VCC, Asco) that was used in the previous chapter was used to imitate the opening and closing function of the glottis. A BioPac flow meter(TSD160A) was fixed to the exhaust side of the solenoid valve. The valve was powered through a relay which was controlled using a data acquisition device (DAQ, USB-6211, National Instruments), pressure data was collected utilising DAQ as well. The system was controlled via MATLAB2017®, which was also used for the data post-processing.

The working principle of the simulator is repeatable and robust: the computer-controlled actuated linear slide was used to replicate the movement of the human diaphragm and generated the force needed to drive the syringes. The air was then pushed through the semi-bronchi and semi-trachea components. In the case of breathing, the solenoid valve was kept open and the breathing flow rate was measured with the BioPac flow meter attached to the exhaust side of the valve. The simulation of a cough comprised of four stages: 1) the solenoid valve is closed, 2) the actuated linear guide compresses air in the system until 3) the pressure sensor registers a pressure above a fixed threshold; this triggers 4) the opening of the valve which causes the exhalation of the compressed air.

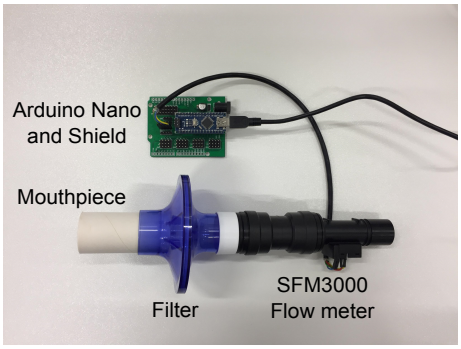

Figure 4.3: Devices used for experiments with participants. The filter was connected by an adaptor to the flow meter, which communicates with the Arduino micro-controller.

4.3.2 Experiment with healthy participants

Breathing and coughing experiments were carried out with 8 healthy participants within the age group of 25-40 years (ethics approval was granted from Faculty of Engineering Ethics committee, University of Bristol Ref:57763). All participants followed the same experimental procedures. The participants were asked to perform three tasks:

1. Normal Breathing (Duration: 30-60s) The subjects are asked to breath as naturally as they can.

2. Deep Breathing (Duration: 30-60s) The subjects are asked to take a series of deep breaths.

3. Coughing (Cough 3 times) The subjects are asked to take breath normally, then take a deep breath and then cough as forcefully as they can.

Before beginning each test, participants were asked to sit down and relax for a few minutes to avoid artefacts in the measurements due to any preceding aerobic activities.

A Sensirion SFM3000 flow meter was used to measure normal breathing and deep breathing and the BioPac Pneumotachometer (TSD 160A) was used to gather coughing data. A disposable anti-viral and anti-bacterial filter prevented contaminants from each participant from going into the flow meter (Figure 4.3). The data gathered with the Sensirion SFM3000 flow meter was collected utilising an Arduino Nano, while the Biopac system utilises its own data acquisition system MP150 and software.

4.3.3 Simulation methods

The tidal volume (TV) was utilised as a starting point in simulating the human breathing pattern. TV was calculated by identifying the flow rate data obtained in the experiments described in Section 4.3.2. Since the volume of the syringes was known, a simple proportion yielded the syringe

plunger travel needed to obtain the same volumetric flow as in the physiological experiment. Flow rates and acceleration were identified utilising an iterative process.

Experiments aimed at reproducing coughing were conducted by specifying the travel distance, velocity and acceleration for the linear guide, which pushed the syringes forward and increased the internal system pressure. Once a certain pressure threshold was reached, the solenoid valve was opened, thus releasing the pressurised air and generating an artificial cough.

In order to reproduce a coughing event, the three most important variables are: volume, flow rate magnitude and cough duration. The coughing simulation consisted of three stages:

1. In the first stage, a series of threshold pressures is tested to characterise the relationship between flow rate and threshold pressure. The acquired characterisation is used to inform the following experiment, where the desired flow rate magnitude is attained by setting the relative pressure threshold.

2. In the second stage, the volume of the typical human cough acquired in Section 4.3.2 is determined and a simulation of a cough of similar air volume is performed, hence volume is kept constant. The flow rate is also kept constant.

3. In the third stage, the cough duration and maximum flow rate (but not the total volume) are kept constant between the physiological cough and the simulated one.

4.3.4 Results

The average values and relative standard deviation for peak flow rate and expiratory volume from the experiments are shown in Table 4.6. The mean frequency was 13±3 breaths/min for normal breathing and 7±2 breaths/min for deep breathing.

	Peak Flow Rate (L/min)	Expiratory Volume (L)
Breathing	15.12 ± 3.18	0.46 ± 0.15
Deep Breathing	59.32 ± 22.69	1.40 ± 0.34
Coughing	538.42 ± 109.70	1.24 ± 0.18

Table 4.6: Peak Flow Rate and Expiratory Volume obtained from experiments

The flow rate values for breathing and for coughing found in these experiments match the values reported in the literature [147, 148]. In order to test the ability of our simulator in reproducing human physiological breathing and coughing patterns, an example of both from the set of data acquired was chosen. The representative example chosen for the normal breathing experiment with human subjects is shown in the left of Figure 4.4 and the representative example chosen for the deep breathing experiment with human subjects is shown in Figure 4.5. As can be observed from Table 4.6, Figure 4.4 and Figure 4.5, the flow rate magnitude (60 L/min) for deep

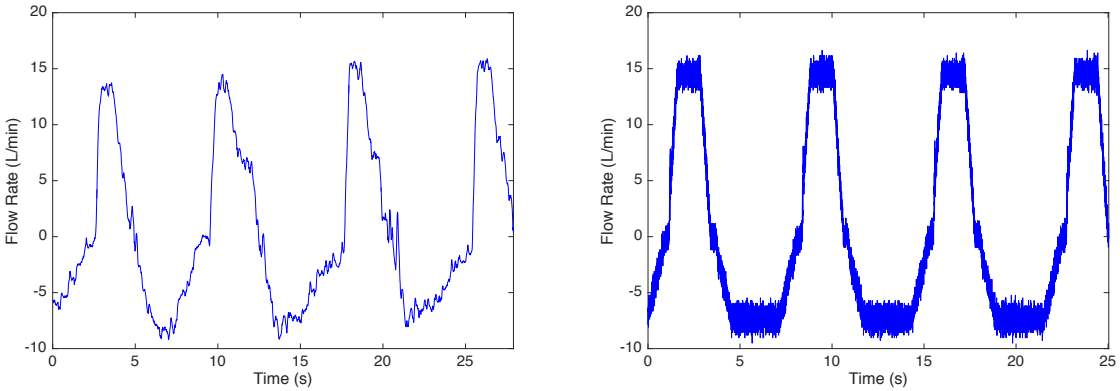

Figure 4.4: Normal breathing simulation. Left: human breathing.Right: simulated breathing

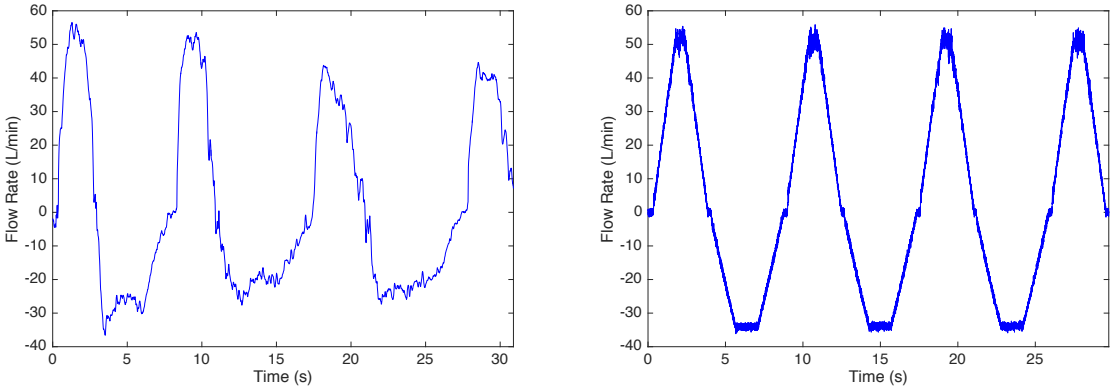

Figure 4.5: Deep breathing simulation. Left: human deep breathing.Right: simulated deep breathing

breathing is approximately four times that of normal breathing (15 L/min). The simulator was then programmed to reproduce each of these patterns.

Figure 4.4 (right) shows simulated flow profiles replicating the normal breathing in the left. Figure 4.5 (right) shows simulated flow profiles replicating deep breathing in the left. The simulator is able to reproduce both the breathing TV of 0.35L and deep breathing TV of 1.5L. The complexity of the physiological profile is not fully reproduced by the simulator. However, the maximum flow rate was replicated in both experiments, together with the inspiration and expiration duration. The overall flow profile provided the important prototypical and highly repeatable respiratory function needed for robotic device development and testing. The simulator successfully attained the reproduction of a simplified breathing and deep breathing pattern.

Prior to simulate coughing profiles from human coughs, characterisation of the system was carried out to obtain a relationship between the system threshold pressure (P_T) to the output flow rate. Figure 4.6 shows a monotonic relationship between pressure threshold and flow rate magnitude. Figure 4.7 shows internal system pressure profile and flow rate for a typical simulated

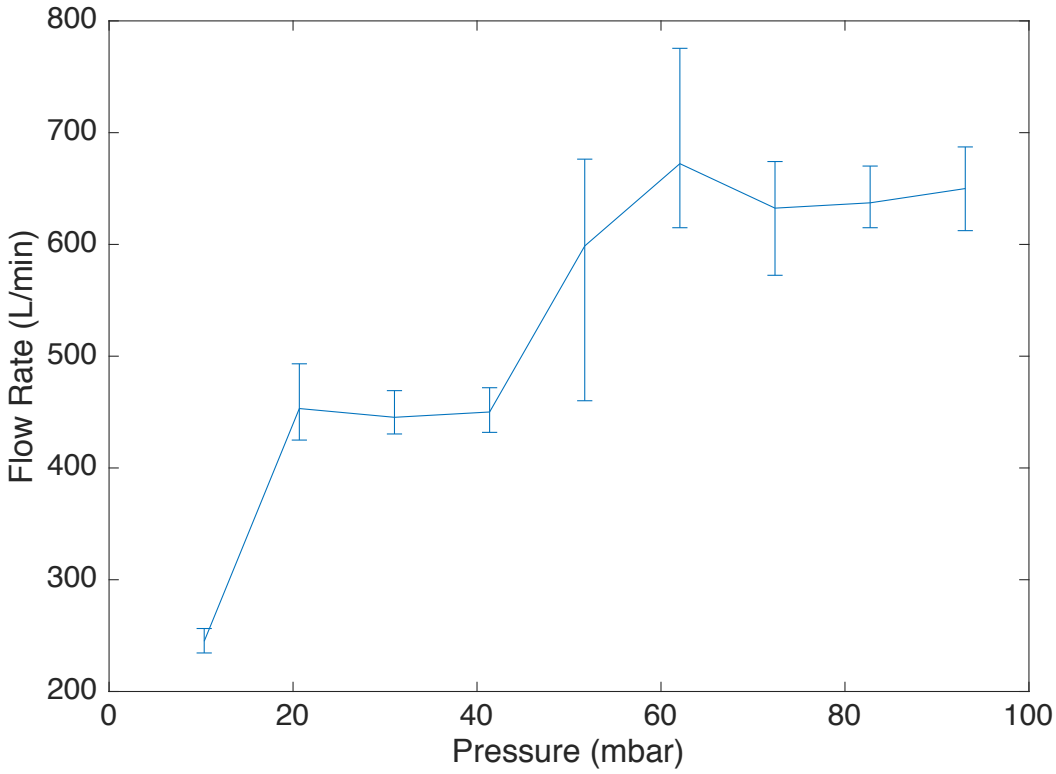

Figure 4.6: Relationship between pressure threshold and flow rate magnitude.

cough. As can be seen from the figure, as soon as (P_T) of 93.08 mbar was reached, the solenoid valve was opened and this generated a flow impulse of approximately 100ms followed by a tail of lower flow for approximately 200ms.

After the characterisation of the system, key parameters of a human cough was simulated. The representative example chosen from the coughing experiment with human subjects is Figure 4.8.

In the constant volume tests (second stage described in section 4.3.3, Figure 4.8) the simulator was able to replicate a cough event of comparable volume (right) to the physiological cough (left). Although the simulator cough profile was over a much longer duration, the maximum flow rate were comparable in the human cough and simulated cough, in both cases it was at approximately 650 L/min.

The cough flow profile was most successfully reproduced in the results of the third stage experiment, shown in Figure 4.9. In this case the simulated cough and the human cough had similar profiles and followed similar trend. The total simulated cough event duration (0.4s) and peak flow rate were similar to the human cough. However after reaching the peak, flow rate decreased gradually in human cough whereas in simulated cough it fell sharply to 0.

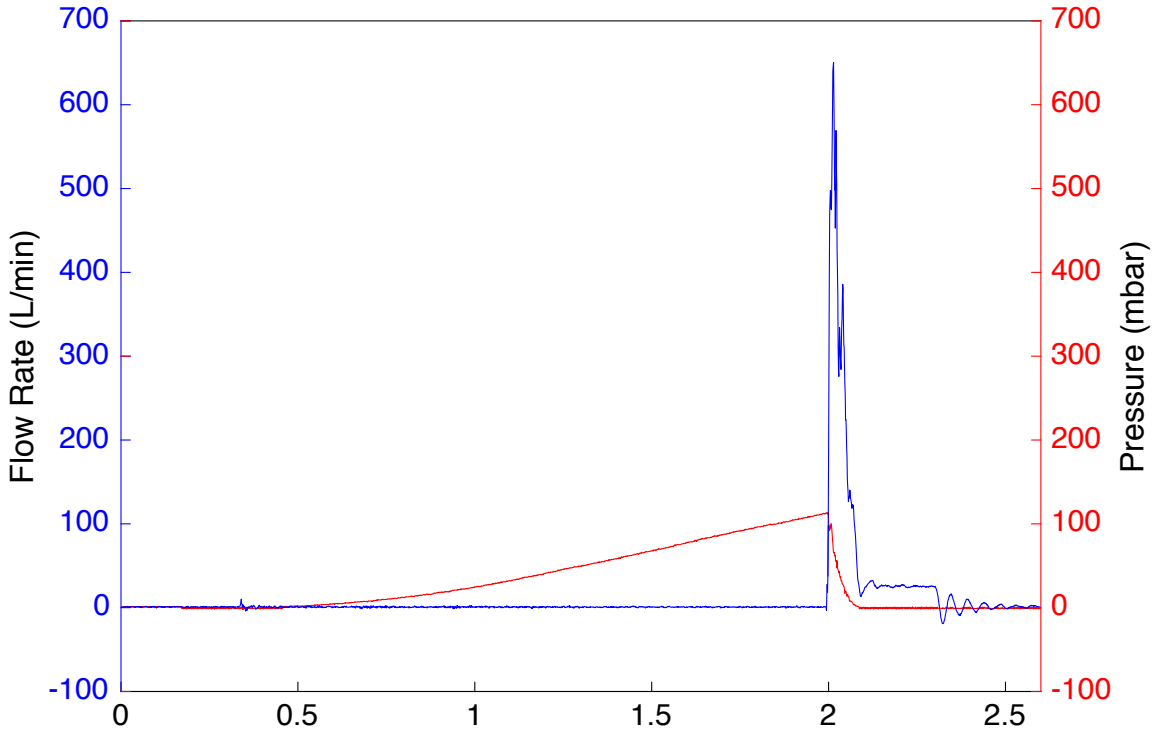

Figure 4.7: Correlation between internal system pressure profile and flow rate.

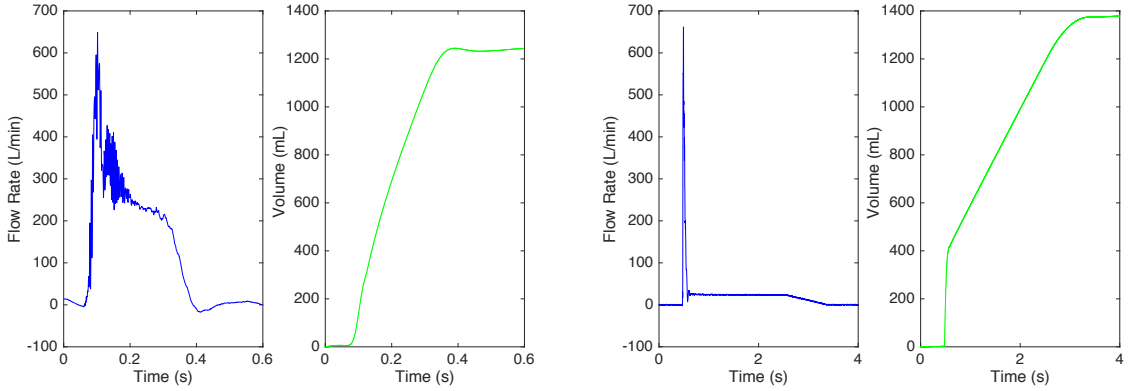

Figure 4.8: Cough expiratory volume simulation. Left: human cough. Right: simulator cough.

4.3.5 Discussion

Respiratory Simulator 2.0 was able to reproduce the frequency, tidal volume and amplitude of the physiological flow rate profiles of breathing and deep breathing. However, the novel simulator was not able to reproduce the higher frequency flow artefacts present in the breathing profiles observed.

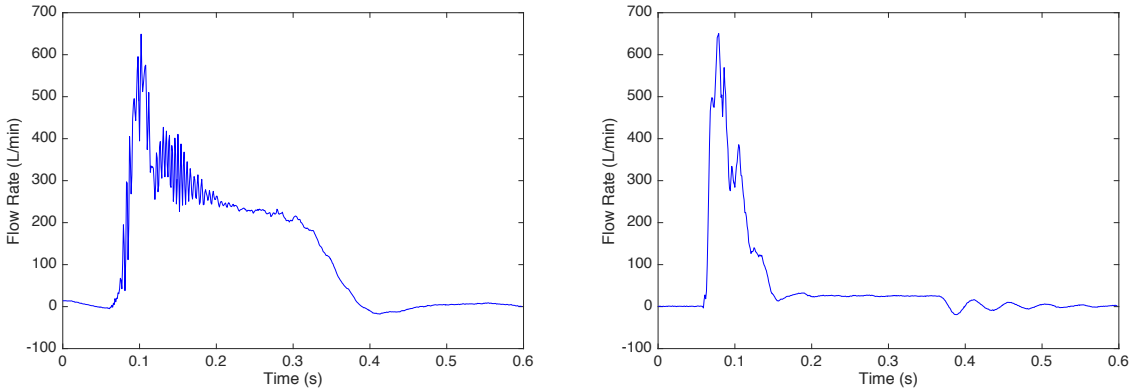

Figure 4.9: Coughing duration simulation. Left: Human cough. Right: Simulator cough.

As regard to coughing simulation, the system described in this section was able to reproduce the volume, flow rate magnitude and duration of a human cough. However in this case, human cough profiles were not exactly reproduced. In the simulator the peak flow reduces faster than in human coughs. A more advanced control system and more investigation into the morphology of coughing process could be carried out to tackle the issue.

It is possible that some of the artefacts observed in the physiological breathing profiles were due to the compliant nature of the human respiratory system and the characteristics and orientation of the muscles driving the human diaphragm and chest. These were not captured by the simulator.

Also, it is possible that some of those non-linearities are the result of the role of the larynx, glottis and upper airway on coughing. Hence designing and building soft robotic devices to mimic the naturally compliant respiratory anatomy is a future aim to make the platform even more suitable to testing and investigating the human airway system.

4.4 Conclusion

This chapter focuses on the design, building, testing and characterisation of a respiratory simulator of the human respiratory system that aims to simulate human breathing and coughing. It was able to reproduce the frequency, tidal volume and amplitude of the physiological flow rate profiles of breathing and deep breathing; and the volume, peak cough flow and cough duration of a human cough.

In the previous chapter, we demonstrated a possible way to improve cough efficiency, with the pressure threshold setting and the solenoid glottis. In this chapter, we found that with the same peak flow rate, a simulated cough produced a much higher cough acceleration compared to a human cough with the solenoid valve. In the attempt of improve the simulation, in the next chapter, we take the first step toward developing a controllable soft valve to replace the rigid

solenoid valve.

CHAPTER 5

ARTIFICIAL VOCAL FOLDS

In the previous chapters, we explored the human respiration system and developed a respiratory simulator to simulate key breathing and coughing characteristics such as peak flow rate and peak pressure. However, although we can simulate peak flow and pressure using solenoid valve as the 'glottis', it is made from rigid materials and therefore does not match the material properties of the actual vocal folds. In this chapter we take inspiration from the human vocal folds and aim to develop a soft valve that can function like vocal folds, and potentially replace them as an implantable device.

This chapter was in collaboration with Hsing-Yu Chen. K.Y designed, fabricated and carried out experiments and analysis presented in Section 5.2.1, H.C led the design and fabrication and carried out experiments presented in 5.2.2, K.Y and H.C carried out the experiments and analysis in 5.3 and together and jointly conceived the ideas of developing various prototypes throughout this chapter.

Main contributions

- Designed and manufactured a novel pneumatic actuated vocal folds prototype.

5.1 Introduction

Vocal folds are crucial to phonation as well as breathing and coughing. Consequently, being able to observe and understand the physiological structures and the dynamic motion of vocal folds is vital for the diagnosis and treatment of voice disorders. Different approaches have been used to tackle the problem.

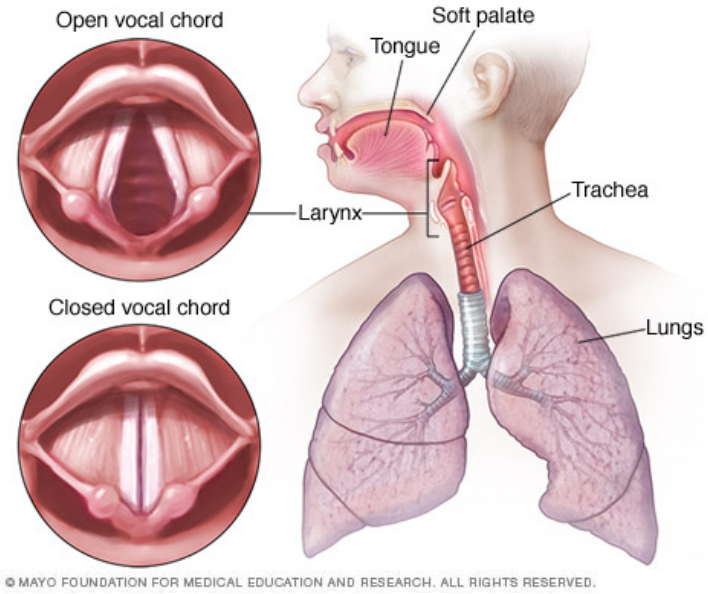

Figure 5.1: Axial view of vocal folds. Image reproduced from [17]

Excised human and canine cadaveric larynges were used to analyse material properties and structural motion of vocal folds, such as muscle strength and tissue compositions in [149, 150], as well as to analyse flow, vocal fold dynamics and resulting acoustics [151, 152]. They were also used as a test platform for newly developed treatments for vocal fold disorders, for example local injection of different materials [153, 154, 155]; phonation with resonance tubes [156] and transoral glottic microsurgery [157]. Results were then used to evaluate the effect of such treatment in humans. High-speed video-endoscopy was used to record and analyse different vibratory patterns and vocal fold positions during sound production to see how acoustic loading can contribute to voice instabilities [158].

Besides excised larynges, synthetic physical models of the larynx including membrane models and rubber casting models, have also been increasingly developed and used. An example of a membrane model is shown in Figure 5.2 (left), where a sheet of 0.2mm silicon was used to mimic the mucosa layer and was driven by water injected into the cavity [18]. Rubber casting models, on the other hand, were created by casting rubber materials into molds of desired geometry. The most widely used geometry was the M5 model as shown in Figure 5.2 (right) [19] and the geometry based on the MRI scan of a larynx [159]. Single layer [160]. two layers [161] and multi-layer models [162, 163] with materials of different stiffness were developed based on a rubber casting method. Characteristics of these models such as vibration patterns, on-set pressures, flow and mucosal wave-like motion were compared with human vocal folds and provide a powerful tool for understanding the myoelastic-aerodynamic theory of phonation [164].

Along with physical models, computational models have also been used to model tissue properties, flow dynamics, and evaluate possible pathologies of laryngeal disorders [165]. One

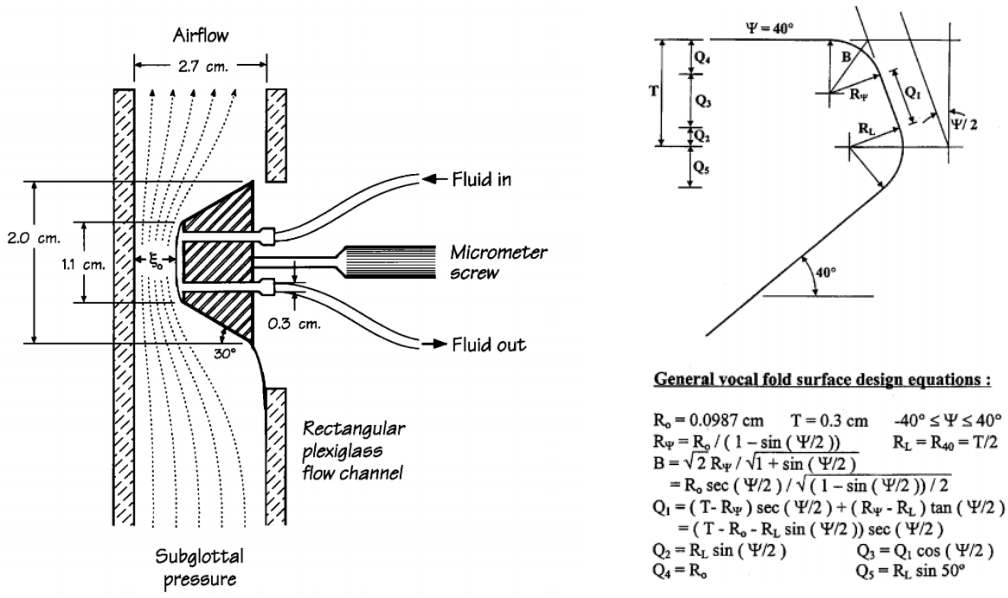

Figure 5.2: Geometry models of the vocal folds.Left: Membrane model [18]. Right: M5 model [19]

mass [166] and two mass [167] model of vocal folds that take into account tissue properties and structures were developed in early years, describing the two layers of materials composing vocal folds [168]. Following which, a three mass model was introduced, adding a body cover layer consisting of muscle fibres and collagen fibres of the vocal ligament [169]. Computational fluid dynamics (CFD) models were therefore widely implemented and coupled with tissue models, using finite element analysis [170]. Pathological models have also been developed to simulate possible conditions of voice disorders such as glottal incompetence [171], vocal fold tissue lesion [172] and unilateral vocal fold paralysis [173].

Although physical and computational vocal fold models have been established and material properties have been quantified, prior physical models have predominently been static or passively actuated. Models either match the physical composition of vocal folds but are static, or can be passively actuated but are not well controlled, or are made from rigid materials. A physical model that can mimic the core function of vocal folds has yet to be developed.

In this chapter we aim to develop a artificial vocal folds prototype that is made from soft materials, can be fully closed and open upon actuation, and have a size that resembles human vocal folds. It should be capable of sustaining airway pressures during coughing.

5.2 Artificial vocal folds with uniform wall thickness

In this section we aim to design a mechanical model that mimics the function of adduction and abduction of vocal folds from an axial view, as shown in Figure 5.1 from the previous section. From the axial view we could see that the opening of the vocal folds leaves an oval aperture.

Using conventional technologies, the opening and closing of this aperture could be achieved using a butterfly valve, check valve, or a solenoid valve that we have used in previous chapters. However, rigid valves are typically bulky and not biocompatible, and therefore have limited suitability for applications that interaction with humans. A soft robotic approach has potential advantages including flexibility and biocompatiility. Within the field of soft robotic actuation technologies, shape memory alloys (SMAs) are limited by poor efficiency and electro-thermal heating-cooling cycles. Electroactive polymers (EAPs), such as dielectric elastomer actuators (DEAs), require advance fabrication techniques. In contrast, fluidic elastomer actuators are lightweight, inherently complaint and low cost [174].

5.2.1 First prototype

The design of the artificial vocal folds took inspiration from the movement of vocal folds but was simplified to mimic two states: abduction and adduction. It was designed to have an oval aperture in their relaxed state and provide a full closure when pneumatically actuated, the principle of the design is shown in Figure 5.3. Figure 5.4 shows the CAD image of the mould design for a single artificial vocal fold using Autodesk® Inventor®. The moulds were composed of an inner piece and one outer shell that fit together. In the first iteration, the mould were designed to have a uniform wall thickness, which required a consistent gap of 2mm around the inner mould. The inner mould had a dimension of 22mm×12mm, which matches the size and the shape of the actual human vocal cord.

5.2.1.1 Design and fabrication

The moulds were 3D printed using Polylactic acid (PLA). Dragon Skin™ 20 silicone elastomer was then used to mould the artificial vocal folds. During the moulding process, the elastomer at the bottom of the mould was cured with an embedded non-stretchable mesh material so that when actuated the curved membrane is the only side to be actuated. The prototype is shown in Figure 5.5.

As illustrated in Figure 5.3, a pneumatic actuation method was proposed to drive the artificial vocal cord. When actuated, the curved membrane would stretch out and therefore mimick the phonation of vocal cords and to have a full closure at the middle.

5.2.1.2 Experiments

To quantify the characteristics of the moulded vocal folds, pressure-volume test was carried out. The vocal folds were placed inside a laser-cut acrylic square mount for better visualisation of its motion, as shown in Figure 5.6, and the device was to be fitted on to the respiration rig described in Chapter 4. A hand-driven syringe was used to actuate the folds and a pressure sensor

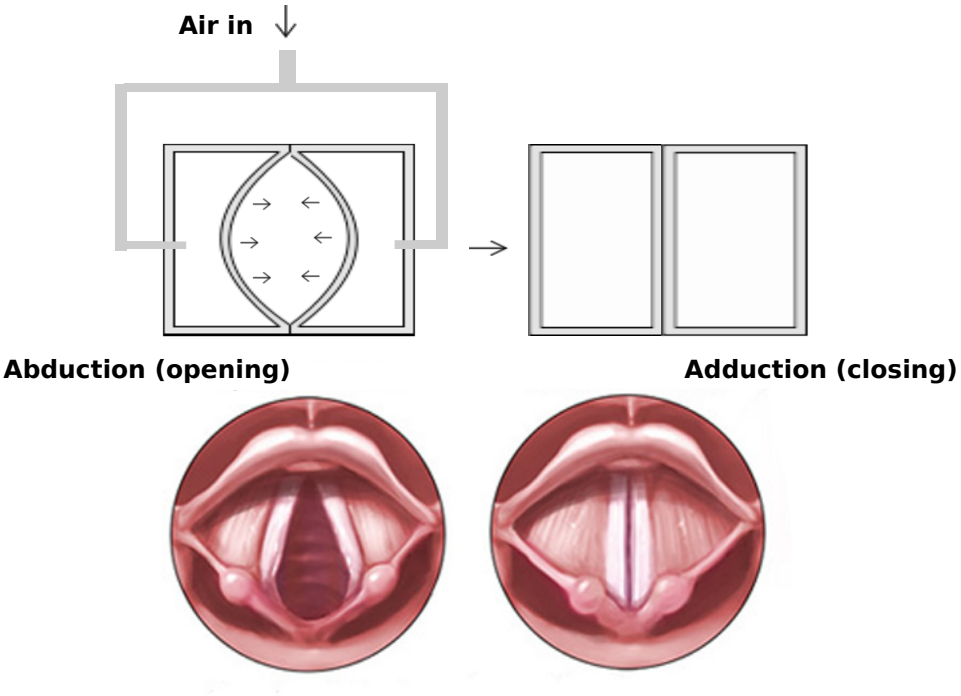

Figure 5.3: Principle of the vocal fold design.

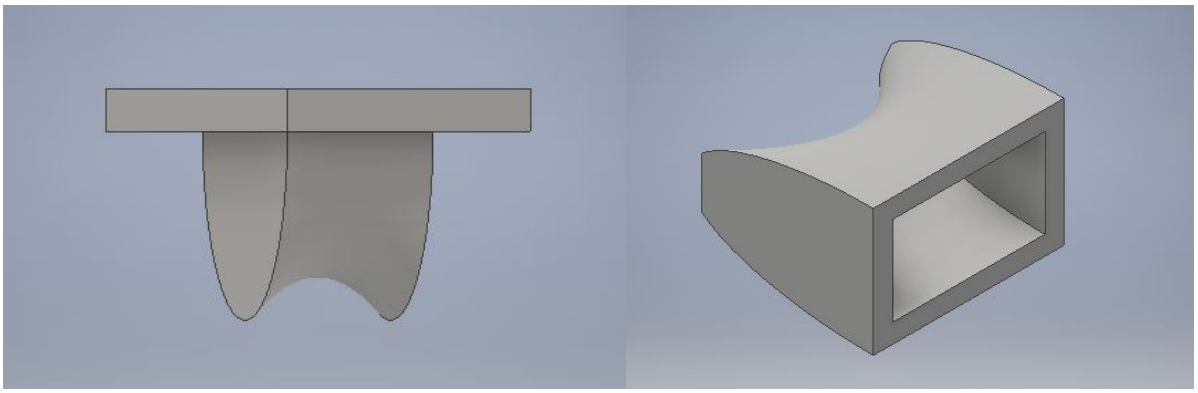

Figure 5.4: CAD image of the vocal fold moulds.

(ExiaIICT4) was connected to measure pressure achieved at different volumes, as illustrated in Figure 5.6.

5.2.1.3 Results

Results shown in Figure 5.7 represents the pressure volume relationship in the moulded prototype. It shows a linear increase in pressure inside the chamber as the volume increases. On the other hand, the aperture size reduces quickly at the beginning and decreases linearly as the injection volume rises from 4-9ml, the decreasing gradient then reduced until the volume reached 12ml.

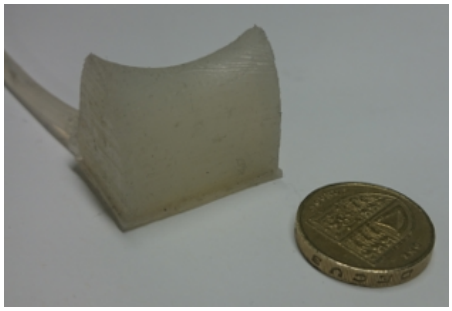

Figure 5.5: The prototype of soft vocal cord

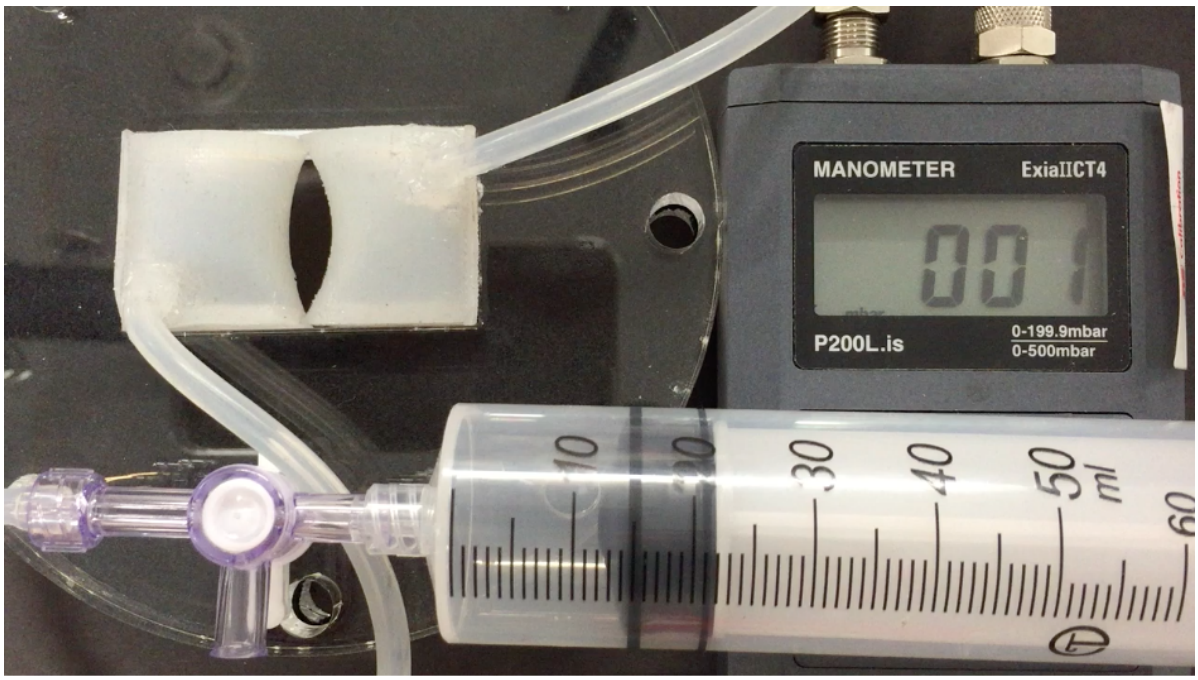

Figure 5.6: Experiment set up for vocal folds with uniform wall thickness.

It was the minimum injection volume needed to enable contact between the two folds. It can be seen from the graph that at 12ml the vocal folds met at the middle with a pressure of 230mbar. Although there are two gaps at the far end of the two folds, the middle of the membranes have met and cannot be actuated further.

As can be seen from Figure 5.7, the vocal folds did not achieve full tight closure as designed. Possible reasons could be that the air was injected from the middle of the folds and thus the middle part of the membrane inflated first, also the further corners had a pointy shape, making them stiffer than the rest of the membrane. Full closure could potentially be achieved by making the corner thinner than the middle, this could be done by replacing the pointy edges by a squared design. To address this issue, we fabricated and tested a second prototype.

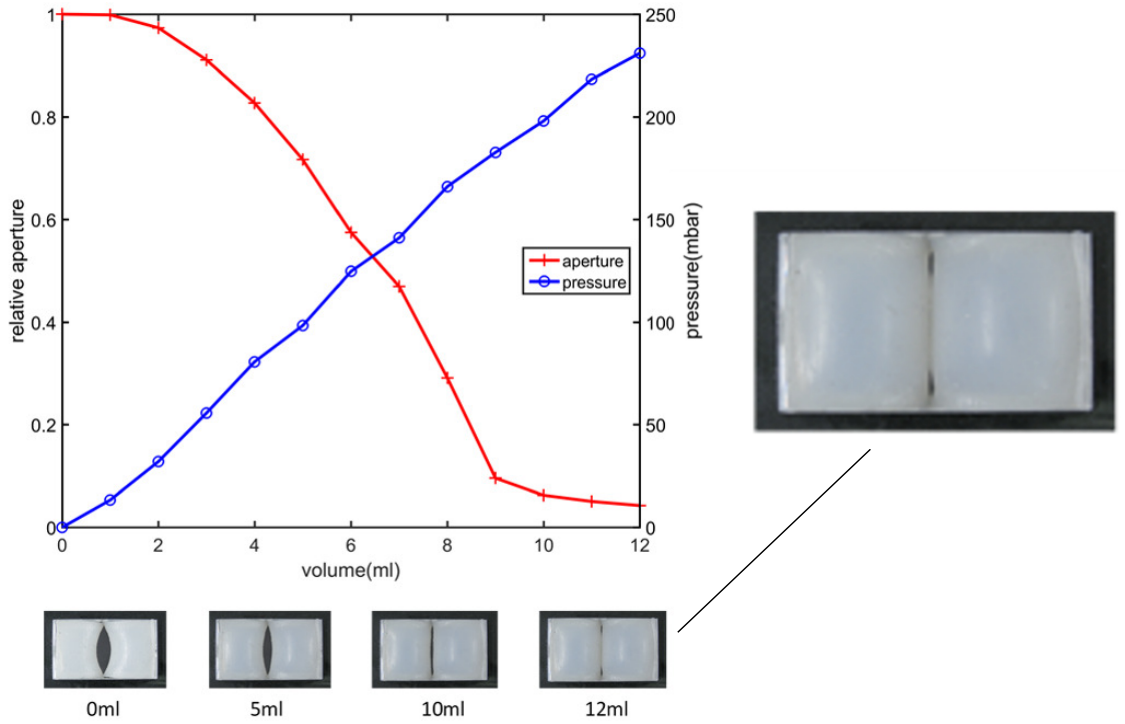

Figure 5.7: Pressure and relative aperture against volume of air inside vocal folds.

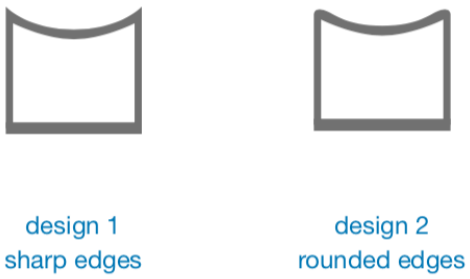

Figure 5.8: Illustrative drawings of the two designs of the artificial vocal folds.

5.2.2 Second prototype

The second mould design was based on the mould described in Section 5.2.1.1 and Figure 5.4. The edges of the outer mould were cut and the corners were rounded to avoid any sharp edges that could cause tear in the moulding process. Illustrative design is shown in Figure 5.8.

5.2.2.1 Experiments

Two prototypes utilising the new rounded-edge mould were made using two different materials: Dragon Skin™ 20 and Ecoflex™ 30. Two prototypes utilising the first sharped-edge design using these materials were also made for comparison. Pressure-volume relationships in each prototype

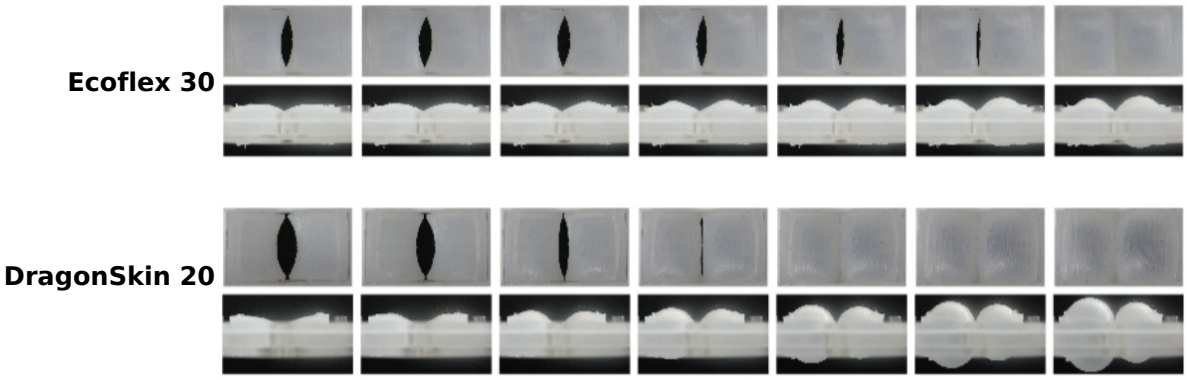

Figure 5.9: Top-down and side views of the relative aperture during inflation of the prototypes fabricated from the rounded-edge moulds.

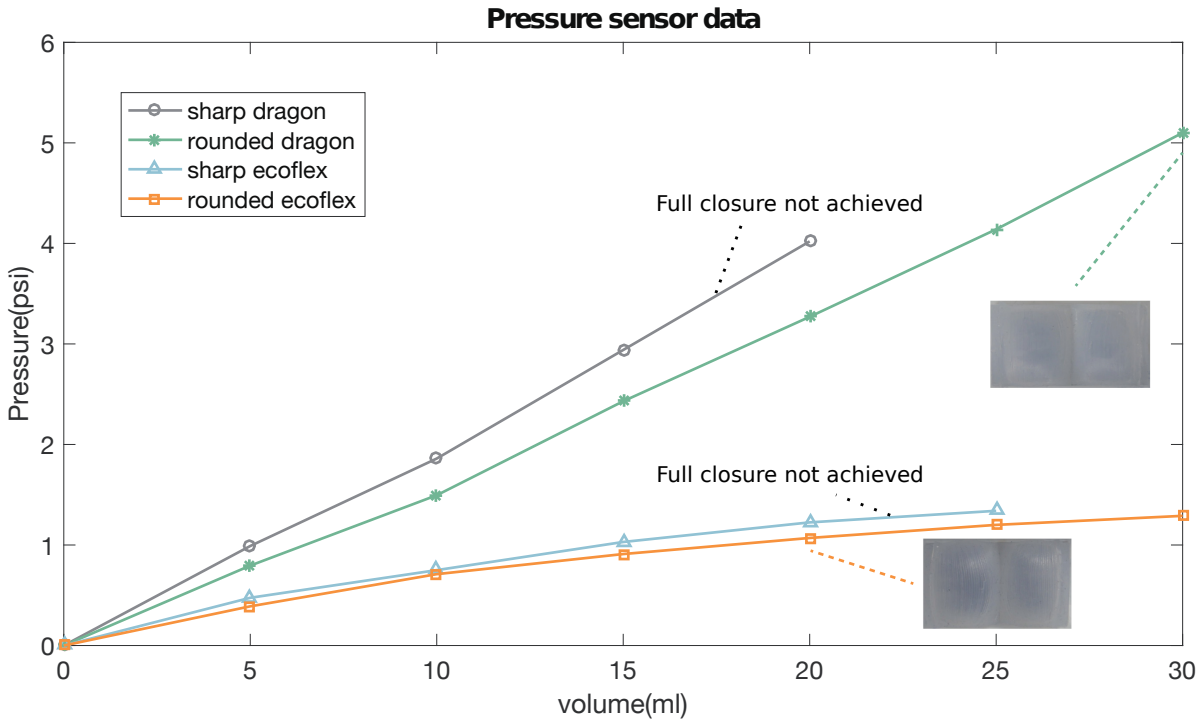

Figure 5.10: Pressure against volume of air inside vocal fold prototypes.

were tested and shown in Figure 5.10 and relative aperture of the prototypes during inflation are shown in Figure 5.9. In the experiment all prototypes were inflated to its maximum tolerance, such that further air injection could cause out-of-plane expansion from side view.

As can be seen from Figure 5.9, both prototypes fabricated from the rounded-edge moulds achieved complete closure upon air inflation. Observations during experiment shows Ecoflex achieved full closure at 1psi (≈ 68.9mbar) and DragonSkin achieved full closure at 5psi (≈ 344.8mbar). Figure 5.10 shows the pressure-volume curves of the prototypes moulded using the two designs for a clearer comparison. The point of full adduction are pointed with dotted lines

Figure 5.11: Illustrative drawings of the three designs of the artificial vocal folds.

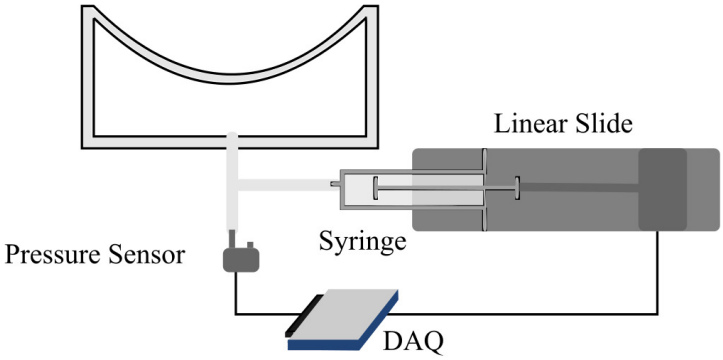

Figure 5.12: Experimental set up for testing the artificial vocal folds with non-uniform wall thickness.

with a top-down view of the fold. It can be seen from the figure that when comparing between two designs using the same material, the sharp edge design had higher internal pressure for the same amount of volume injection, although in prototypes moulded with Ecoflex this difference is small. It is clear to see that DragonSkin prototypes have higher pressure throughout the inflation compared to Ecoflex prototypes at same volume, but the DragonSkin prototype achieved full closure at smaller volume injection than the Ecoflex prototype.

5.3 Artificial vocal folds with non-uniform wall thickness

In this section, we explore the effect of non-uniform wall thickness by modify the curvature of the outer shell, creating a thicker gap in the middle and thinner gap around the edges. The mould was modified from the rounded-edge mould used in Section 5.2.2. Same inner mould was used and the curvature of the outer mould was changed. The resultant vocal folds had 2mm thickness at the middle and 1mm thickness at the edges. Illustration of the designs is shown in Figure 5.11. Ecoflex™ 30 was used to fabricate the prototype.

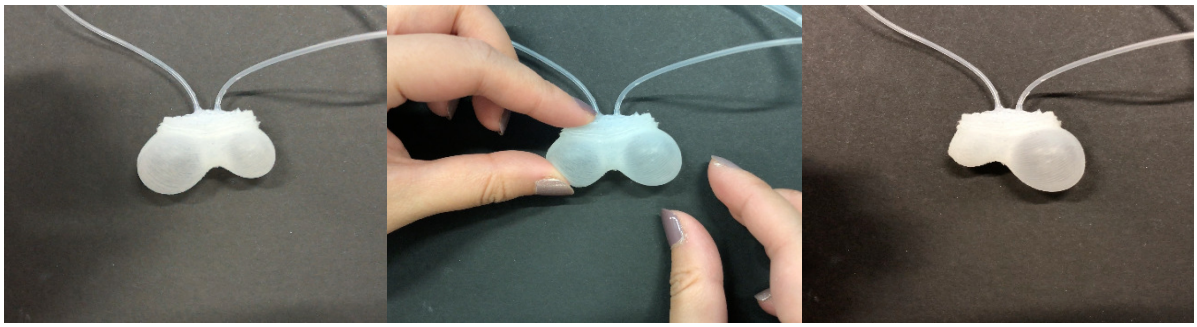

Figure 5.13: State changes in vocal folds with non-uniform thickness.

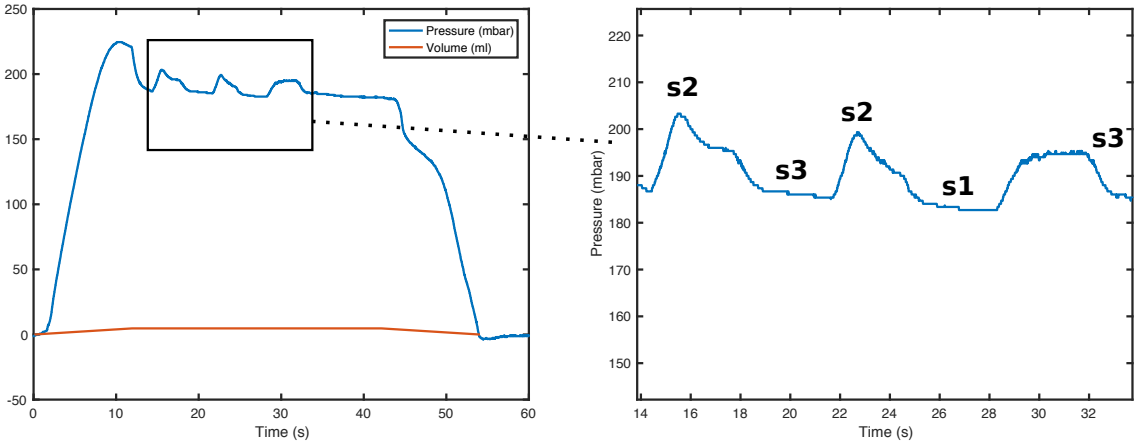

Figure 5.14: Pressure and volume curve of the bistable vocal folds, s1 (State 1), s2 (State 2) and s3 (State 3) mark different states exhibited during the experiment.

5.3.1 Experiments

As shown in Figure 5.12, the syringe was mounted onto a linear slide and pressure was measured using a Honeywell differential pressure sensor (SSCSNBN015PDAA5). Data were collected using DAQ (National Instruments, 6002). The total injection volume was set to be 5ml, after full injection a point force (in this case, finger tip) was applied to the vocal folds to explore the behaviours.

5.3.2 Results

Figure 5.13 includes cropped images from the experiment video and shows the three main states observed. Figure 5.14 (left) shows the full pressure and volume curve during the process, with Figure 5.14 (right) being the enlarged pressure curve in the black box.

During the initial air injection, one side of the vocal folds expanded faster and the vocal folds stabilised at a point where one bump is smaller than the other, which is marked as state 1

in Figure 5.13. The pressure volume curve from 0-14s follows the standard balloon expansion curve. We then applied a point force (State 2, Figure 5.13) on the larger bump and the vocal fold stabilised again at a reversed position of the bumps (State3, Figure 5.13). This represents multi-stable behaviours and was not anticipated. The squared black box in Figure 5.14 shows the pressure change during this process, the force was applied three times. With the applied force the pressure inside vocal folds peaks and can be seen from the three peaks shown in Figure 5.14. As can be seen from the pressure graphs the pressure gradually reduces and reaches a plateau before a second peak. This was because the vocal folds reaches state 3 and stabilised. The third peak is also much flatter compared to the first two, this could due to the prolonged force application time.

5.4 Discussion

In this section we explored two designs of the artificial vocal folds and successfully achieved full adduction in the second design, where the edges of the vocal folds were changed from a pointy, sharp shape to a round shape. Dragon Skin 20 was used to test the first design, although it did not achieve full closure, it shows this material can achieve the pressure needed for artificial vocal folds. In the second design we used Dragon Skin 20 as well as another material Ecoflex 30. From the cross comparison between two different materials with different designs in Figure 5.10, it can be concluded that the key factor of achieving full closure lies the design whereas the pressure-volume relationship is determined by materials.

Mean peak respiratory flow during coughing is 126.4mbar for male, 93.8mbar for female [76] and 30 mbar during speech [149]. The pressure registered in the round-edge vocal fold could reach 344.8 mbar when fully actuated and hence is sufficient for testing breathing, coughing and phonation with physiologically correct pressure and flow.

In the study with vocal folds of non-uniform wall thickness, tests were carried out to achieve full closure, while during the experiment bistability in the structure was observed. A more complete range of vocal folds designs of varied curvature could be investigated for quantifying the conditions to achieve bistability. A force gauge driven by linear slide could be used to replace the finger tip to apply force on vocal folds to remove human errors that could present in the tests.

In the pressure curve graphs, the pressure shows a slight decrease during each plateau period, which could be due to the back pressure driven into the tubes connected to syringe. A check valve could be used in series with the tubes and could therefore reduce back driven pressure and also prevent potential air leaks in connections.

5.5 Conclusion

In this chapter we developed a novel vocal fold model and observed bistability in certain elastomer structures. The round edge artificial vocal folds made from Ecoflex 30 achieved full closure at a pressure as low as 68.9mbar and the structure could potentially reach full adduction at a

lower/higher pressure with different elastomers. Further analysis with different materials could be carried out to quantify the behaviour of this structure, which could then be developed into a pheumatically actuated soft valve. In the test with vocal folds of non-uniform wall thickness, a bistable behaviour was observed. The bistable behavior observed in elastomer inspired future investigation of a bistable balloon actuator in Chapter 7.

In Chapter 3, 4, 5, we investigated the anatomical backgrounds related to larynx and vocal folds paralysis, and have gained better understanding of the problem by building simulators and mechanical models. In the next chapter, we start to explore potential solutions to unilateral vocal folds paralysis.

CHAPTER 6

THE BELLOWS ACTUATOR

This chapter is a collaboration research between Keren Yue, Krishna Manaswi Digumarti and Alice Hayes. The contribution are as follows: K.Y led the dissection sessions and A.H led the development of bellow-shaped actuator. K.Y, KM.D and A.H worked together on the design and tests with the actuators and conducted the experiments on pig larynx.

Main contributions

- Developed a bellows shaped pneumatic actuated implant as opposed to the current implants for vocal fold paralysis.
- Tested the bellows actuator in pig larynx and showed promising results.

6.1 Introduction

Figure 6.1 shows one of the most common treatments for unilateral vocal fold paralysis, Type I Thyroplasty, is where a silastic implant is inserted via a small window on the thyroid cartilage to push the paralysed vocal fold to the midline, and therefore medialise the vocal folds. However, current implants (example shown in Figure 6.2) have fixed sizes with lack of mobility, and as a result patient could experience shortness in breath and difficulties in speaking after the procedure, as discussed in Section 2.2.3 of Chapter 2.

In this chapter we explore the possibility of a pneumatically actuated soft implant that could provide a more robust alternative solution to the current methods. This soft implant is made from soft materials, and can be actuated to variable volumes. We aim to test it in a pig larynx in the final testing stage and the main technical challenge here is the design of the actuator, and determining whether it can push the vocal fold towards the midline position.

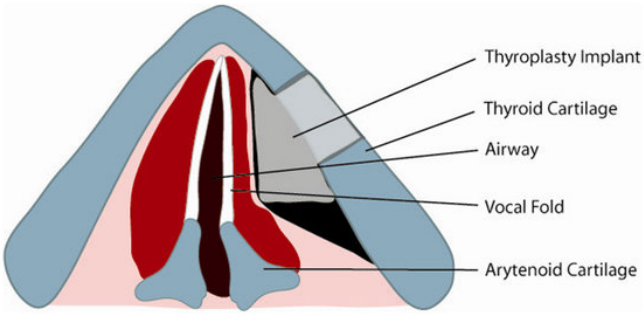

Figure 6.1: An illustration of Type I Thyroplasty, reproduced from [20].

Figure 6.2: Montgomery® Thyroplasty Implant.

6.2 Design and fabrication

Initially the size and functionality of the proposed valve was analysed and determined. Normally, in thyroplasty the window cut into the cartilage is size is approximately 10-15mm wide and 5mm tall, depending on the type of implants. The prototype is to be tested in a cadaverous pig larynx. Moulds were designed using Autodesk® Inventor® and then 3D printed in Acrylonitrile butadiene styrene(ABS). Figure 6.3 shows the 3D CAD image of the moulds. The implant design was inspired by engineered bellows structure which have been used in medical settings such as a manipulator in minimal invasive surgery. A bellow is compressible, can be fluidically actuated and can generate a large actuation strain [175]. However in our design, in order to achieve more effective force distribution directly along the side of vocal folds, unlike the traditional cylindrical bellows design, we aim to deliver a triangular cross-sectional shape when actuated, similar to the Montgomery® Thyroplasty Implant, to provide effective closure of the vocal folds. The actuator was moulded from silicone in 3D printed moulds. ABS was chosen for the moulds because small tolerances and accurate printing were required to avoid rough edges for this design. The moulds

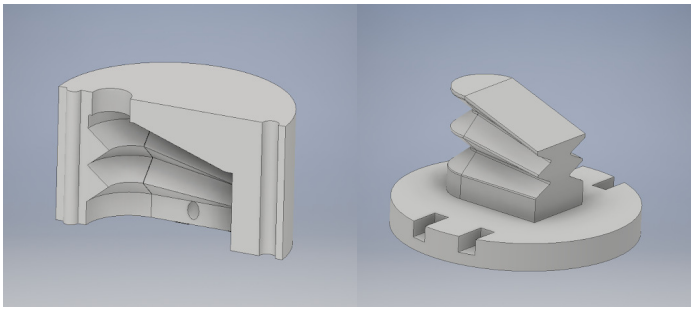

Figure 6.3: CAD image of the bellows shaped implant

Figure 6.4: Bellows actuator. Left: Bellows moulded using injection moulding. Right: 3D printed bellows.

are composed of an inner piece and two outer shells that fit together leaving a consistent gap of 1-2mm around the inner mould. Peg joints and guides were used to ensure that the moulds are aligned. A small hole was added from the inside base to the outside top of the outer shells to allow air to escape during the injection moulding. When the injected silicone comes out of the holes, it was clear that the mould has been fully injected. After 3D printing, the surfaces of the mould were smoothed using wet & dry abrasive paper and the bellows actuator was moulded. Dragon Skin™ 30 was mixed, de-gassed in the vacuum chamber and poured into an appropriately sized syringe. With the mould clamped together with elastic bands, silicone was then slowly injected from the top until it reached the base and came out of the air holes. The mould was then left to cure and bonded onto another flat sheet of silicon as its bottom. The moulded bellow (20mm x 14mm x 16mm, width x depth x height) is shown in Figure 6.4 (left). A 3D-printed bellows actuator (17mm x 11mm x 14mm) was also manufactured by Object Eden 350V printer using as a combination of solid (Vero White) and flexible (Tango Black) materials - solid top, base and inflow tube, flexible bellows. While the tango black flexible material that the Objet printer uses is not very elastic and prone to tearing over time, this design worked well as a concept and showed the potential for a bellows design, shown in Figure 6.4 (right).

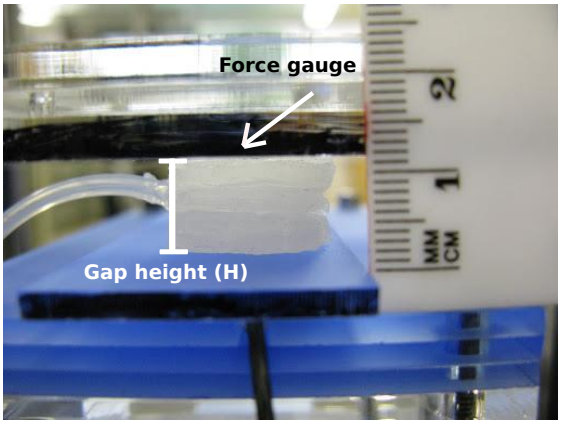

Figure 6.5: Set up used to characterise the force and displacement of bellows actuator.

6.3 Bellows characterisation

To characterise the bellows actuator, the relationship between force, pressure and volume was investigated. As shown in Figure 6.5, the bellows actuator was placed between two parallel plates, which provide a resistive force on the actuator. A load cell was attached to the bottom of the acrylic plate. As gap height H increases, resistive force reduces. This experiment simulates the resistive force that occurs in paralysed vocal folds. The bellows actuator was then connected to a pressure sensor and a hand-driven syringe, with the same connection as illustrated in Figure 5.6 in section 5.2.1.2. Tests were carried out with both the moulded bellows and 3D printed bellows. During experiments, three injection volumes (2.5, 5, 7ml) were tested for both actuators. Four gap heights (H = 12, 13.5, 15, 16.5mm) were tested for the moulded bellows whereas gap height (H = 10, 11mm) were tested for the 3D printed bellows. The gap height were chosen differently for each bellows due to that size difference. Gap height variations were selected so that it covered a physiologically plausible range, starting from the actuator being slightly compressed. Air was gradually pushed into the actuator by the syringe, held for a few seconds, and then released.

Figure 6.6 shows the pressure and force change during inflation and deflation of 2.5ml injection volume with a 12mm gap height. It can be seen from the graph that pressure and force have an approximately linear relationship.. Table 6.1 shows the maximum force and maximum pressure of the moulded bellows actuator under different conditions. It can be seen from the table that with the same injection volume, a larger gap resulted in lower maximum force and pressure. In cases of the same gap height, higher volume injection results in higher maximum force and pressure, as expected. The highest force generated in this actuator was 3.6N and it could retain a pressure of 161mbar. Table 6.2 shows the resultant maximum pressure and force within the 3D printed bellows. It can be seen from the table that the results followed the same pattern as with the moulded bellows: maximum force and pressure increases with volume injection and decrease with gap height. It could exert similar maximum force and pressure as the moulded bellows. The higher stiffness of the Tango Black material could be beneficial in implantation as it meant that

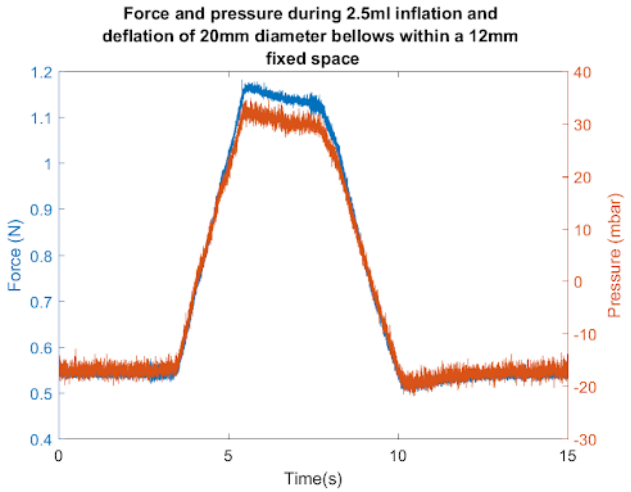

Figure 6.6: Pressure and force change during the inflation and deflation of 2.5ml injection volume.

Moulded bellows			
Gap Height H (mm)	Volume injected (ml)	Maximum Force (N)	Maximum Pressure (mbar)
12	2.5	1.182	31.59
	5	2.166	94.18
	7.5	3.624	161.76
13.5	2.5	0.656	26.76
	5	1.556	85.03
	7.5	2.868	149.46
15	2.5	0.374	19.29
	5	1.063	76.42
	7.5	2.117	139.18
16.5	2.5	0.216	18.59
	5	0.747	73.52
	7.5	1.519	133.29

Table 6.1: Maximum force and pressure generated in moulded bellows.

Objet 3D Printed bellows			
Gap Height H (mm)	Volume injected (ml)	Maximum Force (N)	Maximum Pressure (mbar)
10	2.5	1.299	33.26
	5	2.037	105.95
11	2.5	0.822	34.76
	5	1.532	101.29

Table 6.2: Maximum force and pressure generated in 3D printed bellows.

the actuator could retains pressure without causing shape changing. The moulded bellows, on the other hand expanded out to the sides if the pressure was increased beyond full inflation, but

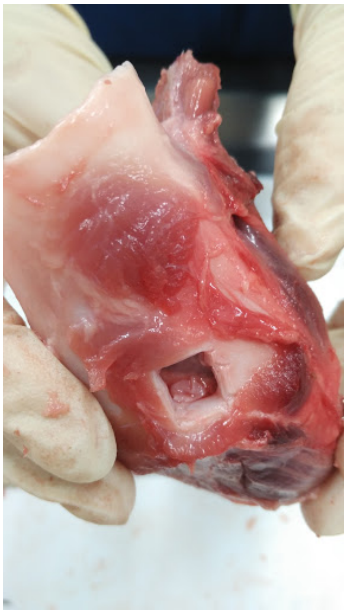

Figure 6.7: Thyroplasty procedure with pig larynx

it has a flexible shape and can be compressed as a whole to fit through a smaller implantation windows as shown in the results graph.

6.4 Experimental procedure with cadaver demonstration

A pig larynx was used as the test bed for proof-of-concept testing of the bellows actuator. A pig larynx was chosen because it has similar structures and material properties to human larynx but bigger in size. A window was cut in the thyroid cartilage in approximately the same position as the incision made during surgery for the implant, as shown in Figure 6.7. The window size was approximately 5mm x 10mm, which is approximately the same as in the surgery.

Firstly, the forces required to push vocal folds to midline were measured, by pushing a cone shaped force gauge through the cartilage window angled towards the back of the vocal folds, such that as the gauge was pushed in, the vocal fold was repositioned to the central line, as illustrated in Figure 6.8. The relationship between force and depth of tissue D are plotted in Figure 6.9. As can be seen, the force required to medialise the vocal fold is very small with an order of magnitude of 0.1N. The force upon loading and unloading both reached a peak at 10mm into the tissue. This behaviour is likely due to the structure of larynx at that position.

We then fitted the bellows actuator into the window and inflated it until the vocal fold was pushed to midline. This was done by driving a syringe by hand.

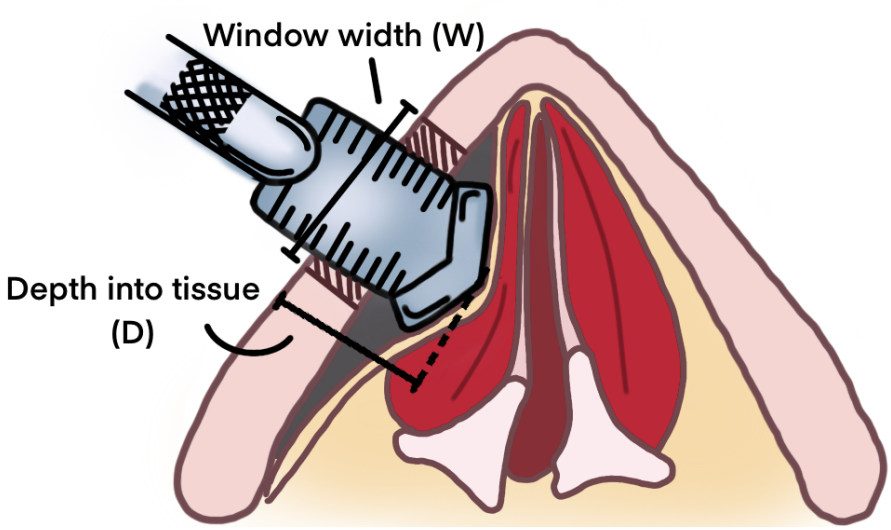

Figure 6.8: Illustration of the force measurement set up. Figure reproduced from [21].

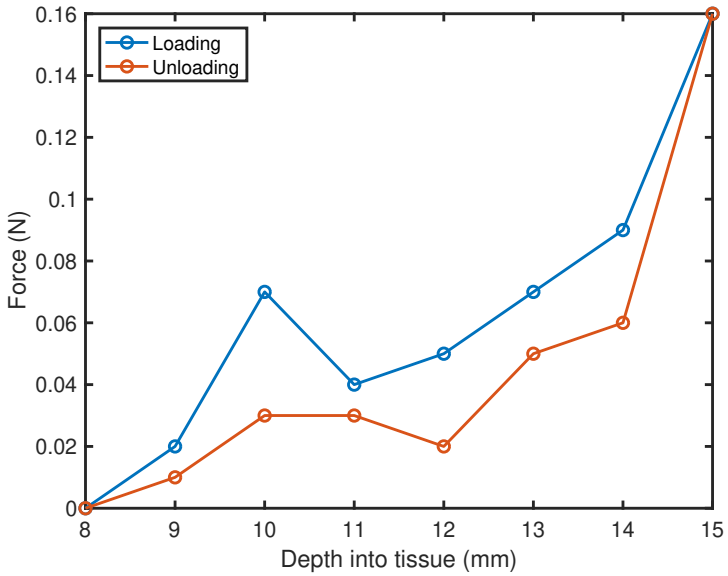

Figure 6.9: Force measured using a cone shaped force gauge.

6.5 Results

Figure 6.10 shows the photo of the bellows actuator fitted into the window on thyroid cartilage. The bellows was 20mm x 14mm x 16mm, larger than the desired size for implanting. However, as can be seen here, it was possible to fit the bellows through the cartilage window as it had a complete soft outer shell and could be compressed slightly.

Figure 6.10: The fitted bellows actuator in pig larynx

Figure 6.11 shows the end result. With an injection of 1 ml, the bellows actuator moves the vocal fold effectively over the midline, as shown between the two white lines.

6.6 Discussion

The bellows actuator takes inspiration from bellows but we re-designed in structure from the traditionally cylindrical shape to a triangular shape so it can push vocal folds towards midline effectively.

From the force gauge experiment we obtain the force required to effectively close the vocal folds. This was tested in a pig cadaveric larynx and the human larynx would have different material properties and would require forces that are different from the pig larynx. But as explored in Section 6.3, the moulded bellows actuator can exert a maximum force of 3.6N and

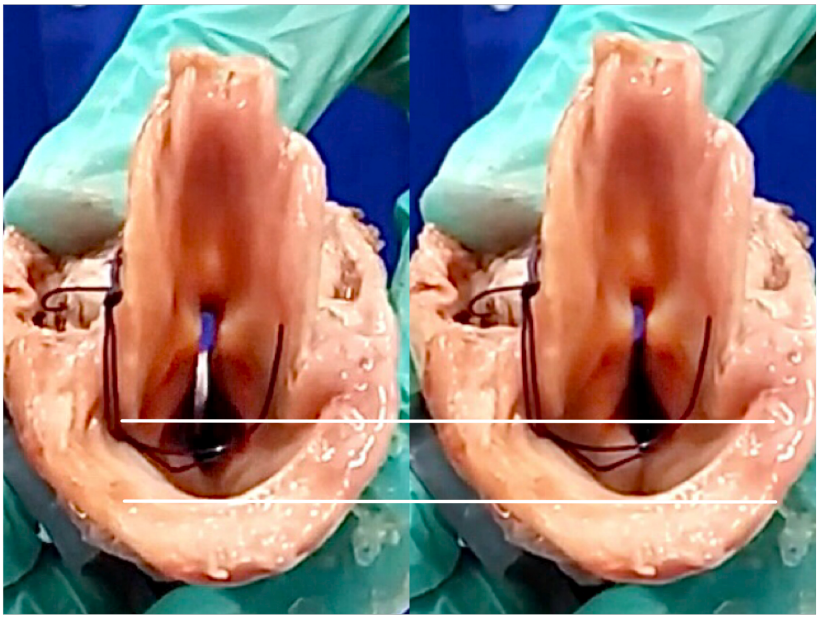

Figure 6.11: Pig larynx showing one side of the vocal folds being pushed to the midline.

should be robust enough, although further tests would be needed to further explore the capability of this actuator.

This bellows actuator provides several advantages over the current implants, as it is flexible and can be made from bio-compatitable materials, and can be actuated to different volumes for different cases of medialisation. By inflating and deflating it according to patients' needs for breathing, coughing and speaking, it is expected to be a more effective implant and to improve the quality of life for thyroplasty patients. Such active actuation requires power and nerve/muscle feedback from the human body, and this could be explored in future work.

6.7 Conclusion

In this chapter we designed and fabricated a bellows actuator as an alternative solution to the current implants for type 1 thyroplasty. The bellows actuator was tested in a pig larynx and could push the vocal folds to midline effectively.

In the next chapter, we will explore the concept of bistability in elastomers and investigate more deeply an actuation method that can lead to the development of a more robust, actively actuated implant for treating vocal fold paralysis.

CHAPTER 7

BISTABLE BALLOON ACTUATORS

In the previous chapter, we observed bistability in the moulded vocal folds structures with non-uniform wall thickness. This suggests that by combining bistablility and soft elastomer actuation, we can realise a device that can actuate utilising surrounding muscles and which can hold its actuated state, or its rest state, without the need for external power sources. In this chapter we explore the bistability of inflated elastomer membranes. We first test fundamental bistability in inflated flat membranes, to explore how different materials affect the snap through behaviour. We then evaluate the stress-strain curve and mullins effect in a single latex balloon; we then explore the bistablility in two connected latex spherical balloons, using pressure as an external driving force. Finally we carried out preliminary tests using catheter balloons.

Main contributions

- Characterised the snap-through behaviour in two inter-connected latex balloons.
- Explored the effect of different materials in snap through behaviour.
- Preliminary test with two connected catheter balloons show promising results towards an bistable balloon actuator that can be used for treating vocal folds paralysis.

7.1 Introduction

Hyper-elastic materials are characterised by their ability to undergo large elastic deformation, although their behaviour exhibits stress softening, hysteresis and cyclic softening during the deformation process [176]. Stress softening describes the irreversible material softening that

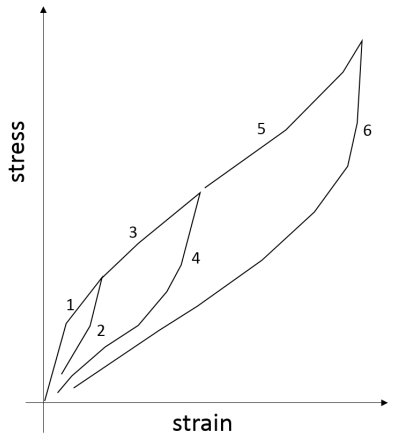

Figure 7.1: Stress–strain responses in filled rubbers showing the mullins effect for three different strain cycles 12, 34 and 56. Figure reproduced from [22]

occurs when the load increases beyond its prior all-time maximum value, such that the next deformation results in lower stress. Hysteresis describes the dynamic lag between stress and strain during loading and unloading, and is due to energy dissipated due to material internal friction and is not permanent. Cyclic softening describes the cyclic stress softening due to the loss of stiffness under cyclic loading conditions. Hysteresis and cyclic stress in filled rubbers are captured in The Mullins effect, introduced by Mullins in 1969 [177]. An example is shown in Figure 7.1. Phenomena associated to Mullins effect have yet to be fully understood, but from cyclic uniaxial tension tests done by Diani et al., it is noted that most of the softening appears after the first loading cycle and that after a few more cycles (up to 10 cycles are reported in literature), the material responses stabilise [178]. Hyperelastic material models have been developed to predict the non-linear stress-strain behaviour of elastomers, such as the Neo-Hookean [179], Mooney-Rivlin [180, 181], Ogden [182] and Gent models [183]. One well known example of a hyper-elastic material is a latex balloon which may undergo a snap through instability and change volume drastically at a certain pressure [25, 184]. Dynamics and instability in tubular or spherically balloons have been studied analytically ([185, 186, 187, 188, 189]) as well as experimentally ([190, 191]). In practical applications, soft pneumatic actuators have been developed utilising tubular balloons [24], for amplified force with small volume by harnessing bistability [25]; by combining dielectric elastomer actuators (DEAs) and inflated hyperelastic membranes [192]. Soft, bistable valves utilising pressure differences in chambers have also been developed which take advantage of the bistability behaviour in a separation membrane [23]. Some of these examples are shown in Figure 7.2.

One main advantage of bistable soft actuators is that they can operate without the need for on board electronics, controllers, or power sources. In this thesis, the main goal is to develop an actuator for treating vocal fold paralysis, where the movement of vocal folds could be simplified into two states: adduction and abduction. Thus integrating bistabilty into the current actuator

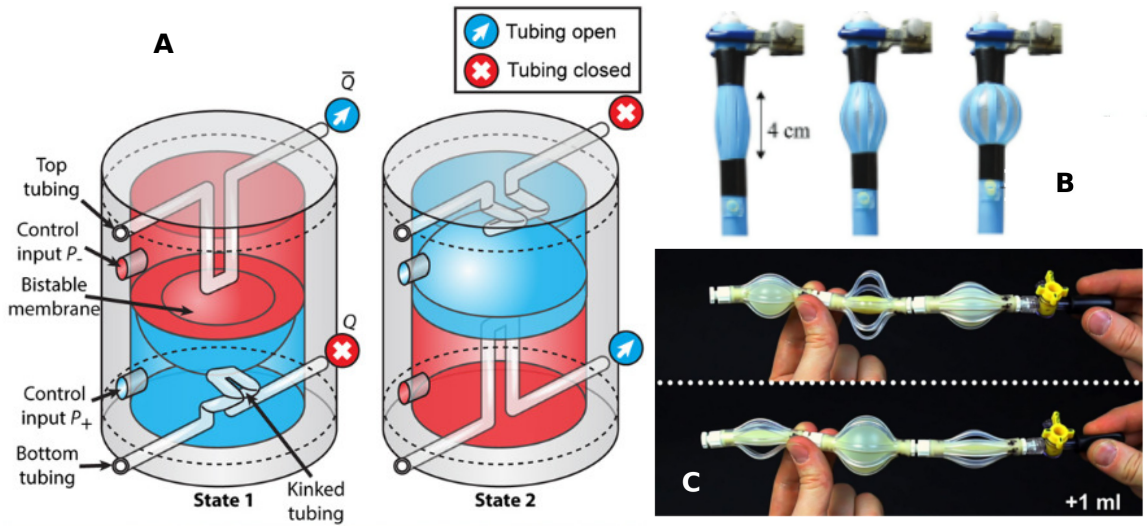

Figure 7.2: Examples of bistable actuator and balloon actuators. A: Bistable valve, image reproduced from [23]. B: The SLiT actuator, image reproduced from [24]. C: Tubular bistable balloon actuator, image reproduced from [25] .

prototype could provide opportunities for a simple self-controlled implant. Theoretical analysis has been done to analyse the bistability in two connected DEA balloons [193] but no practical investigation has been carried out. In this chapter we begin with quantifying basic characteristics in simple inflated membranes. Subsequently we explore bistable behaviours in coupled balloons. Finally we demonstrate the potential of this approach with bistable actuation of commercial catheters. The main technical challenge we address here is to characterise the volume and pressure change to show that in principle it works in the pressure range for our developed bellows actuator in the previous chapter.

7.2 Bistability in inflated elastomer membranes

In this section we further investigate the fundamental characteristics of snap through with hyperelastic materials using a series of inflated flat membranes. This was conducted before tests on more complex solutions (Section 7.3) in which the structure is expected to play a role in bistability and repeatability.

7.2.1 Membrane Characteristics

We first test characteristics of inflated elastomer membranes by looking into the Mullins effect. Five different hyperelastic membranes were tested: Qualatex balloon, condom (Durex), Theraband, VHB 4905 (3M) and VHB 4910. Figure 7.3 illustrates the experiment set up where a sandwich of three acrylic layers and one elastomer membrane was fabricated. Membranes were

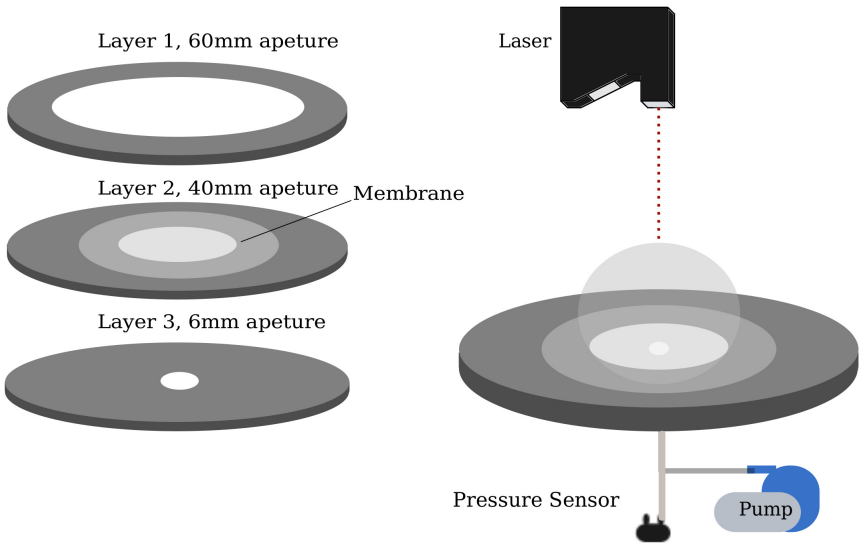

Figure 7.3: Membrane test setup illustration

cut and glued onto layer 2 with as little stretch as possible, which was then clamped between the other two layers. The top and bottom layer plates were made from 10mm thick acrylic and the middle layer plate was made from 2mm thick acrylic. They were all manufactured by laser cutting. Layer 3 had a 6mm hole at the centre, which was then fitted with a push-fit connector that further connects to an air pump (Parker E161-11-050). Layer 2 had a 40mm aperture. Layer 3 had 60mm aperture, the main function of layer 3 was to enhance the airtight assembly in the membrane layer, the aperture size was chosen so that it was larger than the expanded diameter of membrane. Laser displacement sensor (Keyence LK-G402) was used to measure the displacement at the centre of the membrane and a differential pressure sensor (Honeywell SSCSNBN015PDAA5) was used to record pressure change.

Prior to characterisation test, membranes were inflated to displacement = 30mm with video recordings to check whether the membrane expansion were spherical. Figure 7.4 shows a cropped image during an expansion from video. Post-image processing was applied to the image by extracting three sets of random points along the edge of membrane where each set contains three sets of (x,y) points, as presented in Table 7.1. Calculation from 5 sets gave radius with 0.02mm standard deviations. This shows that the membrane expansion was close to uniform and can be treated as spherical, as a first approximation.

	First Set	**Second Set**	**Third Set**	**Mean± SD**
Centre	(-6.43, -0.14)	(-6.38, -0.14)	(-6.43, -0.14)	(-6.41±0.03, -0.14±0.004)
Radius	15.68	15.73	15.70	15.70±0.021

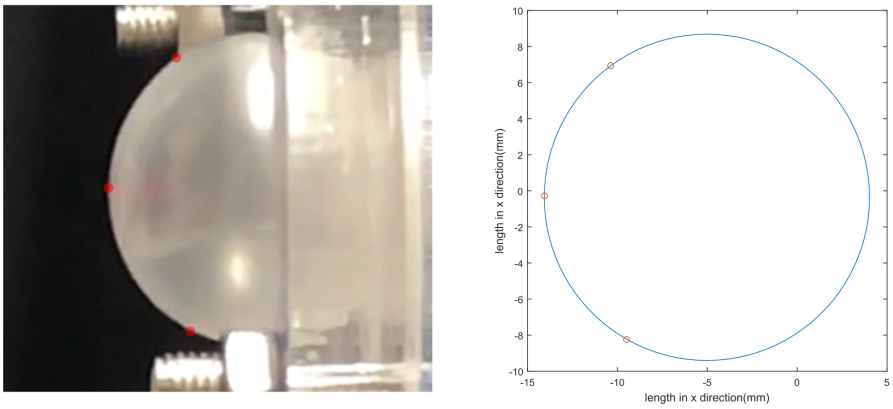

Figure 7.4: Fitting a circle using three points on the membrane surface.

Table 7.1: Radius and centres calculated by extracting random points along the edge of membrane.

7.2.1.1 Mullins effect in different material membranes

We then tested the Mullins effect in membranes. The experimental procedure is as follows:

1. Pump air into membrane until laser displacement records a displacement of 30mm.
2. Immediately release air in balloons.

The process was repeated 15 times, results shown in Figure 7.5. Figure 7.6 and Figure 7.7 show the pressure and displacement for different materials upon first inflation (Fig.7.6) and in the first three cycles (Fig.7.7), where pressure changes were the most significant, as can be seen in Figure 7.5. Inflation pressures at first three cycles are tabulated in Table 7.2.

As can been seen from Figure 7.5,7.6, 7.7 and Table 7.2, VHB 4910 had the highest inflation pressure, followed by VHB 4905, Qualatex balloon, Theraband and condom. It also took longest time to reach 30mm displacement and had the slowest unloading speed among all materials. This could be due to its high viscosity. Among all materials, condom had the fastest loading and unloading response with very small stress softening effect upon the first three cycles.

	Cycle 1	**Cycle 2**	**Cycle 3**
Balloon	156.7	138.1	134.4
Condom	48.15	47.52	46.85
TheraBand	120.6	92.66	90.84
VHB 4905	204.1	179.2	171.8
VHB 4910	327.7	286.5	272.2

Table 7.2: First peak pressure (mbar) at first 3 cycles.

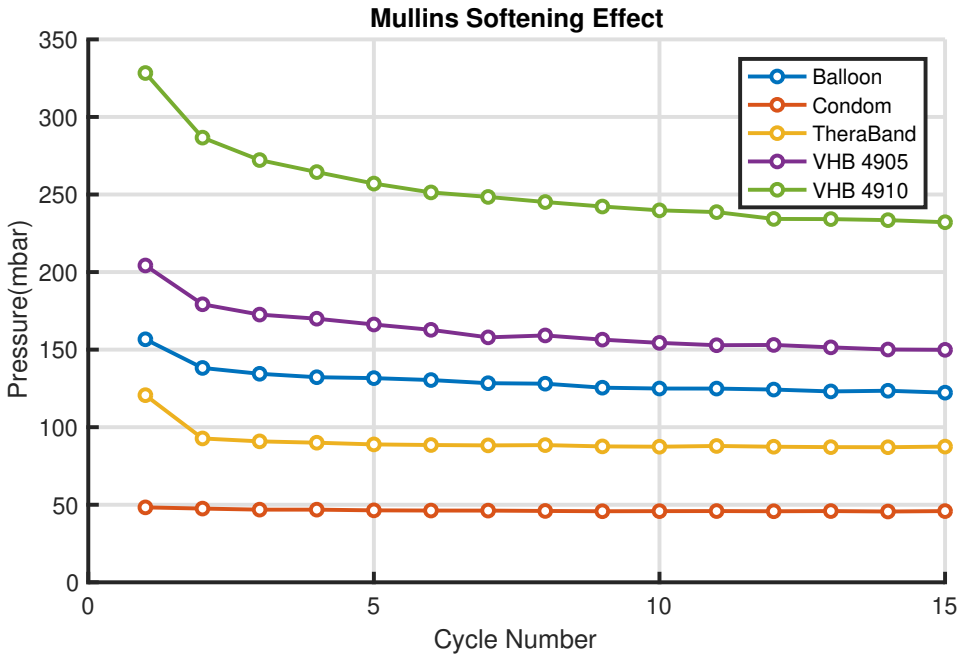

Figure 7.5: The Mullins effect of five membranes in the first 15 cycles of inflation.

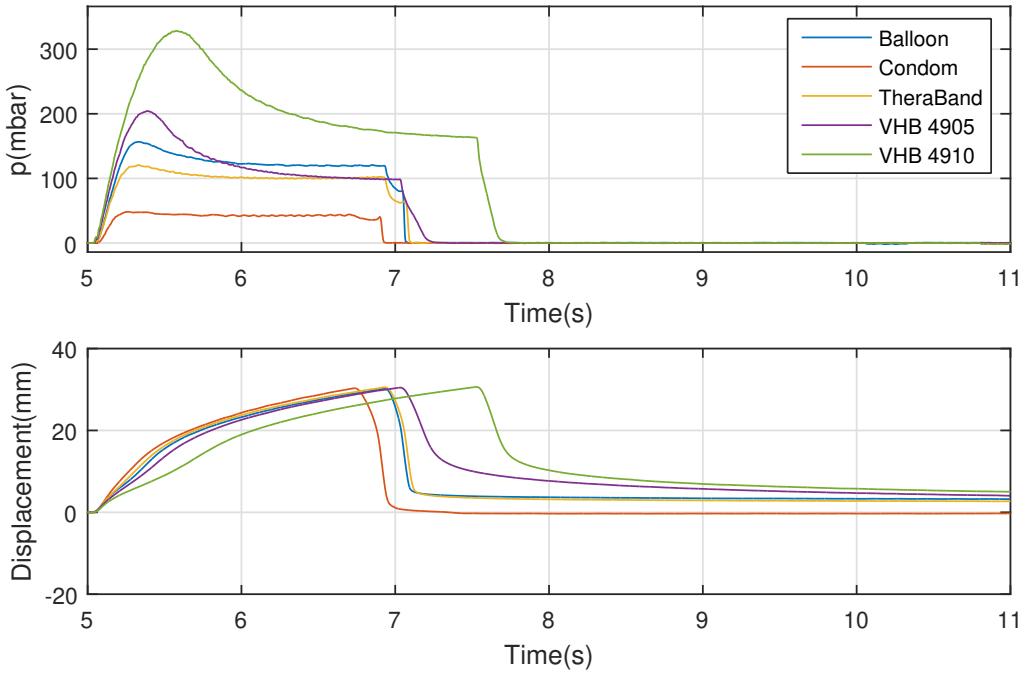

Figure 7.6: Pressure and displacement of 1st cycle in membrane test.

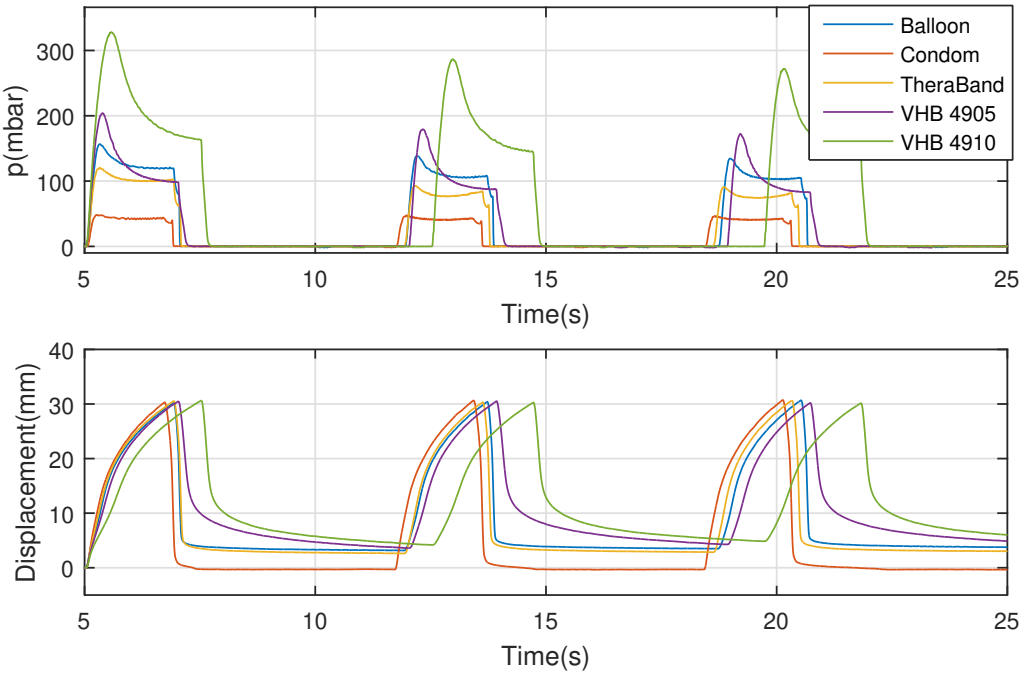

Figure 7.7: Pressure and displacement of first 3 cycles in membrane Mullins test

7.2.2 Snap through using point force

From membrane characteristic tests we found that condom, among all 5 materials, had the fastest response for both loading and unloading, with minimum stress softening effect, and thus would be the best choice for testing the snap-through effect. In this section we investigate the snap through and bistability in two connected inflated condom membrane structures.

Condom membranes were glued onto the same device described in Figure 7.3. Two of such deviced were then connected using pressurised tubes via push-fit connectors. A hand-driven syringe was used to pump air into membranes, a pressure sensor was used to measure pressure changes between the two membranes. A point force was used to drive snap through. This was done by mounting a load cell on to a linear slide, with a 3D printed cylindrical pointer directed to the centre of membrane. The set up is shown in Figure 7.8.

100ml of air was injected into dome actuator by hand. Then the linear slide moved the load cell and pointer towards the inflated membrane, this is controlled by an Arduino through Matlab. The linear slide was stopped once snap through effect was observed. The laser displacement sensor was pointed towards the un-inflated membrane side. Pressure, force and displacement during the process were recorded using a National Instruments data acquisition device and shown in Figure 7.9.

As can be seen from Figure 7.9, upon inflation with 100ml air, the un-inflated membrane side inflated slightly, the displacement then dropped and stabilised at 10mm of displacement.

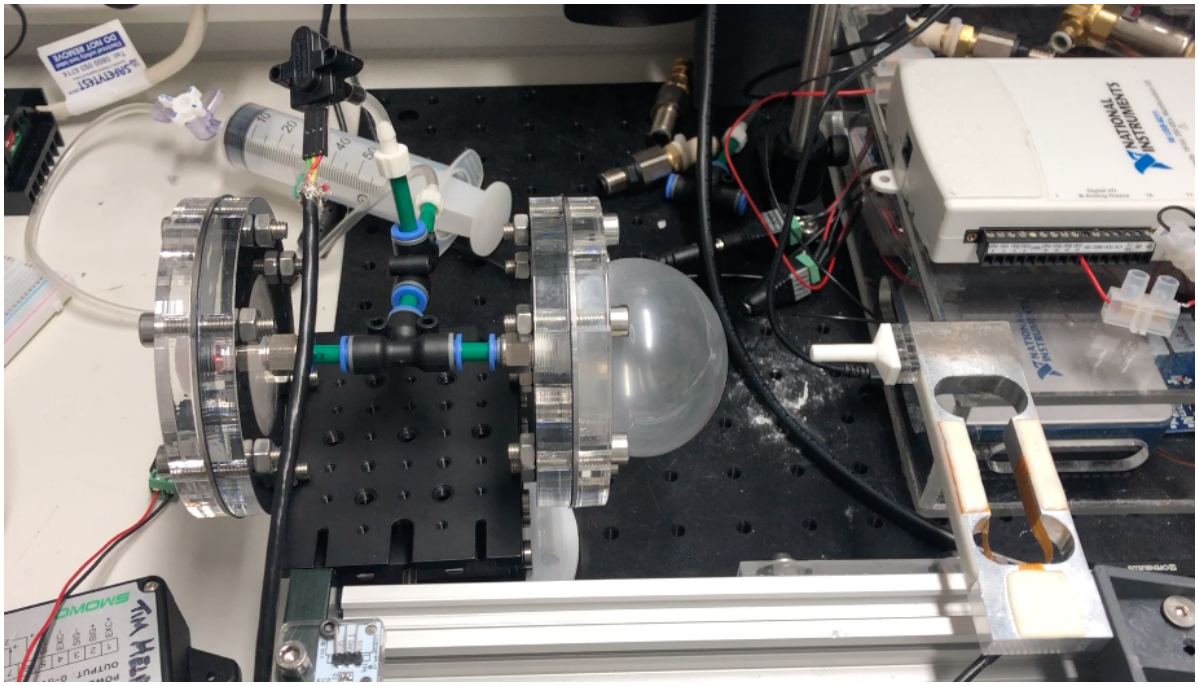

Figure 7.8: Photo of the experiment set up of snap-through upon point force exertion.

This represents the first stable point where the other membrane was stretched out and became a dome completely. The inflation pressure was 19 mbar. The pressure between the two membranes peaked again at snap-through point at 18 mbar (approx. 43sec) and stabilised again quickly, the time taken for snap through, from displacement = 10 mm to 40 mm, was only 1.5 seconds, with a force required of approximately 1N.

The point of snap-through phenomenon was shown by frames in Figure 7.10. As can be seen from the photos, after reaching snap through pressure, air moved from one inflated membrane (right) to another (left) spontaneously without additional force.

7.3 Bistability in two connected balloons

In this section, we explore bistability and snap-through in two connected latex balloons. We start by evaluating the stress strain curve and Mullins effect in a single latex balloon. We then explore snap through behaviour by placing one balloon into a pressurised chamber and the other in atmospheric pressure. Pressure was used as a driving force to transition between stable states. Qualatex balloons (product 43552) made with clear latex were used in experiments carried out in this section.

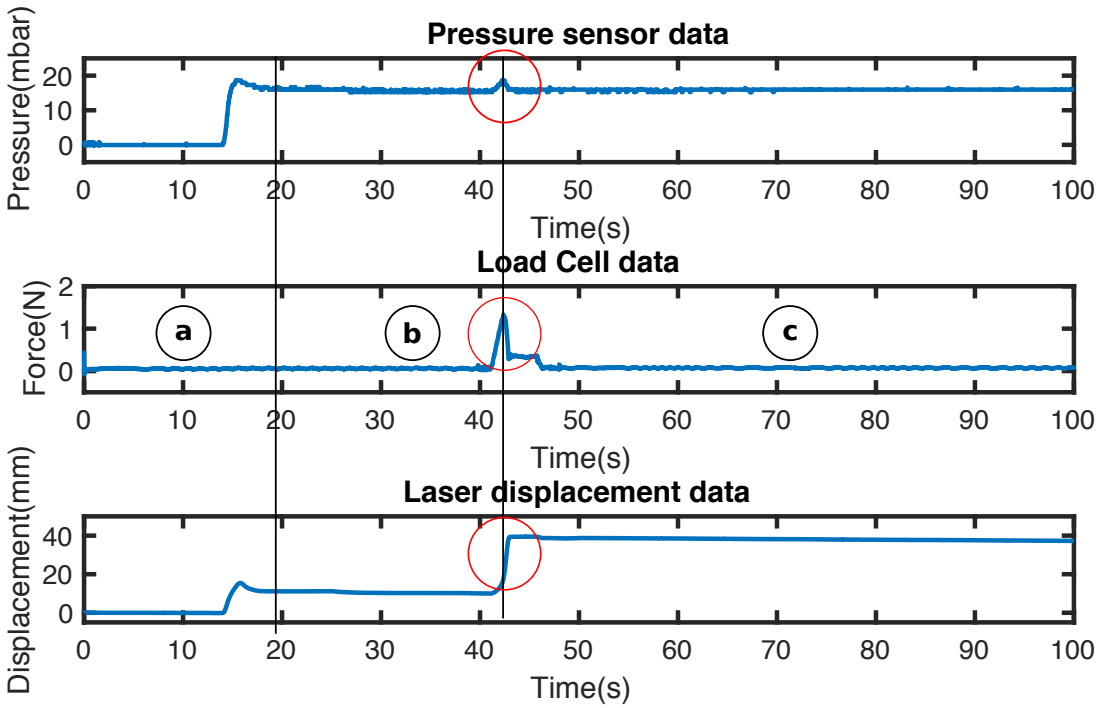

Figure 7.9: Snap through using condom as membrane. Red circle marks the snap through point. a) Inflation of the membrane. b) Forced applied to enable snap through. C) Snap through achieved.

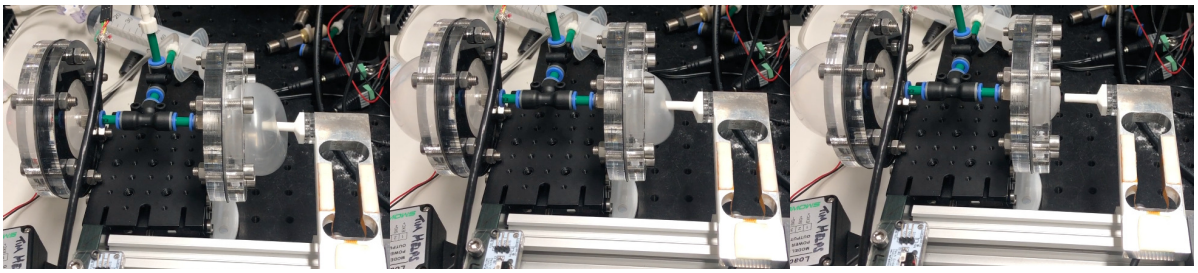

Figure 7.10: Frames capturing snap through behaviour in dome actuator.

7.3.1 Single balloon characteristics

To investigate the characteristics a single latex balloon exhibits, firstly we measured the pressure volume curve. The balloon was inflated to strain ϵ=1 and deflated 15 times using an air pump prior to experiment to remove the Mullins effect according to literature [178]. Strain is defined as $\epsilon = \Delta L/L$, where L is the pole height of a new balloon. It was then inflated at a constant rate until it ruptured or exploded.

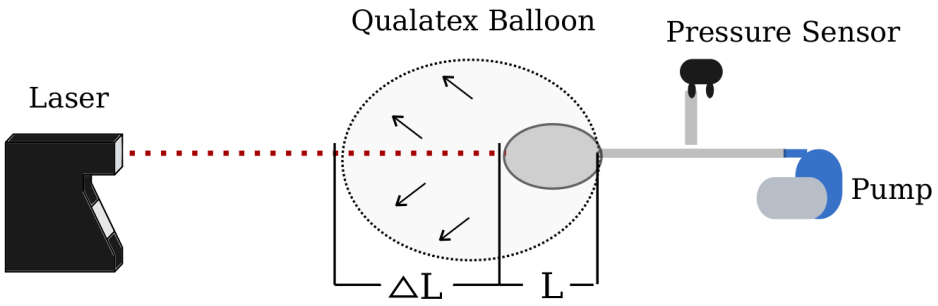

Figure 7.11: Mullins Experiment Setup

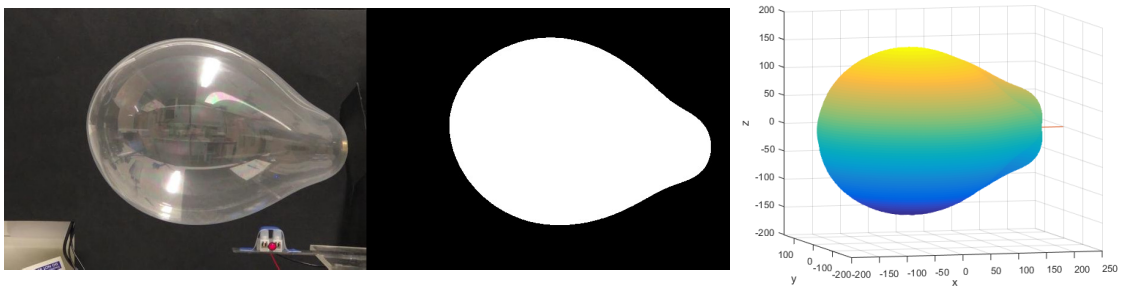

Figure 7.12: Sample image processing for one image, showing reconstructed 3D model (right).

7.3.1.1 Pressure volume curve

The experiment set up is illustrated in Figure 7.11. An air pump (Parker E161-11-050), a pressure sensor (Honeywell SSCSNBN015PDAA5) and a latex balloon were connected using a 3-way push-fit valve. The latex balloon was securely wrapped around the valve using two zip ties. A laser displacement sensor (Keyence LK-G402) was placed in line with the latex balloon, with the laser pointing at the tip of the latex balloon.

Volume inside the balloon was estimated by post image processing using MATLAB, sample processing of a single frame is shown in Figure 7.12. A 3D balloon was reconstructed from the 2D image assuming uni-axial expansion.

Figure 7.13 shows the pressure volume expansion curve of a Qualatex balloon. It can be seen from Figure 7.13 that the balloon has 4ml air volume at rest (pre-inflation). Pressure rapidly rose to its first peak of 95.27 mbar and dipped to 40 mbar before it gradually rose again. It reached breaking point with a pressure of 105.2 mbar and volume of 1418 ml. States of the balloon in the first and break point of the inflation process are circled in red.

7.3.1.2 Mullins effect

We then investigate the Mullins effect in Qualatex balloons by considering two parameters: the maximum inflation strain and the number of loading/unloading cycles. Maximum strain was

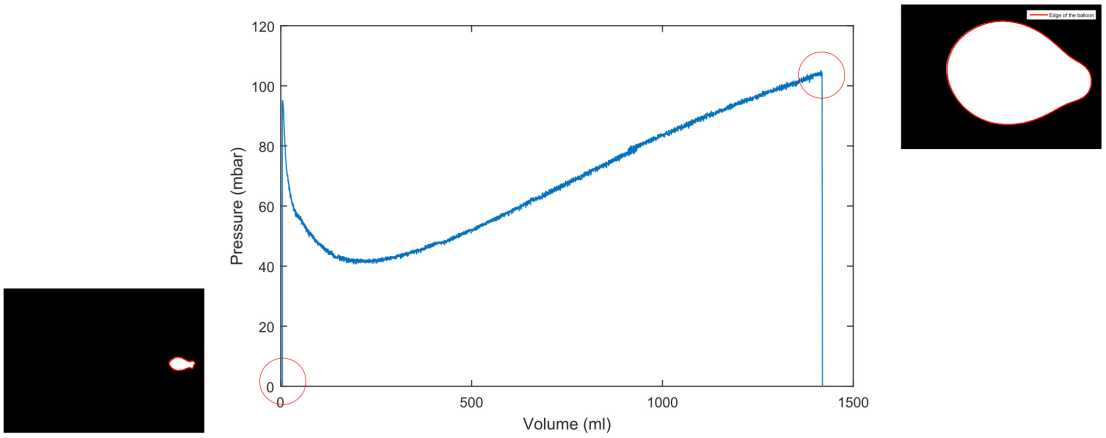

Figure 7.13: Pressure Volume graph of Balloon, from non-inflated to rupture.

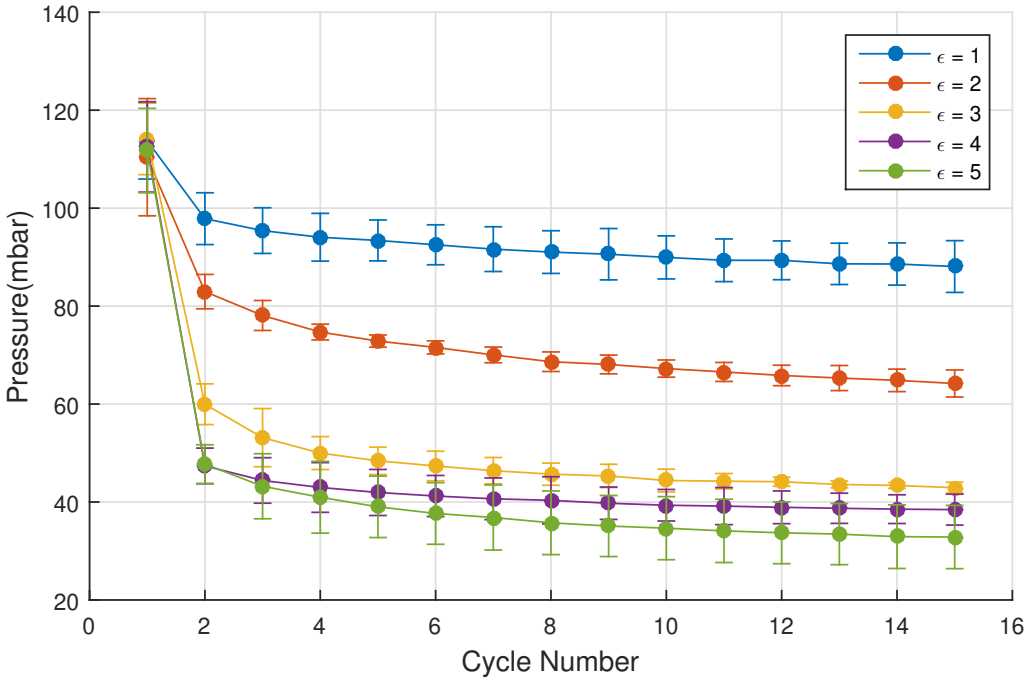

Figure 7.14: First peak pressure of different cycles of mullins effect

varied from 1 to 5, and the number of cycles was chosen to be 15, higher than in the previous literature [178]. The experiment set up was the same as in the previous section (Figure 7.11). A new, unstreched balloon was inflated to a certain strain and then deflated to atmospheric pressure 15 times. For each maximum strain value the process was repeated with 3 balloons.

	Cycle 1	**Cycle 5**	**Cycle 10**	**Cycle 15**
ϵ **= 1**	113.74	93.40	89.94	88.08
ϵ **= 2**	110.40	72.86	67.24	64.20
ϵ **= 3**	114.13	48.40	44.39	42.92
ϵ **= 4**	112.50	41.95	39.34	38.44
ϵ **= 5**	111.75	39.02	34.66	32.85

Table 7.3: First peak pressure (mbar) of Mullins Effect for different ϵ and different number of cycles.

Figure 7.14 shows the how first peak pressure (inflation pressure) varies with cyclic inflation/deflation. Table 7.3 tabulates the mean values of first inflation peak pressure during different cycles. It can be seen from the figure and the table that in all cases the greatest material softening happened between the first and second cycle, and the peak pressure began to stabilise after the 10th cycle, which comply with literature [178]. Comparison between the cyclic softening curve between different strains also shows that larger strain results in greater material softening. Percentage stress softening after 15 cycles was calculated and presented in Table 7.4, showing the stress softening was more than tripled when the balloons were stretched to ϵ = 5 compare to ϵ = 1.

Strain(ϵ)	**1**	**2**	**3**	**4**	**5**
Percentage Softening(%)	22.56	41.85	62.39	65.83	70.60

Table 7.4: Percentage softening throughput Mullins cycling, for 15 cycles.

7.3.1.3 Discussion

In this section we characterised the Qualatax balloons that are to be used in bistability experiments. The pressure curve and Mullins effect was measured and analysed. The Mullins Effect describes the stress softening effect in elastomers. As strain increases, the stress softening effect becomes more significant. Results complied with existing literature. As can be seen from the Mullins test, the Qualatex balloons have very similar, although varied, inflation peak pressure at first cycle, showing that the quality of balloons were relatively consistent and could be comparable as replicates for experiments. In following experiments we pre-stretch the balloon 15 times prior to any tests to remove any influence caused by the Mullins effect and therefore ensure balloons have constant inflation peak pressure.

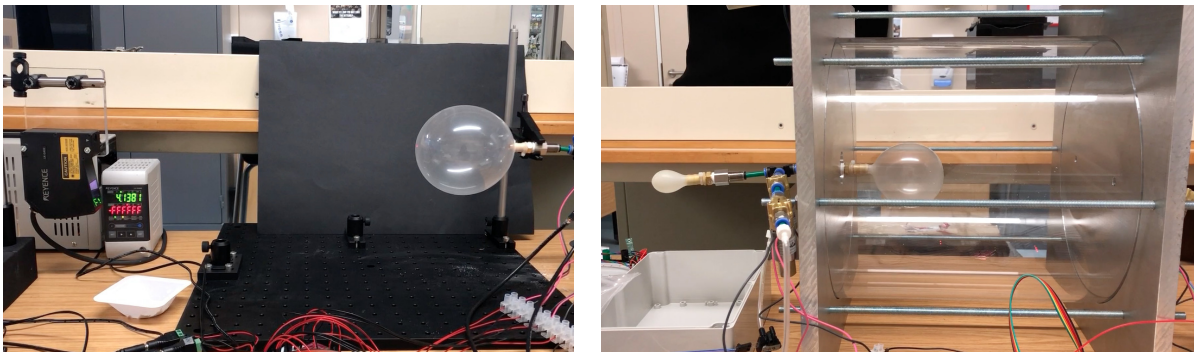

Figure 7.15: Photo of the experiment set up to test bistablility in two connected balloons. Left: balloon outside the chamber with laser. Right: balloon inside the chamber.

7.3.2 Snap through in two connected balloons

In this section we explore bistability in two connected balloons, using pressure as an external driving force. An air-tight pressurised chamber was designed and built to ensure that when actuated, pressure acting on balloon surface is uniform. The pressure chamber can also simulate the muscle contraction in human body, such that when the actuator is implanted it would experience pressure from its surroundings.

7.3.2.1 Experiment procedure

Experiment set up is shown in Figure 7.15 and illustrated in Figure 7.16. Two balloons, each wrapped tightly around connectors using zip-ties, were connected via a 30cm high-pressure tube. One balloon, Balloon$_{in}$, was placed inside pressure chamber and the other balloon, Balloon$_{out}$, was placed in atmospheric pressure, with a laser displacement sensor (Keyence LK-G402) pointing at its pole. Two pumps were used to pump air into balloons (Parker E161-11-050) and the pressure chamber (Parker D743-21-01) respectively. Two differential pressure sensors (Honeywell SSCSNBN015PDAA5) were utilised to measure pressure inside chamber ($P_{chamber}$) and pressure inside balloons ($P_{balloon}$). Since mutiple states were required in the bistability experiments, solenoid valves (SMC VDW250-5G-2-01F-Q) were adopted throughout the connections for switching connections (eg: connecting to pump or to open air). The system was controlled using a data acqusition device (National Instruments, 6002) and data were collected by a second device (National Instruments, 6211), simultaneously through MATLAB.

Both balloons were pre-streched 15 times to ϵ = 1.5 and the experiment procedure was as follows:

1. Pump air into Balloon$_{in}$ while the pressure chamber was opened to air, two balloons were not connected at this stage with solenoid valve in between closed. Duration was set to be 20 seconds.

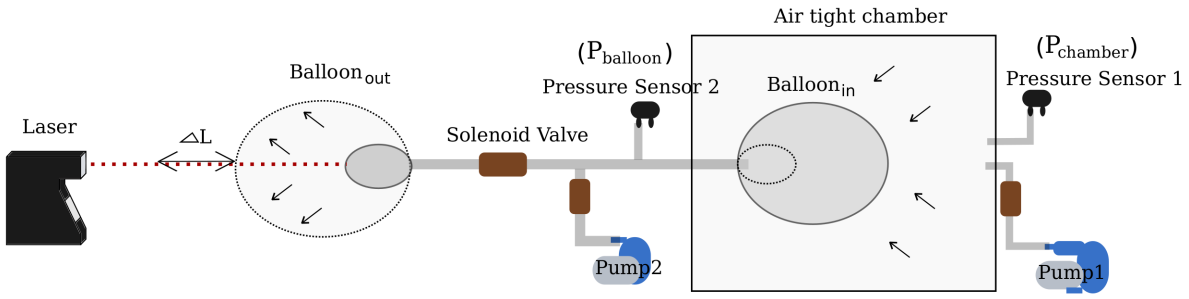

Figure 7.16: An illustration of experiment set up to test bistablility in two connected balloons.

2. Open the valve between two balloons so that they are connected. Duration was set to be 5 seconds.

3. Pump air into the pressure chamber. Driving the air inside Balloon$_{in}$ to flow to Balloon$_{out}$. Pumping continues after snap through. Duration was set to be 30 seconds.

4. Open pressure chamber to air so that pressure in chamber gradually falls to atmospheric pressure. Duration was set to be 30 seconds.

5. Release air in balloons. Duration was set to be 15 seconds.

7.3.2.2 Snap-through behaviour

Snap through behaviour describes an instability of a structure, where the displacement suddenly changes from one configuration to another, even without an increase of the external load. This phenomenon was observed in the two connected balloons and data captured is shown in Figure 7.17. It shows the pressure and displacement change during the experiment procedure discussed in the previous section, with each line marking the end of each step. (Step 1 before yellow line, step 2 between yellow and purple line, step 3 between purple and green, step 4 between green and blue, step 5 after blue line.) Figure 7.18 presents crop images showing representative state changes during the experiment.

Because the two balloon were not connected at the beginning, pressure in balloons recorded in step 1 was the pressure occurred inside Balloon$_{in}$ only. As expected pressure inside the two interconnected balloons, P$_{balloon}$ follows a standard expansion curve while P$_{chamber}$ recorded 0 mbar pressure change, and displacement recorded was also 0. During step 2, balloons were connected. This results in a subtle pressure drop in P$_{balloon}$ and a slight increase in displacement, due to the airflow from Balloon$_{in}$ to Balloon$_{out}$. The increase in total balloon volume caused decrease in P$_{balloon}$. In step 3, P$_{chamber}$ starts to increase, resulting in a increase in P$_{balloon}$, as force is exerted on the surface of Balloon$_{in}$. At around t = 30s, P$_{balloon}$ plateaues whilst displacement suddenly increases, this was where snap through occurrs and air flowed from Balloon$_{in}$ to Balloon$_{out}$. At the same time P$_{chamber}$ dipped slightly because volume have reduced

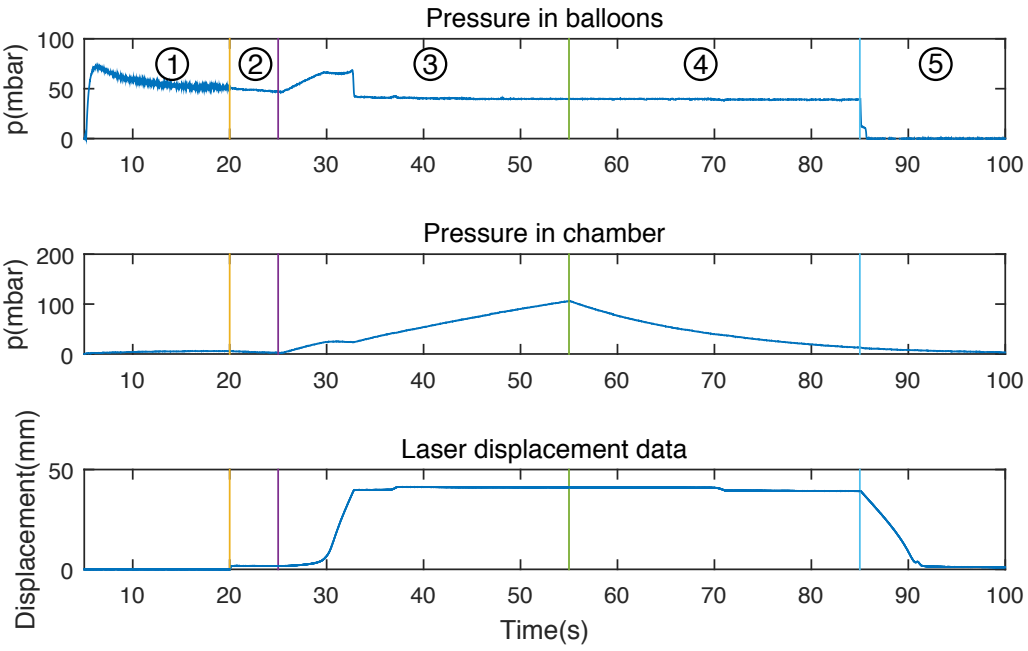

Figure 7.17: Pressure and displacement change during snap through experiment. Circles with numbers show correct step 1-5.

inside the chamber as Balloon$_{in}$ contained less air. After the snap through phenomenon, P$_{chamber}$ continues to increase due to continued pumping and the displacement increases slightly because the increasing pressure acting on Balloon$_{in}$, which further pushes the air left in Balloon$_{in}$ into Balloon$_{out}$. Displacement drops back slightly in step 4, when the chamber was open to air and P$_{chamber}$ gradually drops to atmospheric pressure, the two balloons balanced at a stable state with no external force, as shown in Figure 7.18.

7.3.2.3 Snap through with increasing tube length

In medical applications or robot locomotion, being able to control displacement change at a distance has always been advantageous in many scenarios and could broaden applications. In the previous section we demonstrated the bistability and snap-through effect in two connected balloons. We now investigate the concept further by increasing the connecting tube length, to understand more of the snap through effect in bistable balloon structures.

In this experiment the same process was used as described in Section 7.3.2.1, but the connecting tube length between two balloons was changed from 30cm to approximately 25m. Results are presented in Figure 7.19. As can be seen from the graphs, the responses for the 30cm and 25m tubes were almost the same, with the main differences appears in the snap-through section (3) with P$_{balloon}$ and displacement. With both lengths, P$_{balloon}$ reached 'snap through pressure'

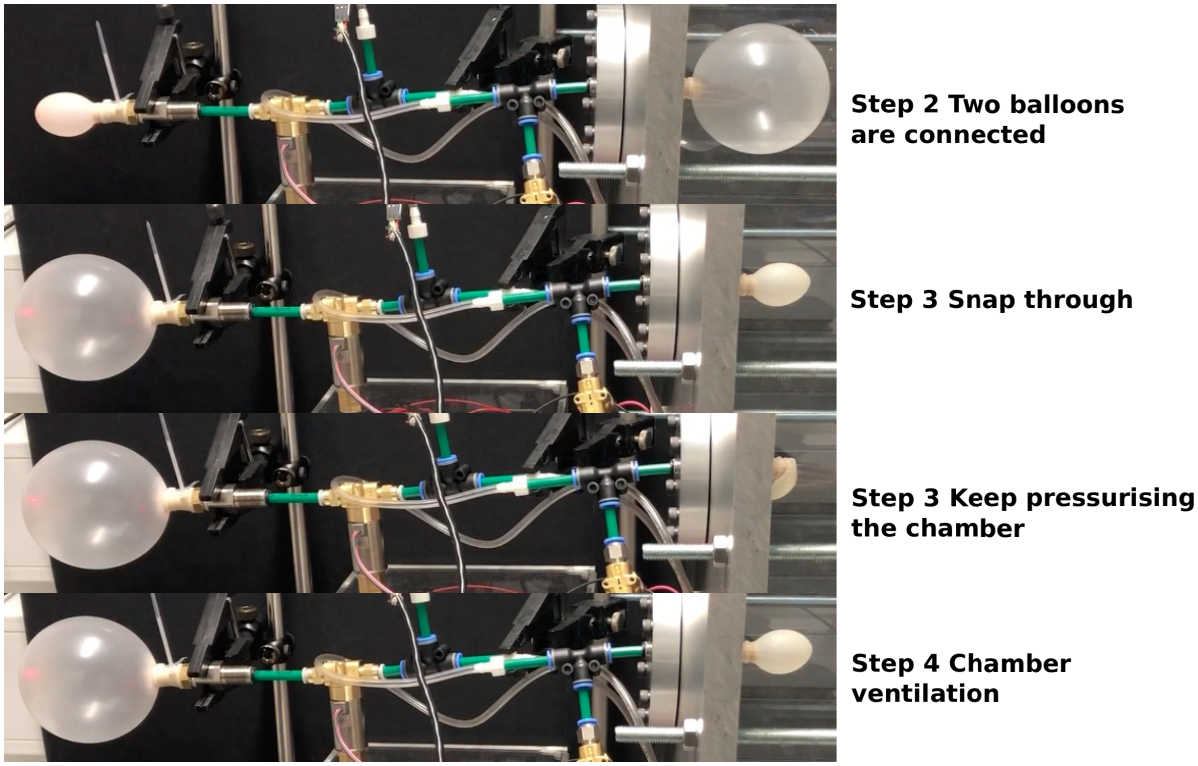

Figure 7.18: A photo showing representative state changes of the two balloons during the experiment.

at similar times, however it took longer for air to flow through in 25m tube from Balloon$_{in}$ to Balloon$_{out}$ and therefore the gradient is less steep as compared to 30cm tube. Snap through and bistability were still exhibited in both cases.

7.3.2.4 Snap through with different initial volume

As observed in Section 7.3.1.2, cyclic stress softening in latex balloon increases with strain applied. In this section we explore the effect of different initial volumes on the snap-through behaviour. Balloon were pre-streched to the 100, 200, 300, 400, 500 and 600ml 15 times respectively to overcome the Mullins effect. We then follow the same procedure described in Section 7.3.2.1, the only change made being at step 1, where Balloon$_{in}$ was inflated to a range volumes.

To observe the difference more clearly, Figure 7.20 only shows the pressure change inside the balloons during step 3 (pumping air into the chamber to induce snap through), step 4 (chamber ventilated) and step 5 (balloons ventilated). As can be seen from the graph, initial stresses were less for higher initial volumes, adhering to the observations in Section 7.3.1.2. As a result, snap-through pressures were also lower at higher volumes and it took longer time to snap through.

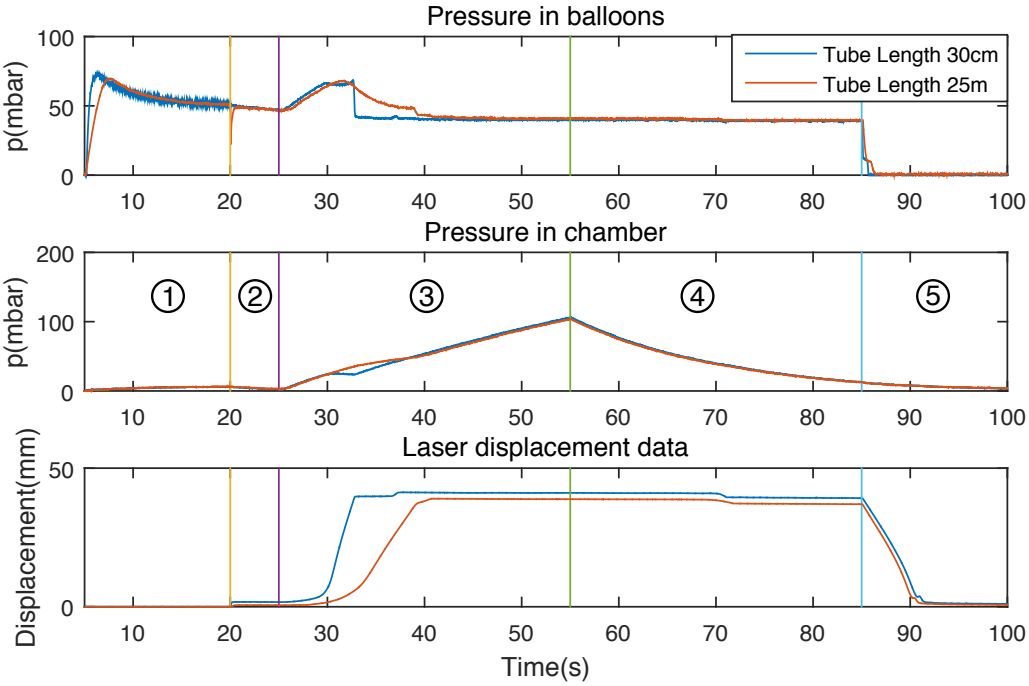

Figure 7.19: Comparison of pressure and displacement change during snap through with different tube lengths. Circles with numbers show correct step 1-5.

7.3.2.5 Discussion

In this section we investigated fundamental bistability and snap-through behaviour in two connected latex balloons, as well as with varied connection tube length and varied initial volume. The initial inflation pressure of the latex balloons was approximately 70 mbar with ϵ = 1.5, and the snapping through pressures were found to be similar to the inflation pressure regardless of tube length. This is because both balloons are identical and have similar inflation curves. The inflation of Balloon$_{out}$ depends on pressure exceeding its inflation pressure, which is similar to that for Balloon$_{in}$. Further investigations could be carried out with balloons in different initial states (e.g balloons with different initial volumes, different sizes), as this could affect the pressure required to snap through between them.

In our set up only one pressurised chamber was used to prove the concept, and tests were only carried out to snap through from Balloon$_{in}$ to Balloon$_{out}$. Another pressure chamber could be built to accommodate Balloon$_{out}$ and the snap-through effect should occur both ways. Also in our tests, Balloon$_{out}$ was in atmospheric pressure at all times, and the additional pressure chamber could simulate cases when Balloon$_{out}$ was placed in pressurised environments.

It is also noted that at snap-through the chamber pressure were at around 21.4 mbar. This finding shows that less force were require to initiate snap-through in the two balloons to produce a higher output pressure (through snap-through inflation of Balloon$_{out}$ to approximately 70mbar)

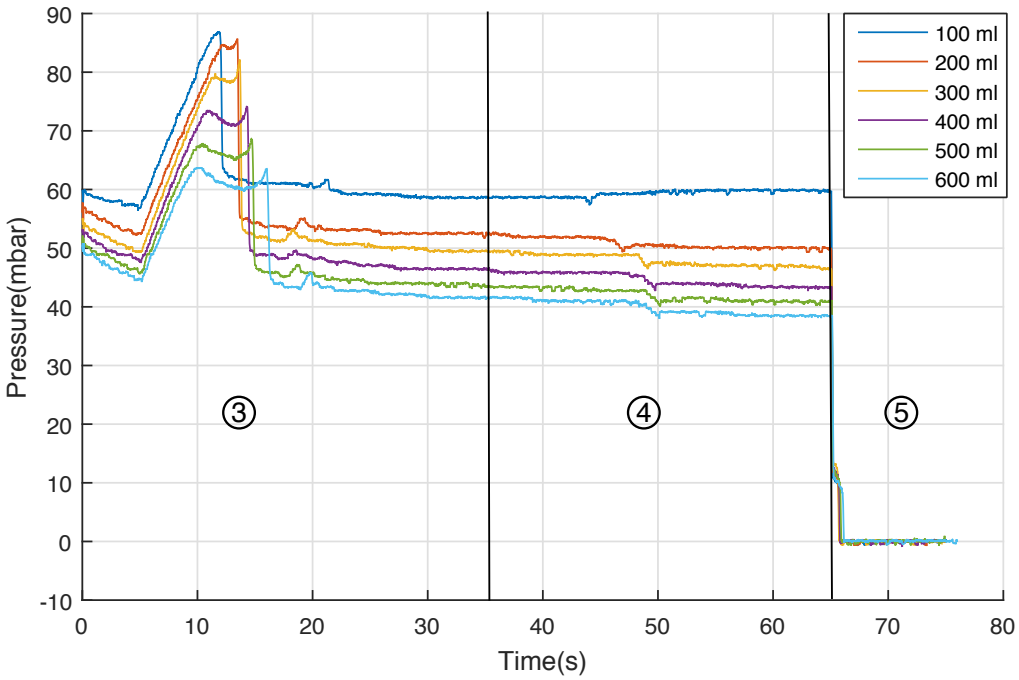

Figure 7.20: Pressure-time curve comparison for balloon pressure $P_{balloon}$ between snap through with different initial volumes. Step 3 - 5 was marked in figure.

as a result. According to literature, the measured interarytenoid pressure was 15-113mbar [194]. The chamber pressure was in this range, which shows that the pressure around vocal folds should be sufficient to snap open an implanted bistable balloon actuator. However the latex balloons used here are too large compare to the size of vocal folds. Therefore a smaller implant design exploiting this bistable snap-through principle should be built and tested in following work.

In the test rig, only one laser sensor was used to measure displacement of the outer balloon. Ideally the displacement of the inner balloon should be measured as well. This was not implemented because the current pressure chamber was made from 10mm pyrex of a clear cylindrical shape and thus causes light distortion. This could be improved in future designs.

7.3.3 Snap through in catheters

In the last section we proved the concept of the snap-through bistable actuation method in latex balloons. In this section we adopted this principle to two connected balloon catheters. Catheters were chosen because they are bio-compatible, and have already been widely used for medical applications.

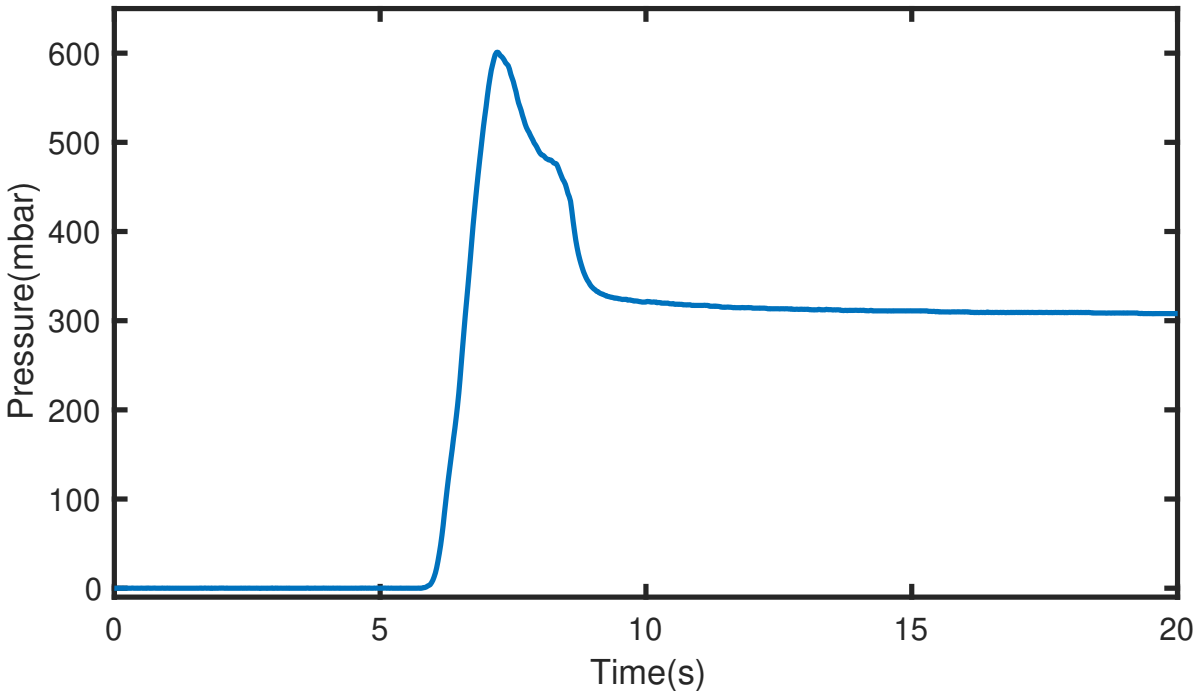

Figure 7.21: Inflation curve of catheter

7.3.3.1 Catheter characteristics

Urinal catheters were used in all experiments. Each catheter was inflated 15 times prior to experiments to remove the influence of the Mullins effect. We first test the inflation curve of a single catheter using a similar experiment set up as described in Section 7.3.1.1, a hand-driven syringe was used instead of the pump, to control inflation volume.

Experiment procedure was as follows: 25ml of air was injected into catheter using a syringe, and then the syringe was pulled out. Air was maintained in the catheter balloon because of the one-way valve design in the catheter. Figure 7.21 shows the inflation curve of a catheter with 25ml of air injection. It can be seen from the graph that the inflation pressure is almost 10 times higher in a catheter (600 mbar) as compared to a latex balloon (70mbar). It then fell and stabilised at 350mbar, the inflation curve follows the general shape of that of a latex balloon.

We then tested the snap through effect in two connected catheters, with the main components illustrate in Figure 7.22) and the 5-step procedure was as follows:

1. Wait 3 seconds for system initiation. Then pump 25ml air into Catheter$_{in}$ while the pressure chamber was opened to air, two catheters were not connected at this stage with solenoid valve in between closed. Duration was set to be 10 seconds.

2. Open the valve between two catheters so that they are connected. Duration was set to be 5 seconds.

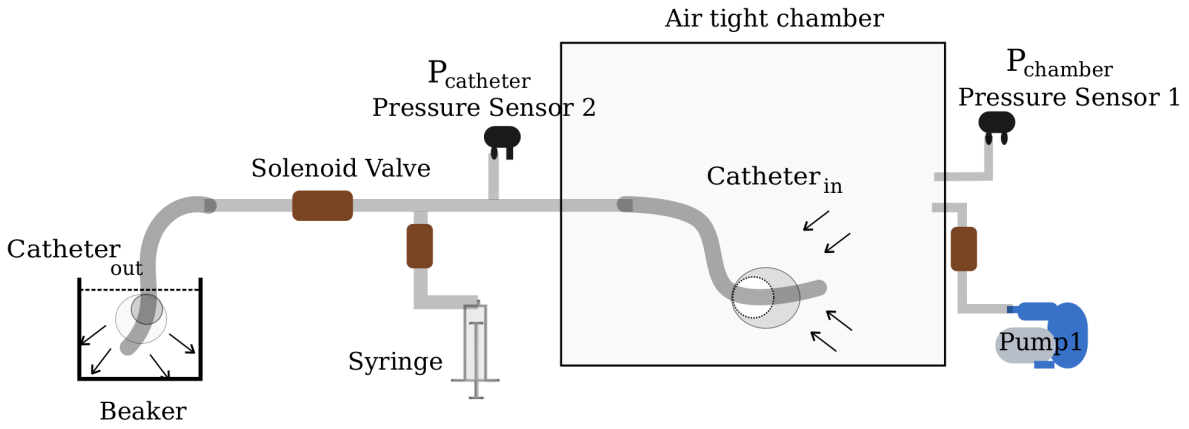

Figure 7.22: Experiment setup for catheter snap through tests.

3. Pump air into the pressure chamber, driving the air inside Catheter$_{in}$ to flow to Catheter$_{out}$. Pumping continues after snap through. Duration was set to be 100 seconds.

4. Open pressure chamber to air so that pressure in chamber gradually falls to atmospheric pressure.

5. Open all connecting valves to air.

The procedure was similar to those described in Section 7.3.2.1, with the main differences being: in step 1, a hand-driven syringe was used as opposed to the pump for precise volume injection; in step 3, time of pumping inside chamber was increased to 100 seconds, because catheters have high inflation pressure and required higher chamber pressure to initiate snap through. In the first experiment, the beaker was empty, Catheter$_{out}$ was placed in atmospheric pressure.

As can be seen from Figure 7.23, the initial inflation pressure of Catheter$_{in}$ was 594.2 mbar and the pressure in catheters increased slightly before dipped to 300 mbar when two catheters were connected. The increase in pressure was different from the snap through in latex balloons, and could be due to the equalisation of pressure from Catheter$_{in}$ to Catheter$_{out}$. Pressure in the catheters increase as air was pumped into the chamber and snap through occurred at an internal catheter pressure P$_{catheter}$ of 462.8 mbar, when chamber pressure P$_{chamber}$ reached 189 mbar. Pressure in catheters dropped slightly from 316 mbar to 300 mbar when chamber was ventilated, but was otherwise stable.

7.3.3.2 Snap through in ballistic jelly

To investigate the snap-through capabilities of this system in muscles, we used ballistic jelly to provide muscle-like surrounding pressure.

Ballistic gelatin is a testing medium that has been scientifically correlated to the density and viscosity of swine muscle tissue, which is in turn comparable to human muscle tissue and is

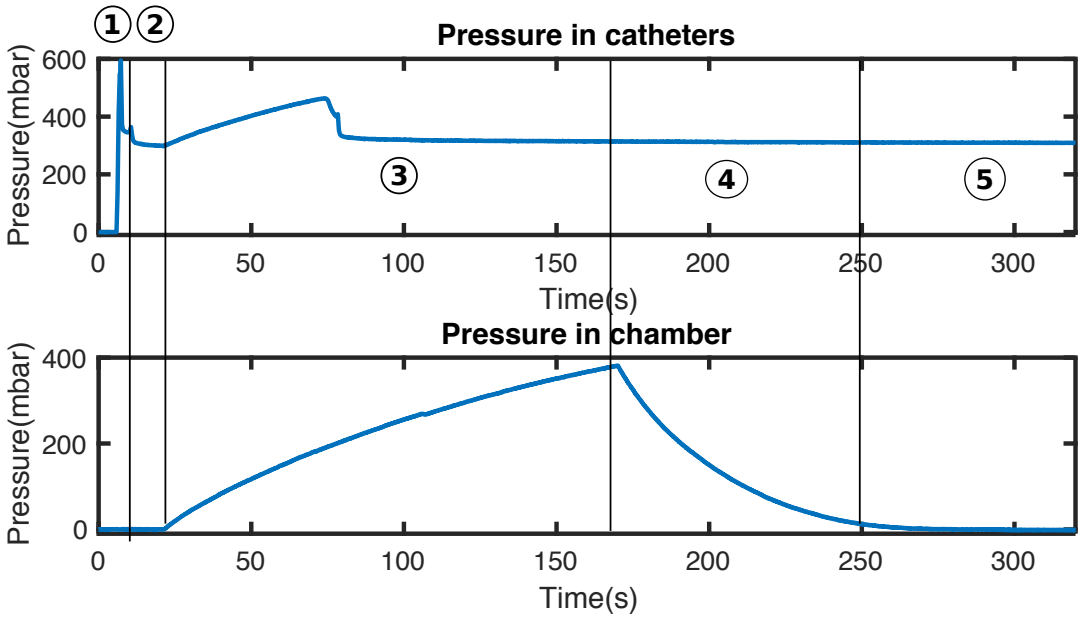

Figure 7.23: Snap through behaviour in two connected catheters. Circles with numbers show correct step 1-5

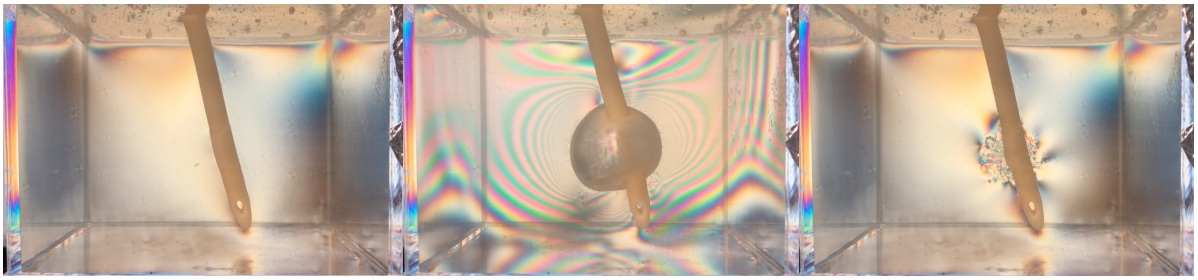

Figure 7.24: Photoelastic experiment showing the inflation and deflation of an catheter in jelly.

widely used to test the effect of wound injuries [195]. For this test we used 300g Bloom (Sigma Aldrich) gelatin and mixed with warm water at a mass ratio of gelatin : water = 1:9. Bloom is a test to measure the strength of a gelatin and the bloom value can be ranged from 30 - 300g Bloom. Higher bloom value indicates higher melting and gelling points and shorter curing time [196]. A 10x10x10 cm clear square pot was used as the container for gelatin mixture. We then placed one catheter into the uncured jelly mixture and cured in a fridge. Photo of a catheter moulded into the jelly is shown in Figure 7.26. Photoelastic experiment was carried out to visualise the stress distribution of the catheter inside the jelly, upon inflation and deflation. Results are shown in Figure 7.24.

The experimental procedure was to Section 7.3.3.1, with the beaker being replaced by ballistic gelatin, and pumping time in Step 3 increased from 100s to 300s to allow sufficient time for snap through. Resultant pressure curves are shown in Figure 7.25. Figure 7.26 shows the catheter

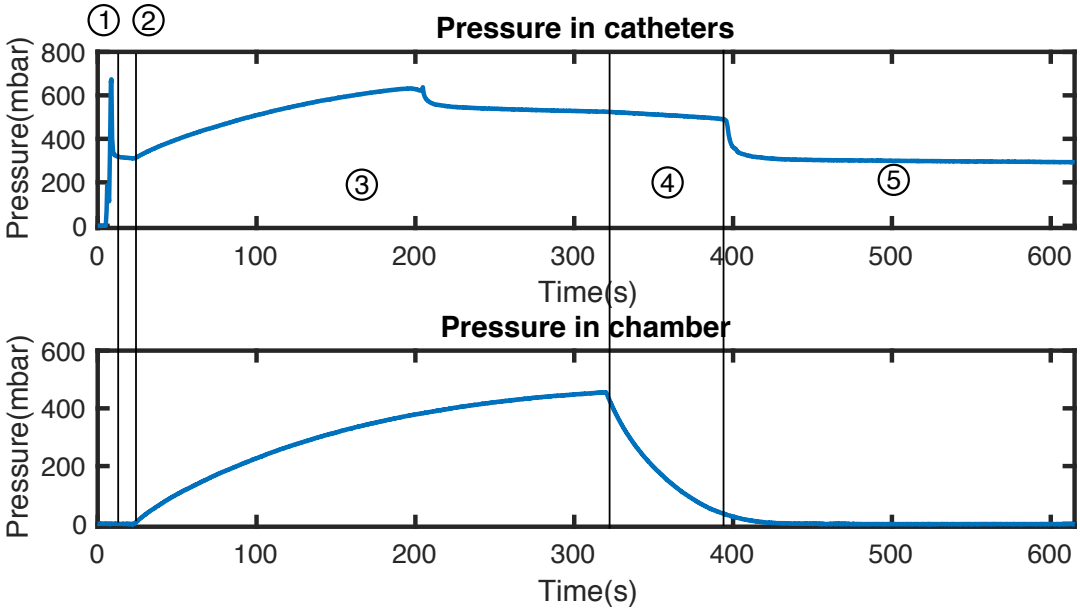

Figure 7.25: Snap through behaviour in two connected catheters with one catheter (Catheter$_{out}$) in ballistic gelatin. Circles with numbers show correct step 1-5.

before and after snap through inside the jelly.

As can be seen from Figure 7.25, the pressure inside the catheters showed a different profile as compared to all the previous experiments. The first peak marks the inflation pressure of Catheter$_{in}$ at 673 mbar. The P$_{catheter}$ then followed similar curves as before, increased as P$_{chamber}$ increased to 382.1 mbar, at which point air flows from through Catheter$_{in}$ to Catheter$_{out}$ and snap through was observed at P$_{catheter}$ = 630mbar. The snap through process took around 150 seconds, which was the longest compared to previous tests. After snap-through, P$_{catheter}$ dipped slightly as the catheters settle into a new bistable state. A further drop in pressure was observed shortly after the chamber was ventilated to 31.16 mbar, at which point P$_{catheter}$ dropped and stablised at 301.5 mbar. This drop could be due to the air being pushed back from Catheter$_{out}$ to Catheter$_{in}$ while P$_{chamber}$ dropped to atmospheric pressure. Pressure exerted by gelatin was not large enough to change the state of the catheters and thus the system remains stable. The stabilising pressure was comparable to that in the first experiment, shown in Figure 7.23.

7.3.3.3 Snap through in chicken breast

Although ballistic gelatin is able to create muscle-like density and viscosity, it lacks the similarities in tissue structures and textures. Therefore in our final experiment, we tested the snap-through in a chicken breast.

A pre-stretched catheter was inserted into the middle of a chicken breast. The experimental procedure was similar to Section 7.3.3.1, with the beaker being replaced by the chicken breast.

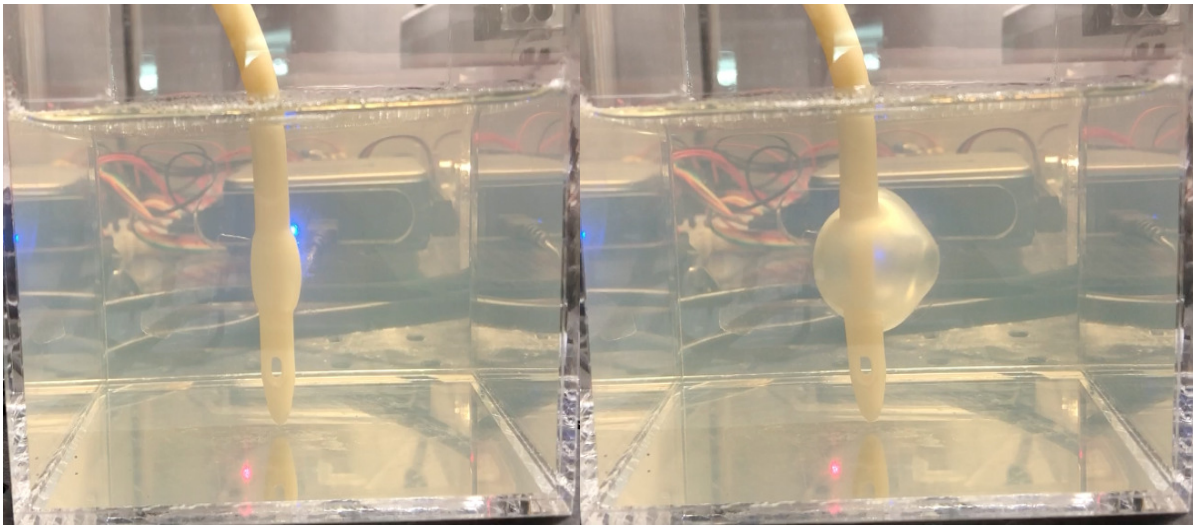

Figure 7.26: Photo of catheter in jelly, before and after snap through.

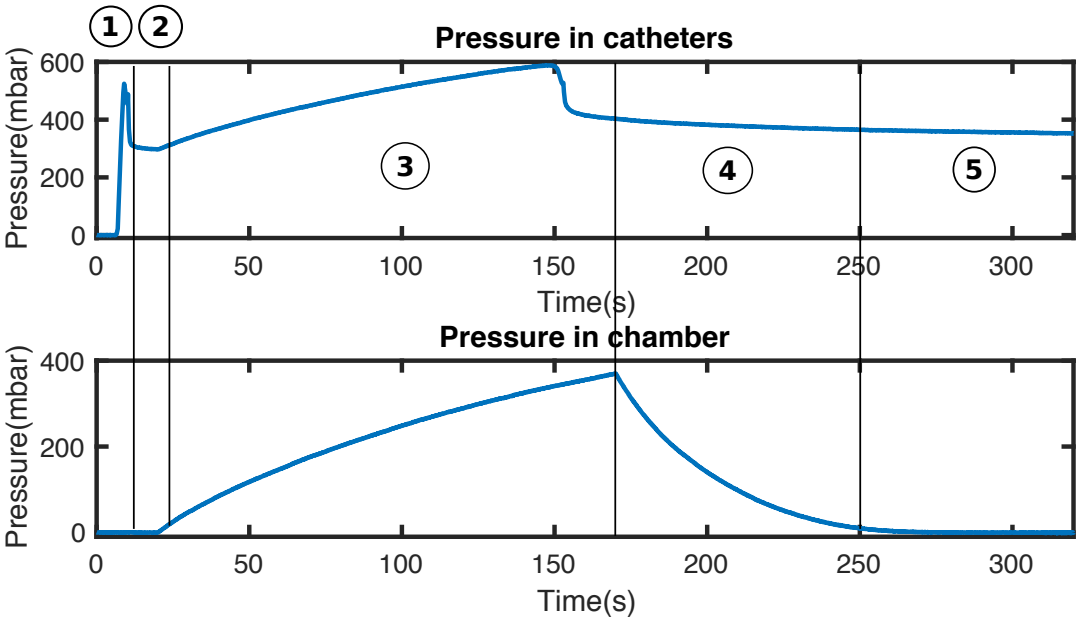

Figure 7.27: Snap through behaviour in two connected catheters with one catheter in chicken breast. Circles with numbers show correct step 1-5.

Resultant pressure curves are shown in Figure 7.27. Figure 7.28 shows the before and after snap-through photo of the chicken breast.

As can be seen from Figure 7.27, pressure inside the catheters followed a similar profile as compared to snap through into water and into atmospheric pressure. The inflation pressure of Catheter$_{in}$ was 524.4 mbar. Snap through was observed when P$_{chamber}$ rose to 342 mbar, at which P$_{catheter}$ was at 587.1 mbar. This was different compare to the previous experiments, as the snapping through pressures were lower than the inflation pressures. The snap through

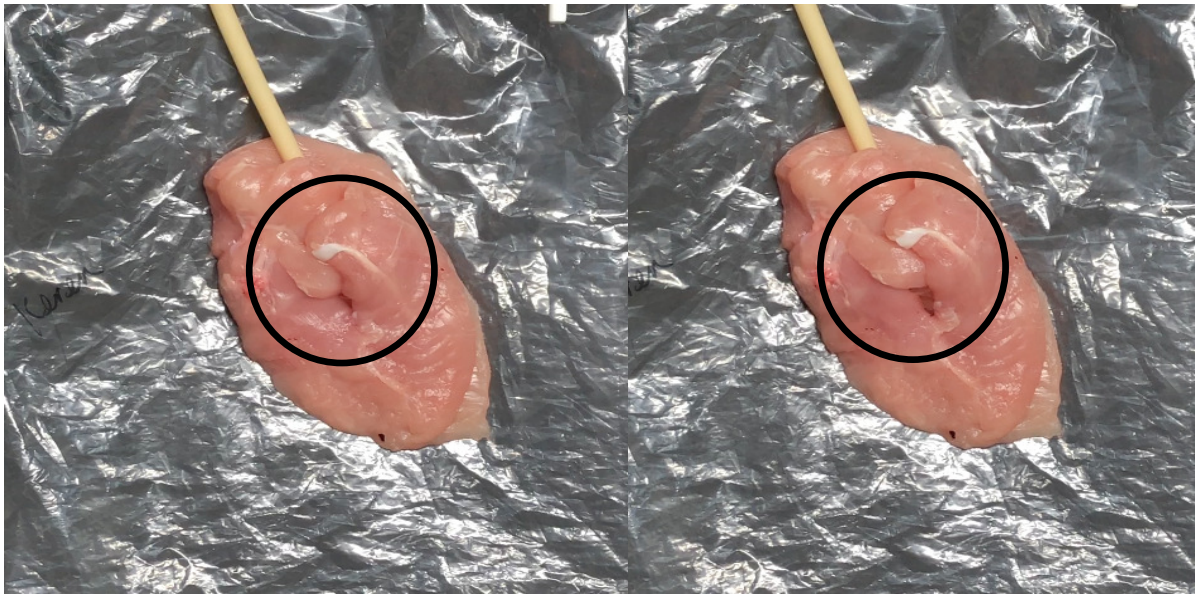

Figure 7.28: Photo of catheter in chicken breast, before and after snap through.

process took around 125 seconds, which was longer than snap through into water and air, but shorter compared to snap-through into gelatin. After snap through, $P_{catheter}$ dipped slightly as the catheters achieved a new bistable state and after chamber ventilation, stablised at 355.6 mbar.

7.3.3.4 Discussion

In this section we conducted experiments with two connected catheters, and explored the effect of different surrounding pressures of $Catheter_{out}$ on the snap-through phenomenon utilising ballistic gelatin and chicken breast.

Ballistic gelatin simulated the muscle in the human body as it is widely used for ballistic tests. Chicken breast simulated not only the muscle strength but also the tissue properties in the surrounding. This was a proof-of-concept test as chicken breast is not comparable to living human muscle tissues. Both tests show promising results as the bistable catheter system remained stable when pressure around $Catheter_{in}$ dropped to atmospheric pressure. This showes that such a system could keep bistability in the human body and thus could be further developed into implants in different body parts. The snap through process, however, took 150 seconds, which was not ideal for fast actions. This could be the limitation of the pump used in the system. This can be improved by replacing the current pump with a more powerful pump or an air compressor, which could pressurise the chamber in a shorter time and therefore speed up the snap through process.

7.4 Conclusion

In this chapter we explored bistability and the snap through behaviour in latex balloons, catheters and elastomer membranes.

Condom material was chosen to implement the dome actuator after preliminary tests showed its ability of fast loading and unloading. This feature is advantageous in developing implant for vocal fold paralysis as well as developing binary robots that requires fast actuation. However, features observed in materials such as VHB show a high inflation pressure and a relatively low stabilising pressure, which meant that these materials could be more stable during state transformation and thus they could be used in cases where stability is more important than fast snap-through.

In the dome actuator developed, an external force is required to induce snap through behaviour. This design could be made more compact by exploring different actuation methods. A possible future development would be using SMA as a driving force.

Tests with two connected latex balloons showed that snap through could happen with less driving pressure compare to internal pressures inside balloons, and that it could happen with extended tube length and increased initial balloon volume. The snap-through time increased with tube length. Possible applications from the long tube tests could be enabling binary control of an actuator from a distance.

Tests with two connected catheters follows similar set ups as with balloons. Catheters had thicker materials and can tolerate higher pressure, but also require higher driving pressures to enable snap through. Experiments with catheters successfully showed snap-through into ballistic gelatin and chicken breast. These broadens the application of this concept not only to design a implant for vocal folds paralysis, but also for other body parts where higher output force is required.

Tests with spherical membranes lead to preliminary tests of a condom dome actuator, where point force was used to demonstrate snap-through phenomenon. This actuator had low inflation pressure compared to other materials and balloon shapes, and can perform state change in under 1.5 seconds. It shows the ability of exploiting fast manoeuvre/size change using the principle of snap-through in soft materials.

A photo of a preminilary test is shown in Figure 7.29. In this set up an SMA coil was wrapped around the surface of membrane (contained in an insulating sleeve). The SMA could also be embedded inside the dome of the actuator to allow complete softness of the structure. In preliminary tests, the actuator snapped through when current was passed through the SMA and it contracted.

In conclusion, bistability and snap-through behaviour exhibited in inflated hyperelastic materials can have broad applications in medical applications, building binary robots utilising state changes caused by two or multiple balloons/spherical membranes.Different output forces and different driving forces could be selected by choosing different elastomer, or different 3D

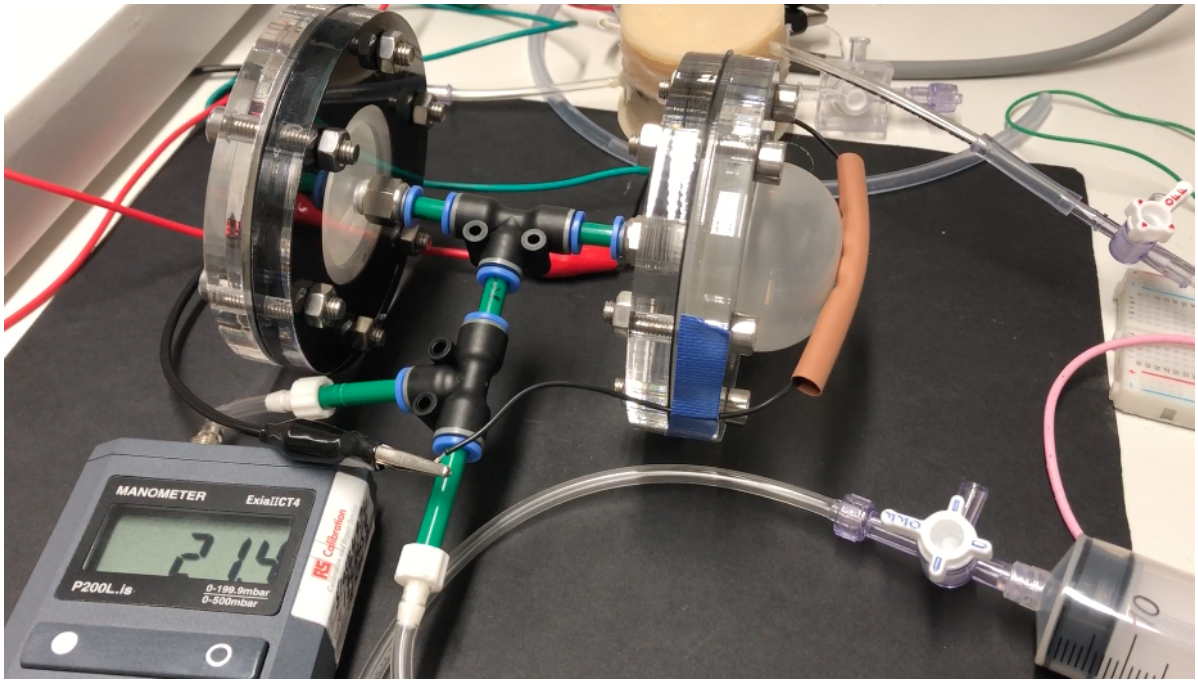

Figure 7.29: Snap through with SMA wrapped around the surface membrane.

structures. In future work, more physical experiments and computational are needed to fully understand this exciting and high-potential phenomenon.

CHAPTER 8

CONCLUSION

This thesis investigates laryngeal disorders, with an emphasis on vocal fold paralysis, and aims to propose an alternative solution to the current implants used in medialisation thyroplasty surgery. We have achieved the aims proposed at the beginning of this thesis and by make the following contributions to the field:

1. Developed a novel assistive coughing device, CoughAid, to mimic the function of the glottis. Preliminary results from a small cohort of post-laryngectomy patients show positive impact on coughing effciency using CoughAid.

2. Built a computer-controlled respiratory simulator to simulate human breathing and coughing, which can accurately produce comparable peak flow rate and volume.

3. Built a motor-controlled model to simulate the movement of arytenoid cartilage, and a soft valve that mimics the opening and closing of vocal folds.

4. Designed and fabricated a bellows actuator which provides effective closure in a pig larynx. Investigations into a novel bistable balloon actuation method were experimentally characterised in pressurised chambers and demonstrated controllable and stable shape changing abilities.

8.1 Summary of results

Although vocal fold paralysis is a well-studied clinical disorder and continual efforts are being taken to improve surgical procedures, there has been little focus on enhancing the treatments with soft robotics. This is despite the biocompatibility and mobility provided by soft robotic implants, which could provide new dynamic solutions to this condition.

Therefore in this thesis, we aimed to carry out preliminary tests to show the feasibility of integrating soft robotics into current treatments, as well as building prototypes to prove the principle by testing such an actuator in a pig larynx.

Prior to device development, given that coughing can be problematic in patients suffering voice disorders, we investigated the importance of strong glottal closure in cough efficiency, and designed and tested an assistive coughing device, CoughAid (Chapter 3). Experimental studies with patients with laryngecotomies and a control group have shown improvement in coughing parameters using CoughAid in both groups. This device could be made more portable and serve rehabilitation purposes for post-larygectomy people. It is important to understand the mechanism behind the motion of the larynx. We used the same solenoid valve that mimics the glottis function in CoughAid and set the foundations for investigating the human respiratory system by building a computer-controlled simulator that can correctly simulate the peak flow rate and volume in breathing and coughing (Chapter 4). This focused on mimicking breathing and coughing, because these are the primary problems faced by vocal paralysis patients. This study led to the development of the respiratory simulator, which can not only reproduce the key parameters, but is also able to mimick the full profile of breathing and coughing.

Following investigations of the respiratory system, we then analused the movement of the vocal folds (Appendix B). The arytenoid cartilage is central to the motions of the vocal folds. However, the precise relationship between the arytenoid cartilage movement and vocal fold positions has yet to be fully understood. We therefore designed and built a mechanical simulator of the arytenoid cartilage, based on pinier theory, which successfully performed rocking, sliding and rotation manoeuvres described in computational models. This model only focuses on re-creating movements of the arytenoid cartilage without considering interactions with muscle or other cartilages. The simulator provides a visual aid for understanding the movement of the arytenoid cartilages and could be further developed into a teaching platform.

We then examine the structures of the vocal folds (Chapter 5). Material properties and composition of vocal fold layers have been studies extensively, however existing artificial vocal folds are mostly static or move passively during phonation tests. We took inspiration from the shape of glottis opening and build a novel artificial vocal fold structure that functions as a soft vocal fold-like valve when pneumatically actuated.

With more understanding of the physiological system related to vocal folds, we then moved onto the development of soft implantable devices. The main vocal fold functions desired for patients with vocal fold paralysis are phonation, breathing and coughing. We identify that better airway management and improved voice quality could be achieved by improving vocal fold mobility in the lateral axis. A soft robotic implant we proposed that could provide mobility in lateral directions, such that the function of paralysed vocal cords could be restored in terms of abduction and abduction.

A bellows shaped elastomer actuator was designed and moulded, which could expand to a

triangular shape under pneumatic actuation (Chapter 6). Tests of the bellow actuator in a pig larynx have shown effective closure of vocal folds under low pressure and low volume injection. The limitation of this design is that the actuator needs to be driven by compressed fluid and implanting such a power source is challenging in the human body. To address this issue, we investigated semi-active actuators by exploring the bistability and snap-though instabilities in hyperelastic materials (Chapter 7). Connected flat membranes and connected latex balloons were used to test the characteristics of the snap-through phenomenon in inflated elastomers. Results show that bistability exhibits regardless of the connecting tube length or initial volume inside balloons. The principle was subsequently tested on two connected urethral catheters, with one catheter embedded in muscle-like gelatine and chicken breast, and results show that controllable bistability persists. These preliminary results highlight the robustness and repeatability of bistable and snap through behaviours in biocompatitable materials, and offer a new way of actuating medical implants that switch between two states.

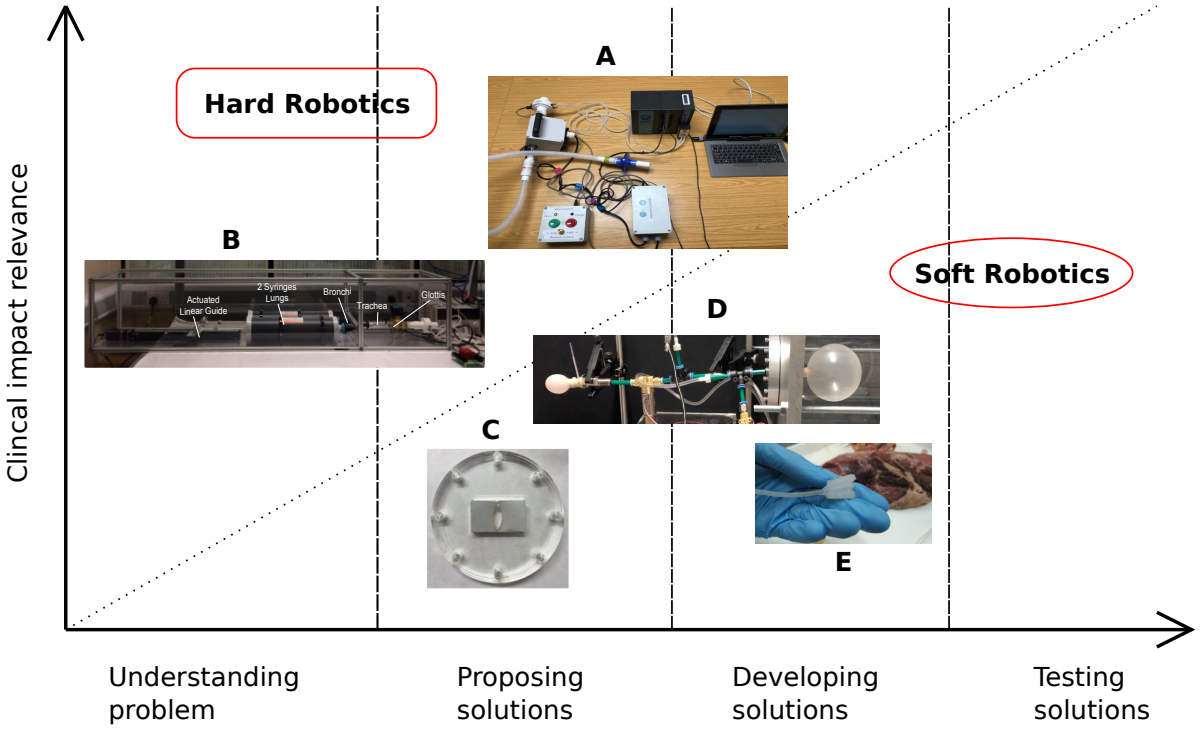

Figure 8.1: Simulators and devices developed in this thesis with regard to clinical relevance. A: CoughAid, B: Respiratory simulator, C: Artifical vocal folds, D:Bellows actuator, E: Bistable balloons actuator.

Figure 8.1 shows the simulators and devices that have been built during this research, and their clinical impact relevance and stages of development. Most devices arising from this thesis are at the preliminary stages of development, but they have bridged the gap between the vocal fold paralysis problem and a feasible soft robot solution. They point to further simulator development

towards medical teaching platforms, and the development of self-driven, biocompatible and durable actuators for vocal fold paralysis.

8.2 Rigid robots vs Soft Robots

Rigid robots are made of rigid materials with fixed mechanical properties wheres soft robots are made from soft or smart materials such as soft polymers, shape memory alloys and shape memory polyners. These structural and material differences generates advantages and disadvantages in both systems.

In rigid robotics, their stiff structure is highly suited for treatments requiring strong mechanical reinforcement. They have advantages including precision positioning and motion control using advanced control strategies and sensors, and are able to exert high forces. However rigid robotics have drawbacks especially when in direct contact with soft tissue. For example, stiff endoscopic arms could cause pain when navigating in the human body, and because of their inflexibility, they are unable to access all internal targets.

Soft robots, on the other hand, have soft and flexible structures which possess greater uncertainty in precision control, but which also are inherently self adaptive and tolerant to the varibility and confined spaces of the human body. Soft robots can have high impact resistance because their materials can absorb dynamic shocks. Soft robots can also be manufactured at low cost and from easily accessible materials. However, the modelling of soft structures can be challenging, especially for human-robot interaction and inside the complex human body. Finally, soft robots can be powered by flexible power systems and controlked by stretchable electronics and sensors.

Both hard and soft robotics have their applications in the field of medical robotics, and have advanced rapidly through past decades. Some tasks such as surgical robots (e.g the Da Vinci surgical system) require a high level of precision control and rigid robots are better suited to such tasks. In contrast, in areas such as stents and implants, soft materials are more commonly used due to their material and mechanical bio-compatibility. In other areas, such as surgical tools for minimal invasive surgeries or rehabilitation exoskeletons, where high performance in control and force are needed but soft materials are also most attractive, more and more research are looking into combining hard and soft elements.

In this thesis we have explored the characteristics of both hard and soft robotics systems. Future studies are likely to include combining soft robotics with traditional rigid robotics, where the respective advantages of both can widen the research scope and increase applications.

8.3 Future Research

In this research we explored a new potential solution to laryngeal disorders, and investigated simulators and prototype devices using both conventional rigid robotics and soft robotics, explor-

ing their advantages in different aspects of control and mechanics. Building on this fundamental piece of work there are a number of future works that can be investigated:

Firstly, all simulators built were made from rigid materials. Further development could integrate soft materials into the simulators to mimics soft tissue properties. For example, in Chapter 4: respiratory simulator, it is possible to replace the current solenoid valve with the soft valve developed in Chapter 5 after completing further characterisation and reliability tests. Some lung simulators use bellows, artificial lungs or cadaveric lungs, to mimic the complicated aeroelastic behaviour of human lungs. However, there has been little study into the structure of upper respiratory system, such as the trachea and vocal folds, despite their vital role in the breathing.

In addition to adding soft parts in simulators, with the bellows actuator developed in Chapter 6, there is the potential of adding soft sensing into the system. The development of soft sensors is a growing field with diverse potential solutions. Combining the developing fields of artificial organs and soft sensing with well-developed mechanical control and modelling could result in more robust simulators.

Last but not least, more investigation can be carried out to further understand the bistable balloon concept and building medical implant devices upon it. The system proposed in Chapter 7 utilises a simple two-balloon structure, which are inspired by the wide use of balloon catheters in the human body. Currently the main challenges for implantable devices revolve around power and control inside human body, and consequently many researchers have looked into micro pumps to overcome these challenges. Here we approach these challenges from a different perspetive by developing a bistable system utilising internal pressures exerted by muscle movement in human bodies. With further reliability testing and more investigation into manufacturing processes, a new generation of energy efficient implantable soft medical devices could be realised.

APPENDIX A

APPENDIX A: RESPIRATORY SIMULATOR 1.0

The respiratory simulator 1.0 was designed and built in order to understand the mechanics of the muscular fluidic systems and to provide a test rig for device development.
This simulator has a larger scale in the larynx area as compared to the actual human respiratory system physiology for better visualisation and modification. Consideration of dimensionless numbers in fluid mechanics such as the Reynolds number can ensure that dynamic similarity is maintained (discussed later in section A.3). The respirator can readily be modified to have true to size dimensions and similar properties of the human larynx.

A.1 System Design

Figure A.1 shows the design of the computer controlled respiratory simulator 1.0. As can be seen from the figure, the respirator has a 450mm computer-controlled Zaber linear actuator (X-LSQ450B-E01) to model the movement of diaphragm, two 3L pneumatic syringes (KoKo KRS007) configured in parallel to give 6L total lung capacity, a 3D-printed rigid connector designed on the shape of trachea, and a vertical placed clear acrylic tube with clamps in the middle to accommodate future larynx device development. Figure A.1 also presents a top down schematic diagram showing dimensions of the components, where d1 = 100mm , d2 = 35mm, d3 = 60mm, d4 = 100mm.

The Zaber linear slide has a maximum speed of 280mm/s and is able to hold 75N, which is more than sufficient to simulate breath. In this configuration the actuator and syringes can generate flows up to 112L/min, providing the full range of human-like respiratory flow rates. The pneumatic syringes model lung volumes. The two syringes have a total capacity of 6L, exceeding the average vital capacity of men(4.6L) and of woman(3.1L). The 3D printed rigid connector is designed to fit the human bronchi tract shape as can be seen in Figure A.2 (left). The trachea is

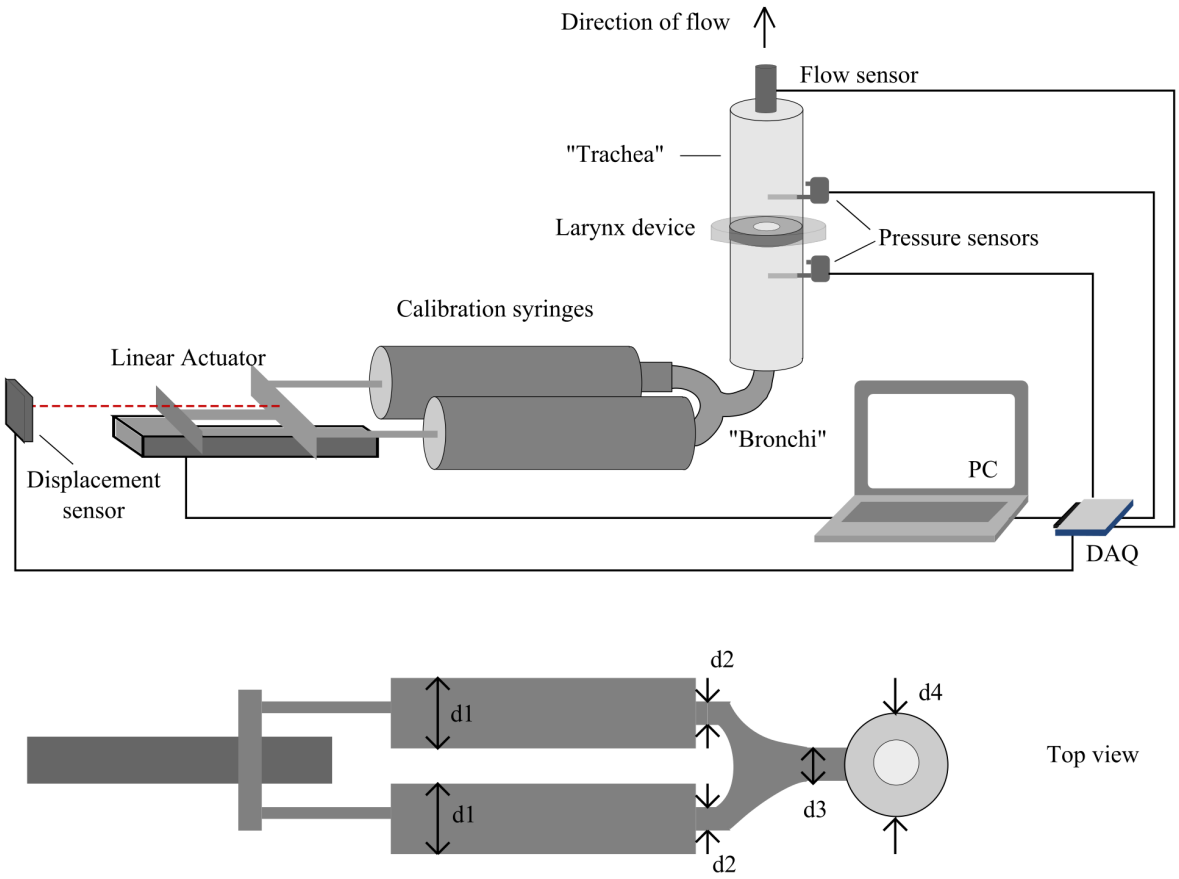

Figure A.1: Respiratory Simulator 1.0.

Technical specification		**Respiration capabilities**	
Total volume	6L	Vital capacity	0 - 6 L
Actuator force	0 - 80 N	Max. flow rate	112 L/min
Actuator speed	0 - 280 mm/s	Rate at 4.8L VC	23 breaths/min
Accuracy	45 μm		

Table A.1: Technical specification and respiration capabilities of the rig

modelled using two 20cm long clear acrylic tubes, bolted together using flanges. It is designed in this way so that the larynx device (example shown in Figure A.2 (right), the device will be introduced in Chapter 6) can be inserted into the ‘trachea‘ very easily as well as can be easily replaced at different design stages.

Table A.1 summarises the technical specification and the respiration capabilities of the respiration test rig.

To enable the respirator to be characterised and validated against human respiration data, we

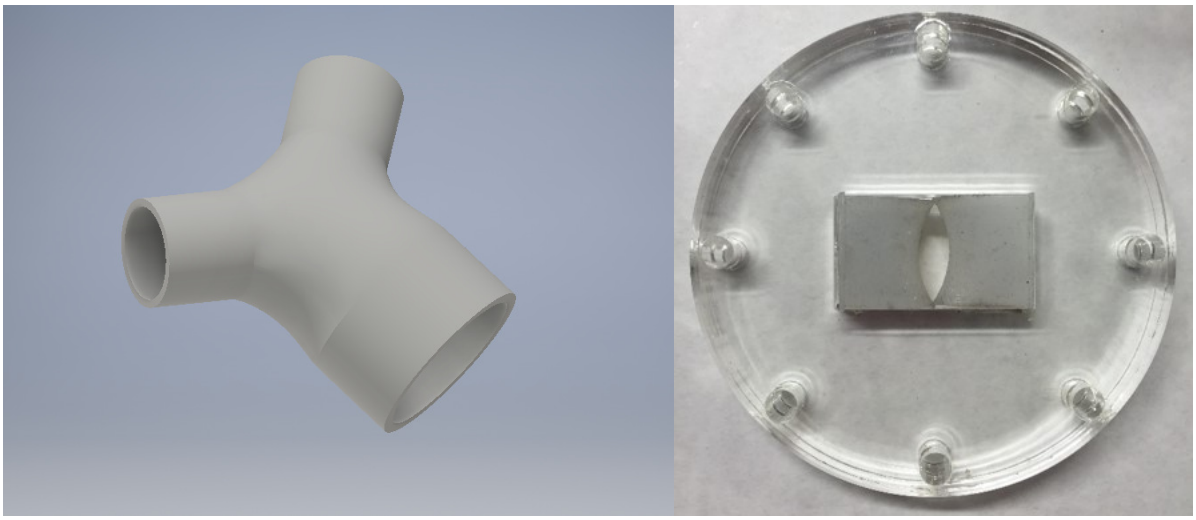

Figure A.2: Tract and larynx device design. Left: CAD image of the connector design. Right: The larynx device.

attached two pressure sensors (Honeywell, SSCSNBN015PDAA5) and one flow sensor(Honeywell, AWM720P1) to the 'trachea' tube. A SHARP optical displacement sensor (GP2Y0A21YK0F) is also used to monitor the displacement of the syringe plunges during respiration simulation. Although the linear slide provides controllable distance travel through its stepper motor drive, it is better to validate these readings with an external distance sensor in case of motor slip. The differential pressure sensors have a range of ± 15 psi and the flow sensor has a range of 0-200 L/min. Sensor locations were as illustrated in Figure A.1, and sensor data were acquired using DAQ (National Instruments).

To obtain the pressure readings as accurate as possible, it is best to put the pressure sensor at the centre of the tube, however this would cause too much flow disturbance. Therefore we mounted the pressure sensors on the tube wall and measured the pressure from the centre of the flow using a 5mm diameter tube. We measured pressure with varied tube length (varying Lp as shown in Figure A.3) to investigate the effect of tube length on pressure drop along the tube. Results show a pressure drop of around 0.2% when tube length was varied from Lp = 2cm to Lp = 7cm tube and can be neglected.

A.2 Results

Figure A.4 shows the resulting flow output from driving the linear slide forward and backward. The output registers a symmetrical flow pattern as 'breath in' (slide driving backward) and 'breath out' (slide driving forward).

Figure A.5 shows the synchronised sensor data. Savitzky–Golay filter was applied to data because it smoothed data without distorting the general trend. As can be seen from the graph, the

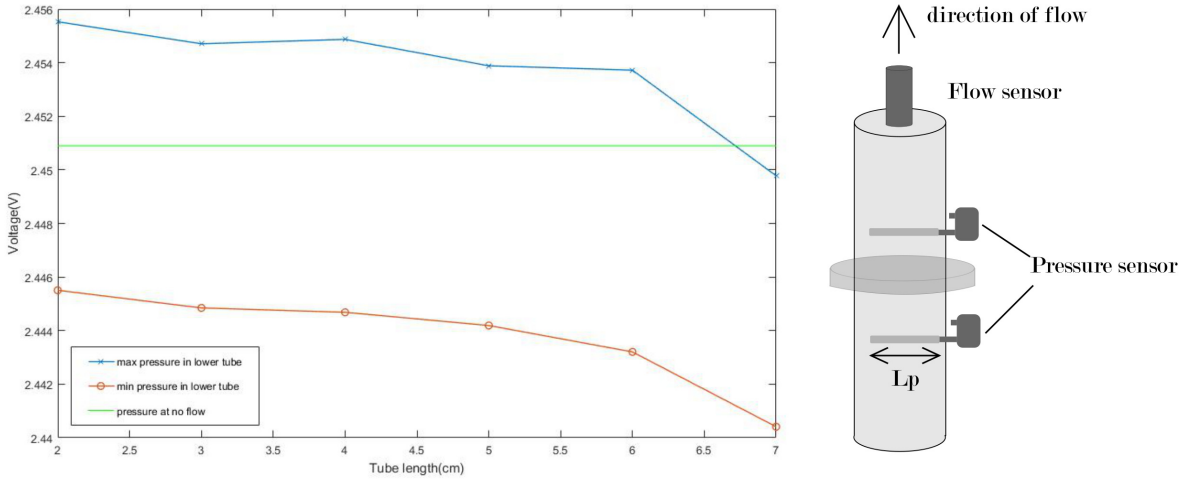

Figure A.3: Schematic diagram of pressure test

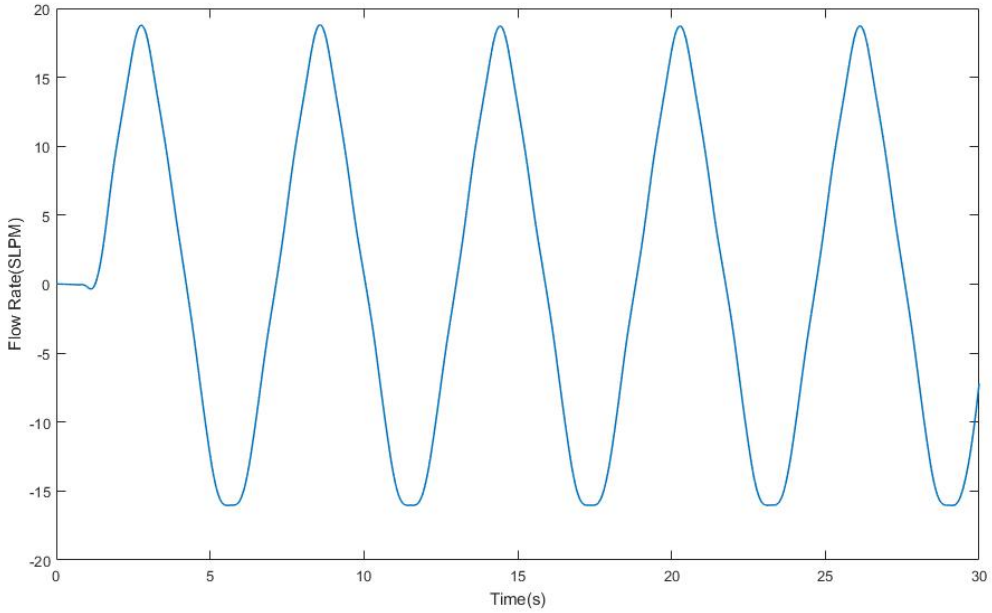

Figure A.4: Simulated symmetrical breathing flow rate.

flow rate is not symmetrical and this is because inhale and exhale flow pattern are not in perfectly symmetrical in human breathing (shown in the left of Figure 4.4), the control programme was made to adapt to the real flow characteristics.

Figure A.6 show how relative flow constriction is related to occlusion type. The presence of six 'occlusion' discs with aperture diameter D (shown in Figure A.2(Right)) of 10, 20, 30, 40, 60, 80 mm were investigated under different simulated respiration rates stated in Table 4.2. It

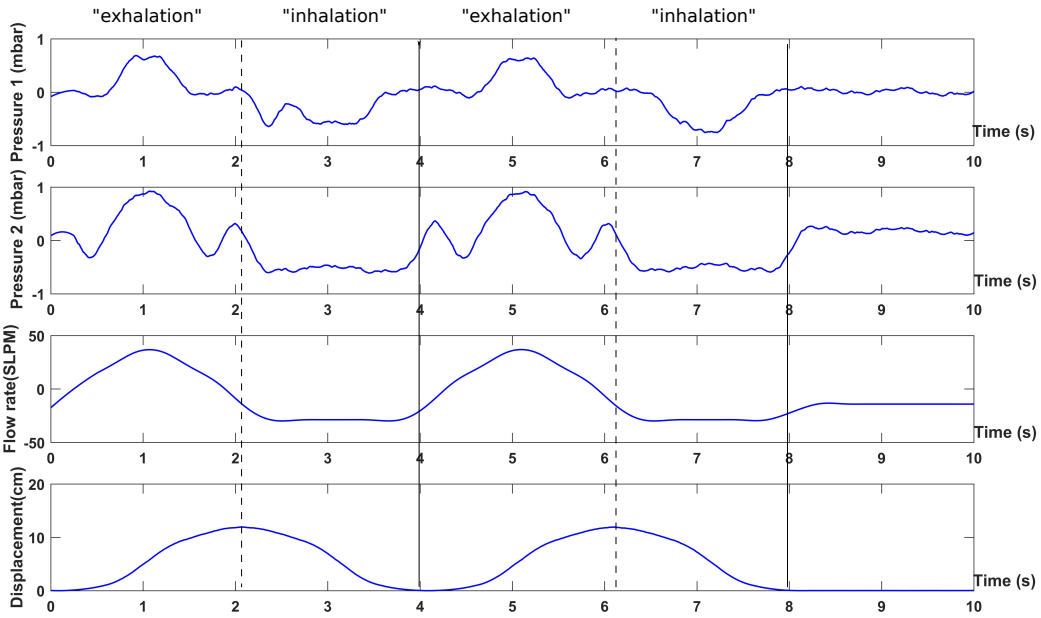

Figure A.5: The synchronised pressure, flow and displacement data. Solid lines mark the end of each respiration cycle and dotted lines separate “inhalation“ to “exhalation“.

can be seen clearly that the pressure in the upper airway does not change too much with small obstructions in the flow. However, it starts to increase rapidly as the diameter decreased to 20 mm and as the flow rate increased to 40 L/min, which indicates that children would experience more breathing difficulties compare to adults if similar types of tracheal occlusions were to occur inside the airway.

A.3 Discussion

As can be seen from Figure A.5, the upper (Pressure 1) and lower (Pressure 2) pressure data both show fluctuations at the beginning and at the end of each “exhalation“ phase. This could be due to the large Reynolds number caused by large tube diameter.

$$Re = \frac{QD}{vA} = \frac{0.0003 \times 0.1}{1.460 \times 10^{-5} \times \pi(0.05)^2} = 261.6, \tag{A.1}$$

where Re is Reynolds number, Q is the volumetric flow rate (m^3/s); D is the hydraulic diameter of the pipe; A is the pipe's cross-sectional area (m^2); v is the kinematic viscosity of the fluid (m^2/s). The calculated Re in the airflow in this system is 130.8, where $Q = 18L/min = 0.0003m^3/s$, $D =$

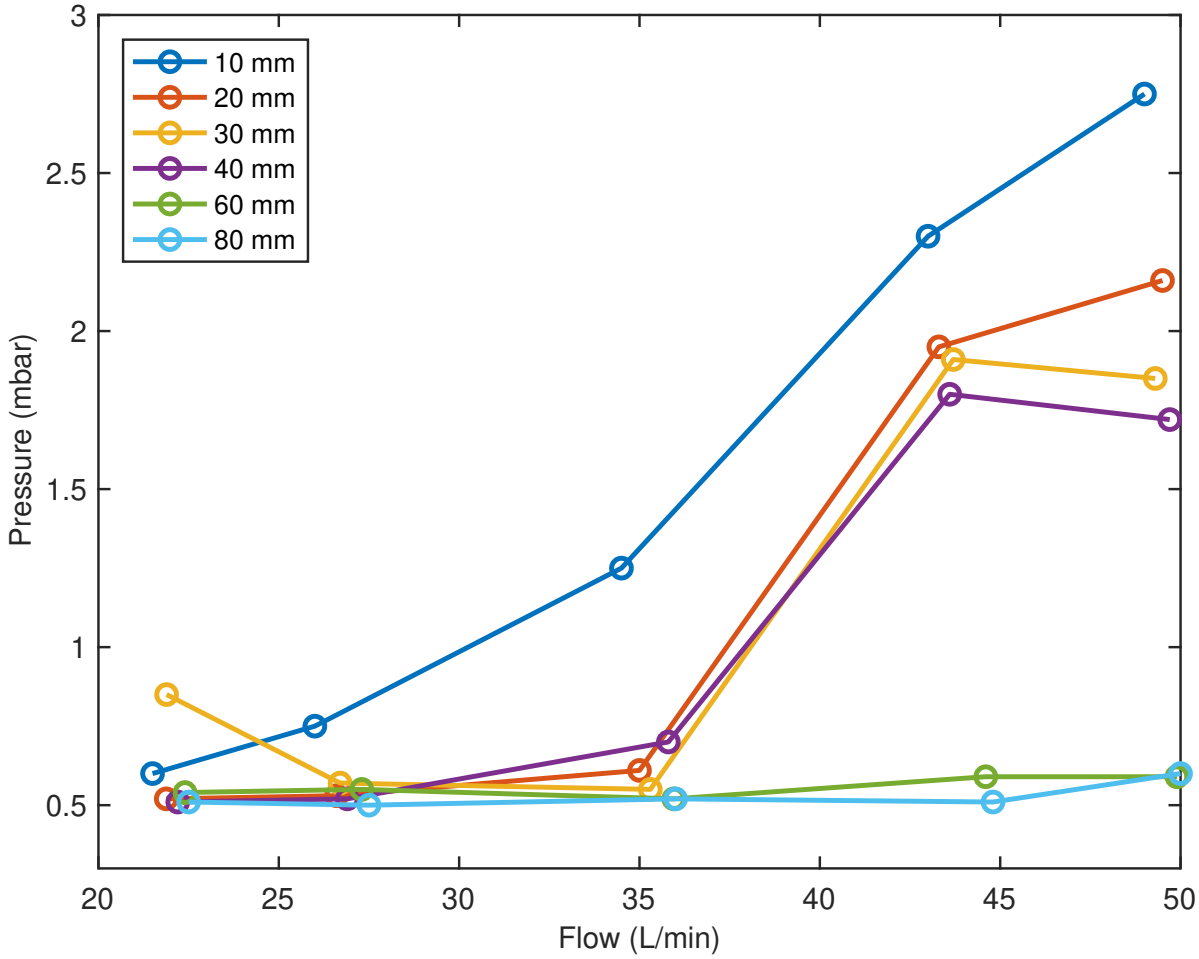

Figure A.6: Pressure and flow change in upper airway with varied occlusions.

$0.1m$, theoretical value of the dynamic viscosity of air at sea level,$v = 1.460 \times 10^{-5}$ was used [197]. This is significantly lower than the estimated Re in human trachea, which is 1160 [198].

Reynolds number increases as tube diameter decreases, and therefore causes a greater pressure loss along the tube. This was also the primary reason of choosing a larger than human sized trachea tube in the system - to reduce pressure loss due to flow turbulence in a small tube.

However, with the existing “trachea“ size, the pressure change detected is very small through this flow rate. Since the normal breath rate for adults is 12 - 18 breaths per minute, and tidal volume is about 0.5L, assuming flow rate is constant, the average expiration flow rate would be 12 - 18 L/min, a pressure sensor with smaller measurement range and higher accuracy may be needed for future tests; or the ‘trachea‘ dimension needs to be modified.

To conclude, results have shown that flow and aperture size has an inverse correlation so that as aperture size reduces, flow rate increases. This proves the capability of the system for

simulating breathing, however, the peak flow rate it has produced is lower than the peak cough rate stated in literature. This is due to the limitation of the flow sensor used in this study, as the maximum flow rate it can detect is up to 200 L/min. In addition the current upward “trachea“ is too wide for the simulation of coughing.

APPENDIX B

APPENDIX B: THE MECHANICAL MODEL OF THE ARYTENOID CARTILAGES

In main thesis, we explored the human respiration system and developed a respiratory simulator to simulate key characteristics such as peak flow rate and peak pressure. In this appendix chapter we look into the larynx area, to better understand the movement of vocal folds during phonation, swallowing and coughing.

This chapter is a collaborative work with Krishna Manaswi Digumarti and Alice Hayes. I led the mechanical design and wrote the main control programme for the mechanical model; KM.D and I assembled the final mechanical model and carried out tests together; A.H, KM.D and I analysed the results and discussed the design together.

Main contributions

- Designed and built a mechanical simulator to replicate three degree of freedom movement of the arytenoid cartilage.

B.1 Introduction

In this section we focus on the cartilages that are involved in articulating movement of the vocal folds and their mechanical motions while doing so. We will then review computational and mechanical modelling approaches that have been made to model the movement of vocal folds, before presenting a new model.

As introduced in Chapter 2, the larynx accommodates a total of 6 cartilages, with 3 unpaired cartilages: epiglottis, thyroid cartilage, cricoid cartilage; and 3 paired cartilages: arytenoid

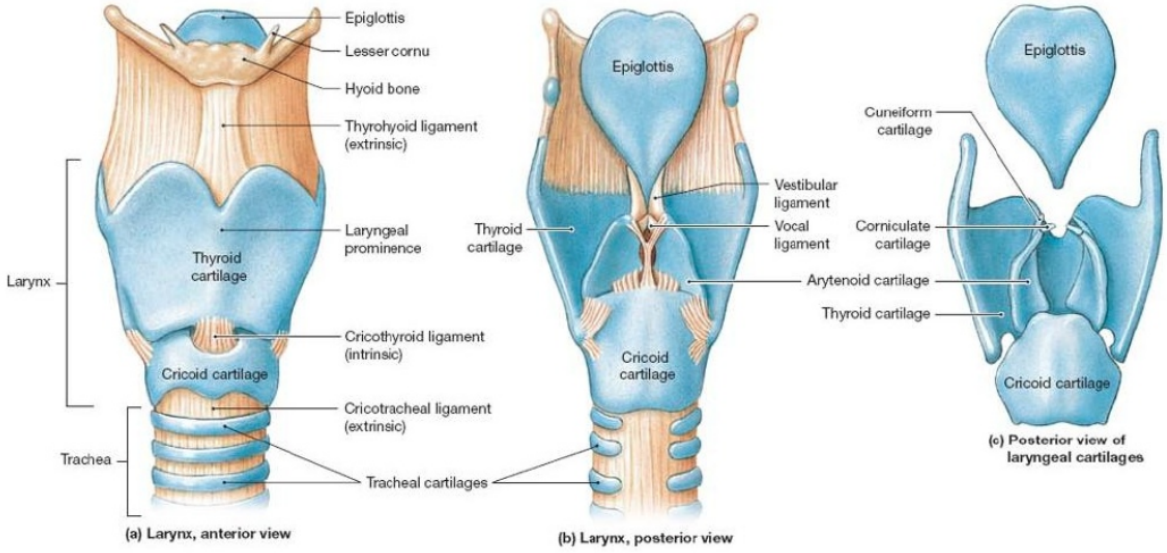

Figure B.1: Anterior, posterior and sagittal view of the larynx, showing compositing cartilages and bones. Figure reproduced from [26].

cartilages, corniculate cartilages and cuneiform cartilages. The movement of vocal folds involves 5 muscles: posterior cricoarytenoid (PCA), lateral cricoarytenoid (LCA), thyroarytenoid (TA), cricothyroid (CT) and interarytenoid (IA) muscle. An anatomy view of the larynx is shown in Figure B.1. The arytenoid cartilages are a small pair of pyramid-shaped structures that sits on top of the cricoid cartilage, to which the vocal folds are attached. As a result the arytenoid cartilages play an important role in help move the vocal folds enabling tension, relaxation or approximation [199], which then made phonation possible as well as ventilation, swallowing, and forced closure manoeuvres such as coughing.

One of the common treatment for unilateral vocal fold pralaysis is through medialisation thryroplasty, this is sometimes followed by arytenoid adduction to reduce the glottal gap occured at the posterior vocal fold area. Various researches have attempted to understand the posturing mechanism by focusing on the motion of arytenoid cartilages around the cricoarytenoid joint (CAJ), as well as the movement of laryngeal muscles causing these motions. With more understanding of the mechanics of cartilages and muscles, laryngeal procedures like medialization could be enhanced.

The arytenoid cartilages are about 17x17x13mm in male and 14x13x12mm in female [200]. Due to its small size and constant movement during vocal fold motions, its articulation mechanism have not yet been confirmed. Nevertheless computational models of arytenoid cartilages and the CAJ have been developed and verified against the range and speed of motion in published vocal fold kinematic data. The movement of arytenoid was thought to be in a 3D dynamic rocking motion initially [201], but Selbie et al. later showed that the CAJ could be viewed as a 2D

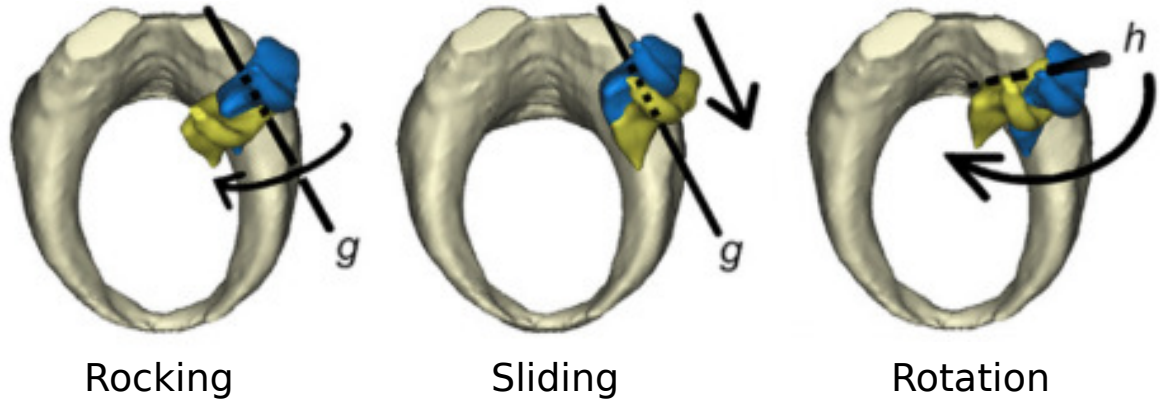

Figure B.2: The rocking, sliding and rotation motions of the arytenoid cartilages. Figure reproduced from [7].

motion derived from 3D rotation analysis [202] and this was further implemented by Titze et al. [203]. Hunter et al. integrated the effect of passive connecting tissues to the existing muscle models to simulate the adduction and abduction of the arytenoid cartilage [204]. Educational computer model has also been implemented to by reconstructing scans of cadavar cartilages by microcomputed tomographic and magnetic resonance imaging (MRI) scanners [205].

Anatomical models have also been developed utilising MRI scans to obtain physiological values and create surface mesh for laryngeal structures [202]. Computerised tomography has also been used to analyse the vertical motion of arytenoid cartlages in pateints [206].

Though advanced computing models have been extensively implemented to model the articulation of arytenoid cartilages and have taken into account material properties, fluid dynamic, tissue composition as well as mechanical forces in muscles and connecting soft tissues, very few mechanical models have been developed. Therefore in order to better visualise the vocal folds and verify the existing theory of the motion of the arytenoid cartilages, we aim to build a mechanical model base on the theory of 3 degree of motion (DOF) of the aryteoid cartlage. This includes movement in 3 DOF as shown in Figure B.2: sliding of the arytenoid along its longitudinal axis, rocking of the arytenoid cartilage during vocal fold abduction and adduction and the rotation of the arytenoid for vocalization, and expiration [7].

B.2 MRI scan

Although structures of the arytenoids have been successfull identified through MRI scan, cadaver larynges were used and therefore the motion of them were not captured. Hence prior to build the mechanical model of arytenoid, we attempted to visualise the motion of aryenoids cartilage by using a high resolution MRI scan with healthy subject. One healthy male subject participated in this experiment under University of Bristol ethics 47961. The participant was asked to breath as usual. A total number of 14 images were produced in the anterior plane using T2-weighted

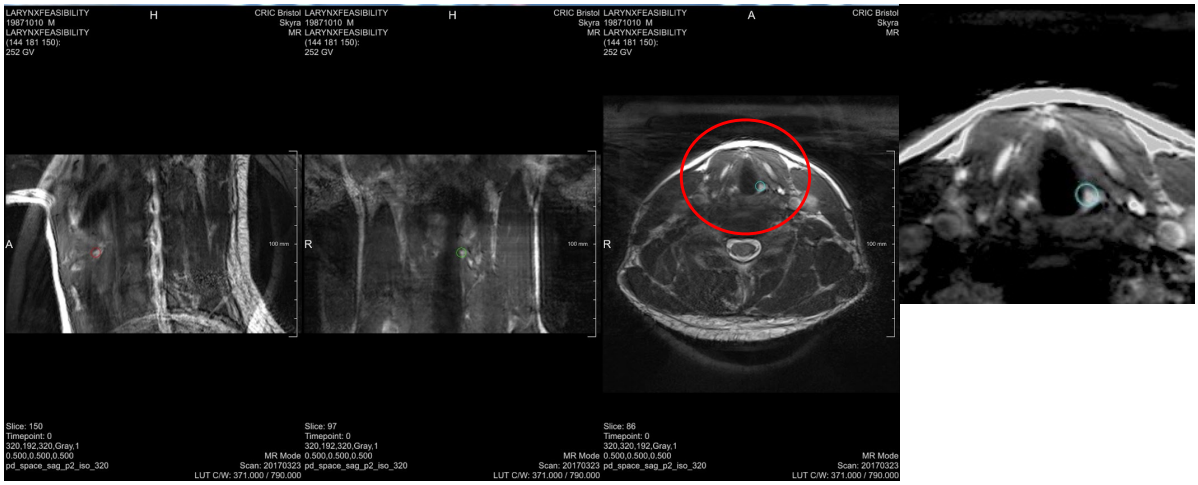

Figure B.3: A sample MRI scan from subject.

scans. A sample scan is shown in Figure B.3. As can be seen from the image, the outline of the arytenoid could be differenciated, however from the resultant images we were not able to identify the movement sequence of the cartilage.

It was said that these high resolution scans could give us the “quasi-static“position of the arytenoids, position which could be used to localise them on a subsequent dynamic scan. However, during a dynamic scan the arytenoids would probably move hence we would either have to hold the position there or wait for the arytenoids to come back to the same position or to take a scan at a certain height, then do the movement and take another scan above or below. We therefore implement the mechanical model based on the articulation theory used by Stork et al. as mentioned in last section as the solution was not feasible.

B.3 Mechanical design

In this mechanical simulator of the arytenoid cartilage, we aim to model the 3 DOF of the movement highlighted by literature. We approached the problem by firstly manufacture a laryngeal cartilage framework for anatomically accurate geometry. This was done by utilising 3D printing with anatomical models produced by Database Center for Life Science (DBCLS) [207]. The cartilages were printed 4 times larger than their original sizes for easier visualisation. Thyroid, crycoid, and arytenoid cartilages were printed and assembled, as shown in Figure B.4. Only one side of the arytenoids was to be articulated to mimic the case of vocal fold paralysis. To create 3 DOF motion of the arytenoid, we used a gear and motor system, as shown in Figure B.5. Two block of aluminium frame were used to house two compartments of this driving design. They were assembled and positioned along the axis of motion marked in Figure B.4.

The compartment that is further away from the arytenoid composed of one Nema 17 stepper motor connecting to a 5mm rod, which links the two aluminium compartment through bearings.

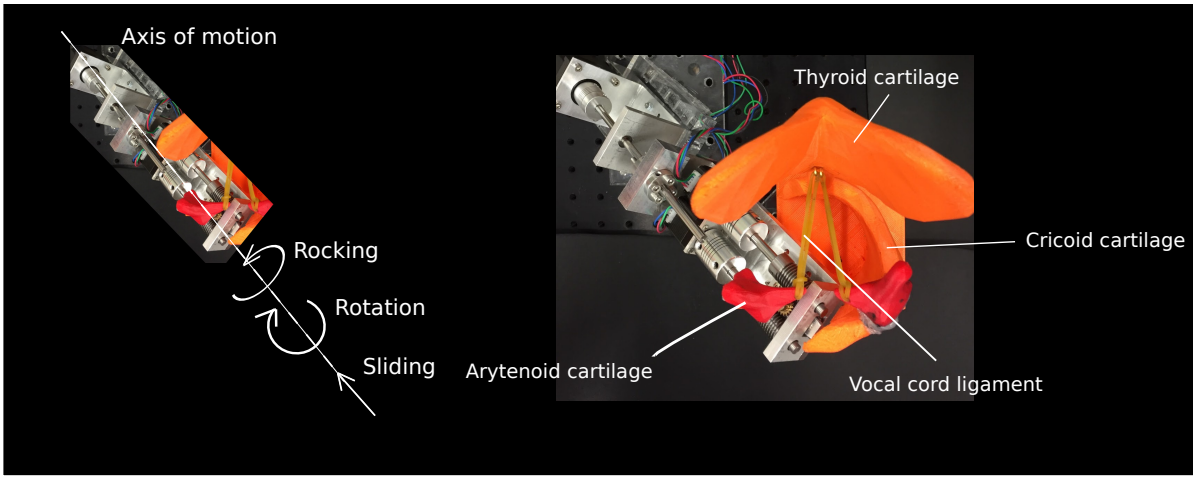

Figure B.4: The anterior view of the mechanical model.

	Men (mean ± SD)	Women (mean ± SD)
Rocking angle (left, degree)	38.7 ± 6.2	35.2 ± 5.6
Rocking angle (right, degree)	37.2 ± 7.3	32.2 ±5.9
Rotation angle (left, degree)	51.4 ± 8.2	51.7 ± 9.5
Rotation angle (right, degree)	50.5 ± 7.9	52.9 ± 9.1
Sliding distance (left, mm)	5.8 ± 1.8	4.7 ± 1.5
Sliding distance (right, mm)	5.5 ± 1.4	4.7 ± 1.5

Table B.1: Anatomical values of the arytenoid movement [7].

This compartment provide the rocking motion.

The compartment that sits closer to the arytenoid provide sliding and rotation. This was done by using worm gears (HPC). A hole was made at the centre of the 3D printed arytenoid cartilage and through which a 3mm rod was used to secure the arytenoid onto a worm wheel, which then sits on a small linear slide. Two worm gears were placed at either sides, driven by Nema 8 stepper motors. The sliding motion was achived by moving both worm gears towards the same direction and the rotation motion was achieved by moving them towards an opposite direction.

Movements at rocking, sliding and rotation were pre-programmed according to literature, shown in Table B.1. The mean physiological values for men were used and timed by 4 in simulation, to match the enlargement of the mechanical model.

B.4 Results

Two demonstrator “vocal cord ligaments” made from elastic bands were attached to the interior of the thyroid for the motion tests of arytenoid.

Figure B.6 shows the resultant movement created utilising the developed mechanical model. A and B show the rocking motion, C and D show the rotation motion, E and F show the sliding

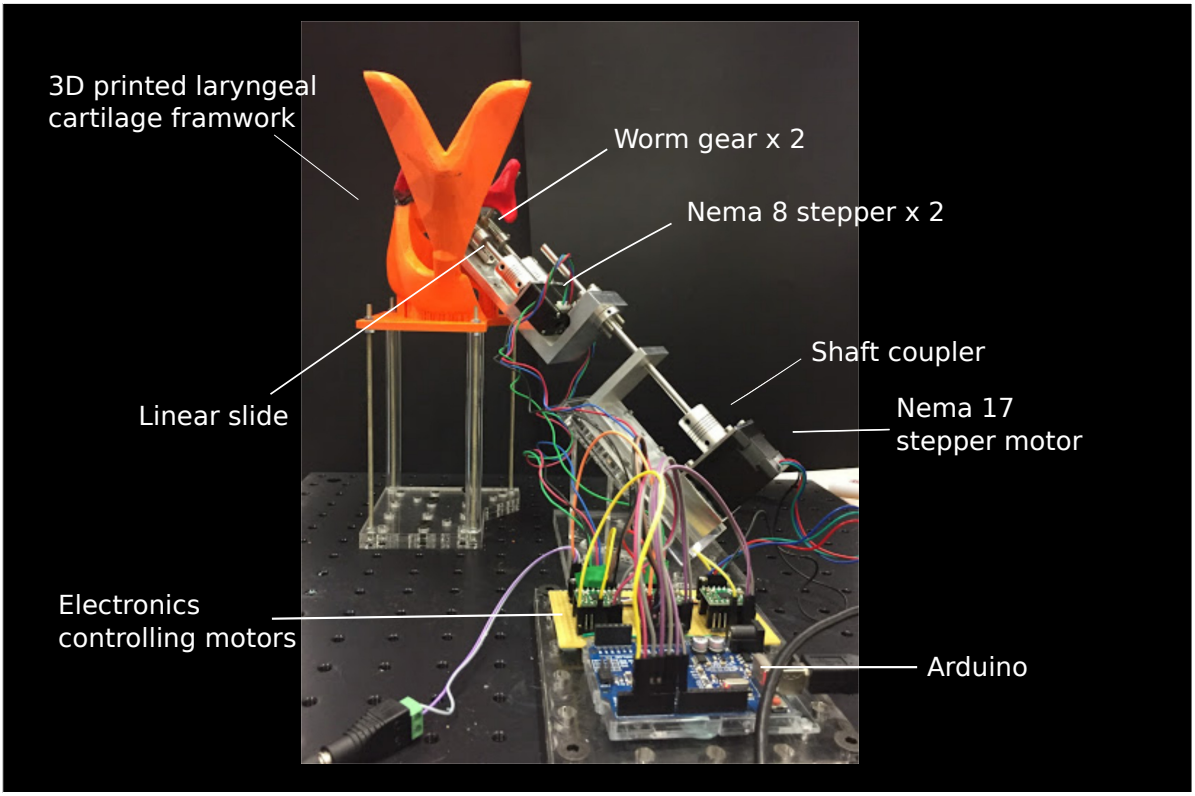

Figure B.5: The side view of the mechanical model.

motion. The three motions are all illustrated in Figure B.6 at their largest displacement/angle. As can be seen, the sliding of the arytenoid cartilage caused less stretching of the on ligaments compared to rocking and rotation. This could be due to the nature of the cricoarytenoid joint that have made the displacement more difficult along the sliding axes, as shown in Table B.1.

B.5 Discussion and further development

In this mechanical model we aim to demonstrate and visualise the 3 DOF of the arytenoid cartilages and in results we tested the 3 motions separately, isolated from the influences from other motions. It should be note that in human larynx, the three motions are always coupled together to achieve optimal articulation for phonation. Also in this model, only the movement of the arytenoid cartilages was considered. Although anatomical correct displacement and angle was used to control the end position of vocal fold ligaments, no force feedback could be gained from this model as muscles that aid articulation were not considered. The limitations of this mechanical simulator could be improved by adding soft materials that model the properties of natural tissue on to the existing cartilage framework component. Further development could also consider miniaturising the rig to a life scale to size as part of its use as a teaching tool.

Although 3D printed laryngeal cartilages are not as anatomically accurate and do not assem-

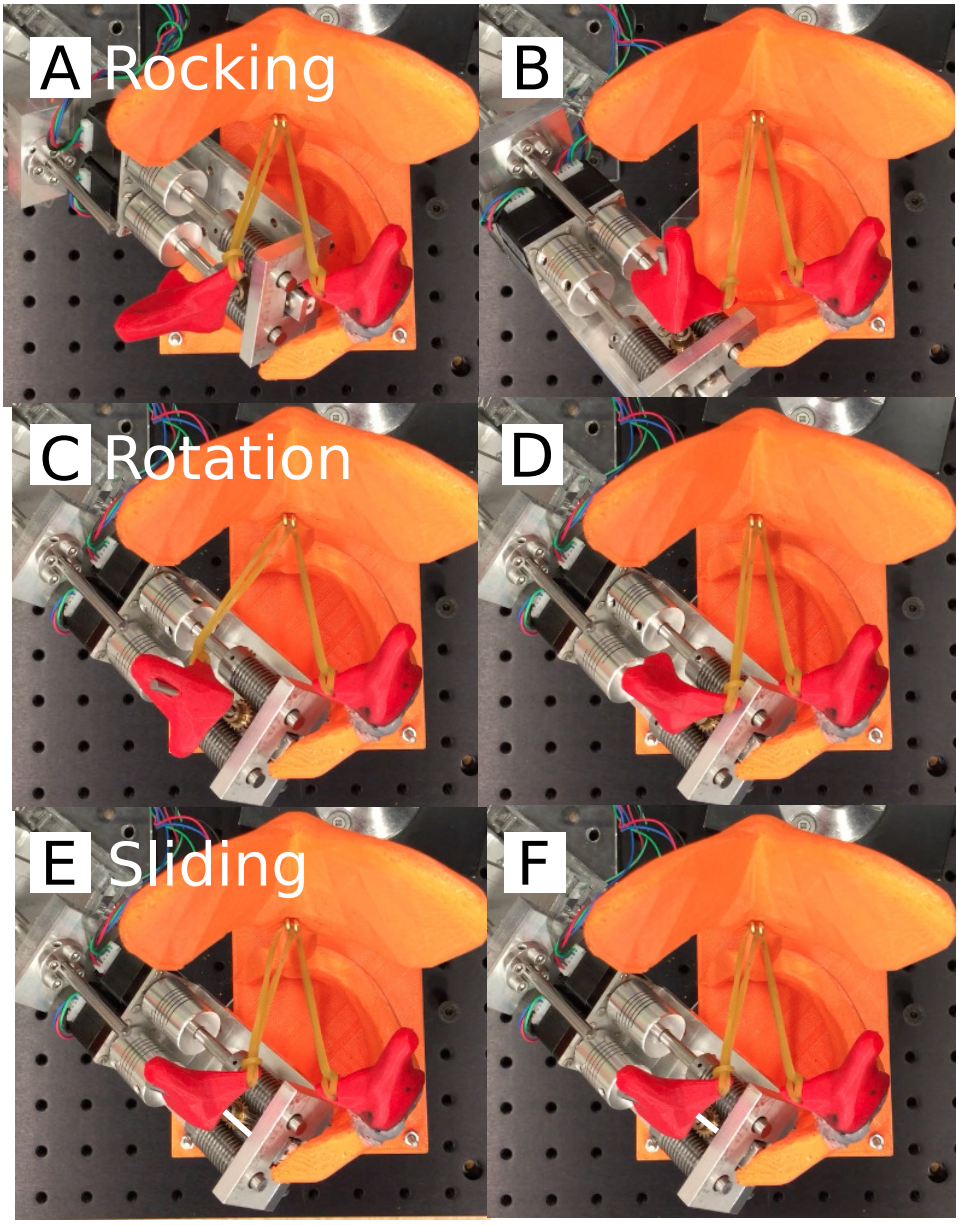

Figure B.6: Three DOF movement of the arytenoid cartilage.

ble tissue properties of a human larynx compared to cadaver larynges, they were chosen over cadaver cartilages for several reasons. First of all, they are easy to assemble for tests. Cadaver larynges will need to be placed under warm water circulation to create a life-like environment for modelling and this is not suitable for this first-stage mechanical simulator development. Secondly, 3D printed cartilages allow the enlargement of dimensions and therefore enable better visualisation and fast prototyping. Last but not least, they are safer, easier to maintain and at a lower cost, which could provide a platform for research, teaching and medical education.

B.6 Conclusion

In this chapter we designed and built a mechanical simulator to model the complex movement of the arytenoid cartilage based on the widely implemented theory that it moves with 3 DOF: sliding, rocking and rotation. Results showed promise towards recreating the deformation of vocal folds ligament in maximal cases. However, this mechanical simulator is completely rigid and did not consider the involvement of laryngeal muscles or the structure of vocal folds. This limitation could be resolved by introducing soft material into the model.

BIBLIOGRAPHY

[1] G. J. Tortora and B. H. Derrickson, *Principles of anatomy and physiology*. John Wiley & Sons, 2008.

[2] W. F. Ganong and K. E. Barrett, *Review of medical physiology*. Appleton & Lange Norwalk, CT, 1995.

[3] S. L. DeBoer, *Emergency Newborn Care*. Trafford on Demand Pub, 2004.

[4] W. Q. Lindh, M. Pooler, C. D. Tamparo, B. M. Dahl, and J. Morris, *Delmar's comprehensive medical assisting: administrative and clinical competencies*. Cengage Learning, 2013.

[5] A. Rodríguez-Molinero, L. Narvaiza, J. Ruiz, and C. Gálvez-Barrón, "Normal respiratory rate and peripheral blood oxygen saturation in the elderly population," *Journal of the American Geriatrics Society*, vol. 61, no. 12, pp. 2238–2240, 2013.

[6] C. Mrudula and M. Krishnaiah, "The study of bronchial tree," *International journal of pharma and bio sciences*, vol. 2, no. 1, pp. 166–172, 2011.

[7] C. Storck, P. Juergens, C. Fischer, M. Wolfensberger, F. Honegger, E. Sorantin, G. Friedrich, and M. Gugatschka, "Biomechanics of the cricoarytenoid joint: three-dimensional imaging and vector analysis," *Journal of voice*, vol. 25, no. 4, pp. 406–410, 2011.

[8] MedlinePlus, "Nerves of layrnx.," 2018. [Online; accessed 05-Nov-2019].

[9] H. Gray, "Anatomy of the human body, by henry gray. thoroughly rev. and re-edited by warren h," *Lewis. Lea & Febiger, Philadelphia*, 1918.

[10] Jkwchui, "Drawing of the left recurrent laryngeal nerve," 2014. [Online; accessed 05-Nov-2019].

[11] Prejun, "vocal cord positions regarding paralyses," 2016. [Online; accessed 05-Nov-2019].

[12] D. T. Ginat, J. E. Small, and D. L. Noujaim, "46 vocal cord augmentation/injection laryngoplasty," *Neuroradiology*, vol. 125, no. 3, p. 357, 2018.

[13] Akshatasbks, "Montgomery thyroplasty implant system.," 2016.
[Online; accessed 05-Nov-2019].

[14] Donald Zhang, "Diagram of arytenoid adduction procedure, lateral view.," 2016.
[Online; accessed 05-Nov-2019].

[15] D. Rus and M. T. Tolley, "Design, fabrication and control of soft robots," *Nature*, vol. 521, no. 7553, pp. 467–475, 2015.

[16] Wikipedia, the free encyclopedia, "Vocal cord paresis," 2016.
[Online; accessed 20-Sep-2016].

[17] "Mayo foundatiion for medical education and research.." `mayoclinic.com`.
[Online; accessed 10-Sep-2019].

[18] I. R. Titze, S. S. Schmidt, and M. R. Titze, "Phonation threshold pressure in a physical model of the vocal fold mucosa," *The Journal of the Acoustical Society of America*, vol. 97, no. 5, pp. 3080–3084, 1995.

[19] R. C. Scherer, D. Shinwari, K. J. De Witt, C. Zhang, B. R. Kucinschi, and A. A. Afjeh, "Intraglottal pressure profiles for a symmetric and oblique glottis with a divergence angle of 10 degrees," *The Journal of the Acoustical Society of America*, vol. 109, no. 4, pp. 1616–1630, 2001.

[20] B. C. of Medicine., "Vocal fold paralysis.." `https://www.researchgate.net/`.
[Online; accessed 10-Sep-2019].

[21] A. Aguirre, "Thyroplasty.." `https://www.youtube.com/watch?v=DXgBsycAu20`.
[Online; accessed 10-Sep-2019].

[22] AresLiam, "Mullins effect," 2013.
[Online; accessed 30-Sep-2019].

[23] P. Rothemund, A. Ainla, L. Belding, D. J. Preston, S. Kurihara, Z. Suo, and G. M. Whitesides, "A soft, bistable valve for autonomous control of soft actuators," *Science Robotics*, vol. 3, no. 16, p. eaar7986, 2018.

[24] L. Belding, B. Baytekin, H. T. Baytekin, P. Rothemund, M. S. Verma, A. Nemiroski, D. Sameoto, B. A. Grzybowski, and G. M. Whitesides, "Slit tubes for semisoft pneumatic actuators," *Advanced Materials*, vol. 30, no. 9, p. 1704446, 2018.

[25] J. T. Overvelde, T. Kloek, J. J. D'haen, and K. Bertoldi, "Amplifying the response of soft actuators by harnessing snap-through instabilities," *Proceedings of the National Academy of Sciences*, vol. 112, no. 35, pp. 10863–10868, 2015.

[26] M. I. MSU, "Anatomy of larynx." `https://www.slideshare.net/ananthatiger/anatomy-of-larynx`, 2010.
[Online; accessed 1-Nov-2019].

[27] S. Takano, T. Nito, N. Tamaruya, M. Kimura, and N. Tayama, "Single institutional analysis of trends over 45 years in etiology of vocal fold paralysis," *Auris Nasus Larynx*, vol. 39, no. 6, pp. 597–600, 2012.

[28] N. Al-Khtoum, N. Shawakfeh, E. Al-Safadi, O. Al-Momani, and K. Hamasha, "Acquired unilateral vocal fold paralysis: Retrospective analysis of a single institutional experience," *North American journal of medical sciences*, vol. 5, no. 12, p. 699, 2013.

[29] S. Gandhi, S. Rai, N. Bhowmick, *et al.*, "Etiological profile of unilateral vocal cord paralysis: A single institutional experience over 10 years," *Journal of Laryngology and Voice*, vol. 4, no. 2, p. 58, 2014.

[30] S. J. S. Toutounchi, M. Eydi, S. E. Golzari, M. R. Ghaffari, and N. Parvizian, "Vocal cord paralysis and its etiologies: a prospective study," *Journal of cardiovascular and thoracic research*, vol. 6, no. 1, p. 47, 2014.

[31] E. C. Ward and C. J. van As-Brooks, *Head and neck cancer: treatment, rehabilitation, and outcomes*.
Plural Publishing, 2014.

[32] C. R. UK, "Head and neck cancers statistics." `https://www.cancerresearchuk.org`, 2016.
[Online; accessed 1-Aug-2019].

[33] I. Ganly, S. Patel, J. Matsuo, B. Singh, D. Kraus, J. Boyle, R. Wong, N. Lee, D. G. Pfister, A. Shaha, *et al.*, "Postoperative complications of salvage total laryngectomy," *Cancer: Interdisciplinary International Journal of the American Cancer Society*, vol. 103, no. 10, pp. 2073–2081, 2005.

[34] S. S. Chandrasekhar, G. W. Randolph, M. D. Seidman, R. M. Rosenfeld, P. Angelos, J. Barkmeier-Kraemer, M. S. Benninger, J. H. Blumin, G. Dennis, J. Hanks, *et al.*, "Clinical practice guideline: improving voice outcomes after thyroid surgery," *Otolaryngology—Head and Neck Surgery*, vol. 148, no. 6_suppl, pp. S1–S37, 2013.

[35] D. Mozaffarian, E. J. Benjamin, A. S. Go, D. K. Arnett, M. J. Blaha, M. Cushman, S. De Ferranti, J.-P. Després, H. J. Fullerton, V. J. Howard, *et al.*, "Executive summary: heart

disease and stroke statistics—2015 update: a report from the american heart association," *Circulation*, vol. 131, no. 4, pp. 434–441, 2015.

[36] G. M. Gardner, M. M. Smith, K. L. Yaremchuk, and E. L. Peterson, "The cost of vocal fold paralysis after thyroidectomy," *The Laryngoscope*, vol. 123, no. 6, pp. 1455–1463, 2013.

[37] M. E. Giannaccini, K. Yue, J. Graveston, M. Birchall, A. Conn, and J. Rossiter, "Respiratory simulator for robotic respiratory tract treatments," in *2017 IEEE International Conference on Robotics and Biomimetics (ROBIO)*, pp. 2314–2319, IEEE, 2017.

[38] V. Negus, "The function of the epiglottis," *Journal of anatomy*, vol. 62, no. Pt 1, p. 1, 1927.

[39] J. Hydman, *Recurrent laryngeal nerve injury*.
Institutionen för klinisk neurovetenskap/Department of Clinical Neuroscience, 2008.

[40] D. R. Fuller, J. Pimentel, and B. M. Peregoy, *Applied Anatomy & Physiology for Speech-language Pathology and Audiology*.
2012.

[41] H. S. Choi, M. Ye, and G. S. Berke, "Function of the interarytenoid (ia) muscle in phonation: in vivo laryngeal model," *Yonsei Medical Journal*, vol. 36, no. 1, pp. 58–67, 1995.

[42] K. L. Moore, A. F. Dalley, and A. M. Agur, *Clinically oriented anatomy*.
Lippincott Williams & Wilkins, 2013.

[43] M. Schünke, U. Schumacher, and E. Schulte, *Comprar Head and Neuroanatomy (THIEME Atlas of Anatomy) | Michael Schuenke | 9783131421012 | Thieme*.
Thieme, 2007.

[44] A. D. Rubin and R. T. Sataloff, "Vocal fold paresis and paralysis," *Otolaryngologic Clinics of North America*, vol. 40, no. 5, pp. 1109–1131, 2007.

[45] L. Sulica and A. Blitzer, "Vocal fold paresis: evidence and controversies," *Current opinion in otolaryngology & head and neck surgery*, vol. 15, no. 3, pp. 159–162, 2007.

[46] L. Sulica, "Vocal fold paresis: an evolving clinical concept," *Current Otorhinolaryngology Reports*, vol. 1, no. 3, pp. 158–162, 2013.

[47] M. N. Syamal and M. S. Benninger, "Vocal fold paresis: a review of clinical presentation, differential diagnosis, and prognostic indicators," *Current opinion in otolaryngology & head and neck surgery*, vol. 24, no. 3, pp. 197–202, 2016.

[48] M. Grossman, "Experimentelle beitrage zur lehre von der posticuslahmung," *Arch Laryngol Rhinol*, vol. 6, p. 282, 1897.

[49] B. Benjamin, "Vocal cord paralysis, synkinesis and vocal fold motion impairment," 2003.

[50] P. S. Mallur and C. A. Rosen, "Vocal fold injection: review of indications, techniques, and materials for augmentation," *Clinical and experimental otorhinolaryngology*, vol. 3, no. 4, p. 177, 2010.

[51] M. Remacle and H. E. Eckel, *Surgery of larynx and trachea*.
Springer, 2010.

[52] N. Isshiki, M. Tanabe, and M. Sawada, "Arytenoid adduction for unilateral vocal cord paralysis," *Archives of Otolaryngology*, vol. 104, no. 10, pp. 555–558, 1978.

[53] H. M. Tucker, "Reinnervation of the unilaterally paralyzed larynx," *Annals of Otology, Rhinology & Laryngology*, vol. 86, no. 6, pp. 789–794, 1977.

[54] M. May and Q. Beery, "Muscle-nerve pedicle laryngeal reinnervation," *The Laryngoscope*, vol. 96, no. 11, pp. 1196–1200, 1986.

[55] E. Yumoto, T. Sanuki, Y. Toya, N. Kodama, and Y. Kumai, "Nerve-muscle pedicle flap implantation combined with arytenoid adduction," *Archives of Otolaryngology–Head & Neck Surgery*, vol. 136, no. 10, pp. 965–969, 2010.

[56] R. C. Paniello, J. D. Edgar, D. Kallogjeri, and J. F. Piccirillo, "Medialization versus reinnervation for unilateral vocal fold paralysis: a multicenter randomized clinical trial," *The Laryngoscope*, vol. 121, no. 10, pp. 2172–2179, 2011.

[57] N. Kodama, Y. Kumai, T. Sanuki, and E. Yumoto, "Arytenoid adduction combined with nerve-muscle pedicle flap implantation or type i thyroplasty," *The Laryngoscope*, vol. 127, no. 1, pp. 159–166, 2017.

[58] S. Kim, C. Laschi, and B. Trimmer, "Soft robotics: a bioinspired evolution in robotics," *Trends in biotechnology*, vol. 31, no. 5, pp. 287–294, 2013.

[59] M. Cianchetti, C. Laschi, A. Menciassi, and P. Dario, "Biomedical applications of soft robotics," *Nature Reviews Materials*, vol. 3, no. 6, p. 143, 2018.

[60] V. Vitiello, S.-L. Lee, T. P. Cundy, and G.-Z. Yang, "Emerging robotic platforms for minimally invasive surgery," *IEEE reviews in biomedical engineering*, vol. 6, pp. 111–126, 2012.

[61] R. S. Diteesawat, T. Helps, M. Taghavi, and J. Rossiter, "High strength bubble artificial muscles for walking assistance," in *2018 IEEE International Conference on Soft Robotics (RoboSoft)*, pp. 388–393, IEEE, 2018.

[62] Y.-L. Park, B.-r. Chen, N. O. Pérez-Arancibia, D. Young, L. Stirling, R. J. Wood, E. C. Goldfield, and R. Nagpal, "Design and control of a bio-inspired soft wearable robotic device for ankle–foot rehabilitation," *Bioinspiration & biomimetics*, vol. 9, no. 1, p. 016007, 2014.

[63] S. Lee, J. Kim, L. Baker, A. Long, N. Karavas, N. Menard, I. Galiana, and C. J. Walsh, "Autonomous multi-joint soft exosuit with augmentation-power-based control parameter tuning reduces energy cost of loaded walking," *Journal of neuroengineering and rehabilitation*, vol. 15, no. 1, p. 66, 2018.

[64] E. T. Roche, M. A. Horvath, I. Wamala, A. Alazmani, S.-E. Song, W. Whyte, Z. Machaidze, C. J. Payne, J. C. Weaver, G. Fishbein, *et al.*, "Soft robotic sleeve supports heart function," *Science translational medicine*, vol. 9, no. 373, p. eaaf3925, 2017.

[65] S. Miyashita, S. Guitron, K. Yoshida, S. Li, D. D. Damian, and D. Rus, "Development of an artificial urethral valve using sma actuators," in *2016 IEEE International Conference on Robotics and Automation (ICRA)*, pp. 909–916, IEEE, 2016.

[66] D. D. Damian, K. Price, S. Arabagi, I. Berra, Z. Machaidze, S. Manjila, S. Shimada, A. Fabozzo, G. Arnal, D. Van Story, *et al.*, "In vivo tissue regeneration with robotic implants," *Science Robotics*, vol. 3, no. 14, p. eaaq0018, 2018.

[67] S. Chonan, Z. Jiang, J. Tani, S. Orikasa, Y. Tanahashi, T. Takagi, M. Tanaka, and J. Tanikawa, "Development of an artificial urethral valve using sma actuators," *Smart Materials and Structures*, vol. 6, no. 4, p. 410, 1997.

[68] Y. Haga, T. Mineta, K. Totsu, W. Makishi, and M. Esashi, "Development of active catheter, active guide wire and micro sensor systems," *Interventional Neuroradiology*, vol. 7, no. 1_suppl, pp. 125–130, 2001.

[69] K. Ikuta, H. Ichikawa, K. Suzuki, and T. Yamamoto, "Micro hydrodynamic actuated multiple segments catheter for safety minimally invasive therapy," in *2003 IEEE International Conference on Robotics and Automation (Cat. No. 03CH37422)*, vol. 2, pp. 2640–2645, IEEE, 2003.

[70] J. Hughes, U. Culha, F. Giardina, F. Guenther, A. Rosendo, and F. Iida, "Soft manipulators and grippers: a review," *Frontiers in Robotics and AI*, vol. 3, p. 69, 2016.

[71] M. Wehner, M. T. Tolley, Y. Mengüç, Y.-L. Park, A. Mozeika, Y. Ding, C. Onal, R. F. Shepherd, G. M. Whitesides, and R. J. Wood, "Pneumatic energy sources for autonomous and wearable soft robotics," *Soft robotics*, vol. 1, no. 4, pp. 263–274, 2014.

[72] S. A. Watts, L. Tabor, and E. K. Plowman, "To cough or not to cough? examining the potential utility of cough testing in the clinical evaluation of swallowing," *Current physical medicine and rehabilitation reports*, vol. 4, no. 4, pp. 262–276, 2016.

[73] A. B. Chang, "The physiology of cough," *Paediatric respiratory reviews*, vol. 7, no. 1, pp. 2–8, 2006.

[74] F. J. Hilgers, A. H. Ackerstaff, N. K. Aaronson, P. F. Schouwenburg, and N. Van Zandwij, "Physical and psychosocial consequences of total laryngectomy," *Clinical Otolaryngology & Allied Sciences*, vol. 15, no. 5, pp. 421–425, 1990.

[75] S. Bień, S. Okła, C. J. van As-Brooks, and A. H. Ackerstaff, "The effect of a heat and moisture exchanger (provox® hme) on pulmonary protection after total laryngectomy: a randomized controlled study," *European Archives of Oto-Rhino-Laryngology*, vol. 267, no. 3, pp. 429–435, 2010.

[76] W. D. Man, D. Kyroussis, T. A. Fleming, A. Chetta, F. Harraf, N. Mustfa, G. F. Rafferty, M. I. Polkey, and J. Moxham, "Cough gastric pressure and maximum expiratory mouth pressure in humans," *American journal of respiratory and critical care medicine*, vol. 168, no. 6, pp. 714–717, 2003.

[77] J. A. Evans and W. A. Whitelaw, "The assessment of maximal respiratory mouth pressures in adults," *Respiratory care*, vol. 54, no. 10, pp. 1348–1359, 2009.

[78] B. Button, H. P. Goodell, E. Atieh, Y.-C. Chen, R. Williams, S. Shenoy, E. Lackey, N. T. Shenkute, L.-H. Cai, R. G. Dennis, *et al.*, "Roles of mucus adhesion and cohesion in cough clearance," *Proceedings of the National Academy of Sciences*, vol. 115, no. 49, pp. 12501–12506, 2018.

[79] B. F. Dickey, "What it takes for a cough to expel mucus from the airway," *Proceedings of the National Academy of Sciences*, vol. 115, no. 49, pp. 12340–12342, 2018.

[80] M. King, G. Brock, and C. Lundell, "Clearance of mucus by simulated cough," *Journal of Applied Physiology*, vol. 58, no. 6, pp. 1776–1782, 1985.

[81] P. Scherer and L. Burtz, "Fluid mechanical experiments relevant to coughing," *Journal of biomechanics*, vol. 11, no. 4, pp. 183–187, 1978.

[82] M. Suleman, K. Abaza, C. Gornall, W. Kinnear, J. Wills, and R. Mahajan, "The effect of a mechanical glottis on peak expiratory flow rate and time to peak flow during a peak expiratory flow manoeuvre: a study in normal subjects and patients with motor neurone disease," *Anaesthesia*, vol. 59, no. 9, pp. 872–875, 2004.

[83] U. Mellies and C. Goebel, "Optimum insufflation capacity and peak cough flow in neuromuscular disorders," *Annals of the American Thoracic Society*, vol. 11, no. 10, pp. 1560–1568, 2014.

[84] C. Dohna-Schwake, R. Ragette, H. Teschler, T. Voit, and U. Mellies, "Predictors of severe chest infections in pediatric neuromuscular disorders," *Neuromuscular disorders*, vol. 16, no. 5, pp. 325–328, 2006.

[85] S.-W. Kang and J. R. Bach, "Maximum insufflation capacity: vital capacity and cough flows in neuromuscular disease," *American journal of physical medicine & rehabilitation*, vol. 79, no. 3, pp. 222–227, 2000.

[86] G. A. Fontana, T. Pantaleo, F. Lavorini, D. Mutolo, G. Polli, and M. Pistolesi, "Coughing in laryngectomized patients," *American journal of respiratory and critical care medicine*, vol. 160, no. 5, pp. 1578–1584, 1999.

[87] M. Chatwin, M. Toussaint, M. R. Gonçalves, N. Sheers, U. Mellies, J. Gonzales-Bermejo, J. Sancho, B. Fauroux, T. Andersen, B. Hov, *et al.*, "Airway clearance techniques in neuromuscular disorders: a state of the art review," *Respiratory medicine*, vol. 136, pp. 98–110, 2018.

[88] S. Yim and M. Sitti, "Shape-programmable soft capsule robots for semi-implantable drug delivery," *IEEE Transactions on Robotics*, vol. 28, no. 5, pp. 1198–1202, 2012.

[89] W. A. Choi, J. H. Park, D. H. Kim, and S.-W. Kang, "Cough assistance device for patients with glottis dysfunction and/or tracheostomy," *Journal of rehabilitation medicine*, vol. 44, no. 4, pp. 351–354, 2012.

[90] C. Dohna-Schwake, R. Ragette, H. Teschler, T. Voit, and U. Mellies, "Ippb-assisted coughing in neuromuscular disorders," *Pediatric pulmonology*, vol. 41, no. 6, pp. 551–557, 2006.

[91] R. Mahajan, P. Singh, G. Murty, and A. Aitkenhead, "Relationship between expired lung volume, peak flow rate and peak velocity time during a voluntary cough manoeuvre," *British Journal of Anaesthesia*, vol. 72, no. 3, pp. 298–301, 1994.

[92] S. T. Kulnik, V. MacBean, S. S. Birring, J. Moxham, G. F. Rafferty, and L. Kalra, "Accuracy of portable devices in measuring peak cough flow," *Physiological measurement*, vol. 36, no. 2, p. 243, 2015.

[93] G. N. Takara, G. Ruas, B. V. Pessoa, L. K. Jamami, V. A. P. D. Lorenzo, and M. Jamami, "Comparison of five portable peak flow meters," *Clinics*, vol. 65, no. 5, pp. 469–474, 2010.

[94] F. Faul, E. Erdfelder, A.-G. Lang, and A. Buchner, "G* power 3: A flexible statistical power analysis program for the social, behavioral, and biomedical sciences," *Behavior research methods*, vol. 39, no. 2, pp. 175–191, 2007.

[95] R. Torres-Castro, M. Otto, H. Puppo, R. Vera, M. Barros, and J. Vilaró, "Difference in assessment of peak cough flow on healthy subjects using mouthpiece and facemask techniques," 2013.

[96] R. J. Knudson, J. Mead, and D. E. Knudson, "Contribution of airway collapse to supramaximal expiratory flows.," *Journal of Applied Physiology*, vol. 36, no. 6, pp. 653–667, 1974.

[97] N. Yanagihara, H. Von Leden, and E. Werner-Kukuk, "The physical parameters of cough: the larynx in a normal single cough," *Acta oto-laryngologica*, vol. 61, no. 1-6, pp. 495–510, 1966.

[98] F. D. McCool, "Global physiology and pathophysiology of cough: Accp evidence-based clinical practice guidelines," *Chest*, vol. 129, no. 1, pp. 48S–53S, 2006.

[99] S. Young, N. Abdul-Sattar, and D. Caric, "Glottic closure and high flows are not essential for productive cough.," *Bulletin europeen de physiopathologie respiratoire*, vol. 23, p. 11s, 1987.

[100] K. F. Chung and I. D. Pavord, "Prevalence, pathogenesis, and causes of chronic cough," *The Lancet*, vol. 371, no. 9621, pp. 1364–1374, 2008.

[101] A. Szeinberg, E. Tabachnik, N. Rashed, F. J. McLaughlin, S. England, C. A. Bryan, and H. Levison, "Cough capacity in patients with muscular dystrophy," *Chest*, vol. 94, no. 6, pp. 1232–1235, 1988.

[102] S. Kang, J. Shin, C. Park, J. Moon, D. Rha, and D. Cho, "Relationship between inspiratory muscle strength and cough capacity in cervical spinal cord injured patients," *Spinal Cord*, vol. 44, no. 4, pp. 242–248, 2006.

[103] G. J. Tortora, B. H. Derrickson, B. Burkett, D. Dye, J. Cooke, T. Diversi, M. McKean, R. Mellifont, L. Samalia, and G. Peoples, "Principles of anatomy and physiology: 1st australasian edition," 2016.

[104] F. E. Cardoso, L. C. de Abreu, R. D. Raimundo, N. A. Faustino, S. F. Araújo, V. E. Valenti, M. A. Sato, S. R. Martins, and J. A. Torquato, "Evaluation of peak cough flow in brazilian healthy adults," *International archives of medicine*, vol. 5, no. 1, p. 25, 2012.

[105] C. E. Stepp, J. T. Heaton, and R. E. Hillman, "Post-laryngectomy speech respiration patterns," *Annals of Otology, Rhinology & Laryngology*, vol. 117, no. 8, pp. 557–563, 2008.

[106] D. Lasserson, K. Mills, R. Arunachalam, M. Polkey, J. Moxham, and L. Kalra, "Differences in motor activation of voluntary and reflex cough in humans," *Thorax*, vol. 61, no. 8, pp. 699–705, 2006.

[107] M. Lacombe, L. D. A. Castrillo, A. Boré, D. Chapeau, E. Horvat, I. Vaugier, M. Lejaille, D. Orlikowski, H. Prigent, and F. Lofaso, "Comparison of three cough-augmentation techniques in neuromuscular patients: mechanical insufflation combined with manually assisted cough, insufflation-exsufflation alone and insufflation-exsufflation combined with manually assisted cough," *Respiration*, vol. 88, no. 3, pp. 215–222, 2014.

[108] K. P. Strohl, J. P. Butler, and A. Malhotra, "Mechanical properties of the upper airway," *Comprehensive Physiology*, vol. 2, no. 3, pp. 1853–1872, 2012.

[109] E. R. Weibel and D. M. Gomez, "Architecture of the human lung: Use of quantitative methods establishes fundamental relations between size and number of lung structures," *Science*, vol. 137, no. 3530, pp. 577–585, 1962.

[110] E. R. Weibel, "A retrospective of lung morphometry: from 1963 to present," 2013.

[111] L. National Heart and B. Institute, "How the lungs work," 2018.
[Online; accessed 05-Nov-2019].

[112] F. S. Grodins, J. S. Gray, K. R. Schroeder, A. L. Norins, and R. W. Jones, "Respiratory responses to co2 inhalation. a theoretical study of a nonlinear biological regulator," *Journal of applied physiology*, vol. 7, no. 3, pp. 283–308, 1954.

[113] F. S. Grodins, J. Buell, and A. J. Bart, "Mathematical analysis and digital simulation of the respiratory control system.," *Journal of applied physiology*, vol. 22, no. 2, pp. 260–276, 1967.

[114] W. Fincham and F. Tehrani, "A mathematical model of the human respiratory system," *Journal of biomedical engineering*, vol. 5, no. 2, pp. 125–133, 1983.

[115] L. Chiari, G. Avanzolini, and M. Ursino, "A comprehensive simulator of the human respiratory system: validation with experimental and simulated data," *Annals of biomedical engineering*, vol. 25, no. 6, pp. 985–999, 1997.

[116] T. B. Martonen, L. Quan, Z. Zhang, and C. Musante, "Flow simulation in the human upper respiratory tract," *Cell biochemistry and biophysics*, vol. 37, no. 1, pp. 27–36, 2002.

[117] P. W. Longest and S. Vinchurkar, "Validating cfd predictions of respiratory aerosol deposition: effects of upstream transition and turbulence," *Journal of biomechanics*, vol. 40, no. 2, pp. 305–316, 2007.

[118] T. B. Martonen, Z. Zhang, G. Yue, and C. Musante, "Fine particle deposition within human nasal airways.," *Inhalation toxicology*, vol. 15, no. 4, pp. 283–303, 2003.

[119] N. Nowak, P. P. Kakade, and A. V. Annapragada, "Computational fluid dynamics simulation of airflow and aerosol deposition in human lungs," *Annals of biomedical engineering*, vol. 31, no. 4, pp. 374–390, 2003.

[120] M. Rahimi-Gorji, O. Pourmehran, M. Gorji-Bandpy, and T. Gorji, "Cfd simulation of airflow behavior and particle transport and deposition in different breathing conditions through the realistic model of human airways," *Journal of Molecular Liquids*, vol. 209, pp. 121–133, 2015.

[121] D. K. Walters, G. W. Burgreen, D. M. Lavallee, D. S. Thompson, and R. L. Hester, "Efficient, physiologically realistic lung airflow simulations," *IEEE Transactions on Biomedical Engineering*, vol. 58, no. 10, pp. 3016–3019, 2011.

[122] L. Xue, H. Fan, W. Shi, D. Ge, Y. Zhang, Q. Wang, and Y. Yuan, "Preoperative 3-dimensional computed tomography lung simulation before video-assisted thoracoscopic anatomic segmentectomy for ground glass opacity in lung," *Journal of thoracic disease*, vol. 10, no. 12, p. 6598, 2018.

[123] N. R. MacIntyre, "Respiratory system simulations and modeling," *Respiratory care*, vol. 49, no. 4, pp. 401–409, 2004.

[124] K. Kunkler, "The role of medical simulation: an overview," *The International Journal of Medical Robotics and Computer Assisted Surgery*, vol. 2, no. 3, pp. 203–210, 2006.

[125] R. Pasteka, M. Forjan, S. Sauermann, and A. Drauschke, "Electro-mechanical lung simulator using polymer and organic human lung equivalents for realistic breathing simulation," *Scientific Reports*, vol. 9, no. 1, pp. 1–12, 2019.

[126] R. T. Scaramuzzo, M. Ciantelli, I. Baldoli, L. Bellanti, M. Gentile, F. Cecchi, E. Sigali, S. Tognarelli, P. Ghirri, S. Mazzoleni, *et al.*, "Mechatronic respiratory system simulator for neonatal applications (meressina) project: a novel bioengineering goal," *Medical devices (Auckland, NZ)*, vol. 6, p. 115, 2013.

[127] A. Verbraak, J. Beneken, J. Bogaard, and A. Versprille, "Computer-controlled mechanical lung model for application in pulmonary function studies," *Medical and Biological Engineering and Computing*, vol. 33, no. 6, pp. 776–783, 1995.

[128] S. Mesic, R. Babuska, H. C. Hoogsteden, and A. F. Verbraak, "Computer-controlled mechanical simulation of the artificially ventilated human respiratory system," *IEEE transactions on biomedical engineering*, vol. 50, no. 6, pp. 731–743, 2003.

[129] Y. Shi, S. Ren, M. Cai, W. Xu, and Q. Deng, "Pressure dynamic characteristics of pressure controlled ventilation system of a lung simulator," *Computational and mathematical methods in medicine*, vol. 2014, 2014.

[130] J. Kim, Y. Lee, H. Shin, S. Ji, S. Park, J. Kim, H. Jang, and Y. Kang, "Development of deformable moving lung phantom to simulate respiratory motion in radiotherapy," *Medical Dosimetry*, vol. 41, no. 2, pp. 113–117, 2016.

[131] V. Meka and J. Van Oostrom, "Bellows-less lung system for the human patient simulator," *Medical and Biological Engineering and Computing*, vol. 42, no. 3, pp. 413–418, 2004.

[132] V. David, M. Forjan, T. Steiner, Z. Bureš, and A. Drauschke, "Mechanical and electrical specifications of the active lung simulator i-lung–development of i-lung 1.0 to i-lung 2.0," *IFAC Proceedings Volumes*, vol. 46, no. 28, pp. 13–23, 2013.

[133] A. Perez del Palomar, O. Trabelsi, A. Mena, J. López-Villalobos, A. Ginel, and M. Doblaré, "Patient-specific models of human trachea to predict mechanical consequences of endoprosthesis implantation," *Philosophical Transactions of the Royal Society A: Mathematical, Physical and Engineering Sciences*, vol. 368, no. 1921, pp. 2881–2896, 2010.

[134] P. W. Longest and J. Xi, "Effectiveness of direct lagrangian tracking models for simulating nanoparticle deposition in the upper airways," *Aerosol Science and Technology*, vol. 41, no. 4, pp. 380–397, 2007.

[135] J. Russo, R. Robinson, and M. J. Oldham, "Effects of cartilage rings on airflow and particle deposition in the trachea and main bronchi," *Medical engineering & physics*, vol. 30, no. 5, pp. 581–589, 2008.

[136] B. Zhang, C. Zhu, Z. Ji, and C.-H. Lin, "Design and characterization of a cough simulator," *Journal of breath research*, vol. 11, no. 1, p. 016014, 2017.

[137] I. MEDICAL, "Asl 5000 breathing simulator." `https://www.ingmarmed.com/product/asl-5000-breathing-simulator/`.
[Online; accessed 21-Sep-2020].

[138] M. Instruments, "Adult lung simulators."
[Online; accessed 21-Sep-2020].

[139] F. MEDICAL, "Accu lung precision test lung."
[Online; accessed 21-Sep-2020].

[140] M. Daroszewski, M. Szpinda, M. Wiśniewski, P. Flisiński, A. Szpinda, A. WoŸniak, A. Kosiński, M. Grzybiak, and C. Mila-Kierzenkowska, "Tracheo-bronchial angles in the human fetus–an anatomical, digital, and statistical study," *Medical science monitor basic research*, vol. 19, p. 194, 2013.

[141] Y. Premakumar, M. Griffin, and M. Szarko, "Morphometric characterisation of human tracheas: focus on cartilaginous ring variation," *BMC research notes*, vol. 11, no. 1, p. 32, 2018.

[142] E. Breatnach, G. C. Abbott, and R. G. Fraser, "Dimensions of the normal human trachea," *American Journal of Roentgenology*, vol. 142, no. 5, pp. 903–906, 1984.

[143] U. Cinar, S. Halezeroglu, E. Okur, M. A. Inanici, and S. Kayaoglu, "Tracheal length in adult human: the results of 100 autopsies," *Int. j. morphol*, vol. 34, no. 1, pp. 232–236, 2016.

[144] S. Sakuraba, R. Serita, J. Kuribayashi, S. Kosugi, H. Arisaka, K. Yoshida, and J. Takeda, "Comparison of tracheal diameter measured by chest x-ray and by computed tomography," *Anesthesiology research and practice*, vol. 2010, 2010.

[145] K. S. Kamel, G. Lau, and M. D. Stringer, "In vivo and in vitro morphometry of the human trachea," *Clinical Anatomy*, vol. 22, no. 5, pp. 571–579, 2009.

[146] S. Mehta and H. Myat, "The cross-sectional shape and circumference of the human trachea.," *Annals of the Royal College of Surgeons of England*, vol. 66, no. 5, p. 356, 1984.

[147] A. Nunn and I. Gregg, "New regression equations for predicting peak expiratory flow in adults.," *BMj*, vol. 298, no. 6680, pp. 1068–1070, 1989.

[148] K. Ward, J. Seymour, J. Steier, C. Jolley, M. Polkey, L. Kalra, and J. Moxham, "Acute ischaemic hemispheric stroke is associated with impairment of reflex in addition to voluntary cough," *European Respiratory Journal*, vol. 36, no. 6, pp. 1383–1390, 2010.

[149] I. R. Titze and D. W. Martin, "Principles of voice production," 1998.

[150] B. Rousseau, S. Hirano, T. D. Scheidt, N. V. Welham, S. L. Thibeault, R. W. Chan, and D. M. Bless, "Characterization of vocal fold scarring in a canine model," *The Laryngoscope*, vol. 113, no. 4, pp. 620–627, 2003.

[151] M. Dollinger, J. Kobler, D. A Berry, D. D Mehta, G. Luegmair, and C. Bohr, "Experiments on analysing voice production: Excised (human, animal) and in vivo (animal) approaches," *Current bioinformatics*, vol. 6, no. 3, pp. 286–304, 2011.

[152] S. Kniesburges, S. L Thomson, A. Barney, M. Triep, P. Sidlof, J. Horacek, C. Brucker, and S. Becker, "In vitro experimental investigation of voice production," *Current bioinformatics*, vol. 6, no. 3, pp. 305–322, 2011.

[153] D. M. Bless, N. V. Welham, S. Hirano, H. Nagai, D. W. Montequin, B. Rousseau, and C. N. Ford, "Growth factor therapy for vocal fold scarring in a canine model," *Annals of Otology, Rhinology & Laryngology*, vol. 113, no. 10, pp. 777–785, 2004.

[154] S. Ohno, S. Hirano, S.-I. Kanemaru, Y. Kitani, T. Kojima, I. Tateya, T. Nakamura, and J. Ito, "Implantation of an atelocollagen sponge with autologous bone marrow—derived mesenchymal stromal cells for treatment of vocal fold scarring in a canine model," *Annals of Otology, Rhinology & Laryngology*, vol. 120, no. 6, pp. 401–408, 2011.

[155] A. Suehiro, S. Hirano, Y. Kishimoto, B. Rousseau, T. Nakamura, and J. Ito, "Treatment of acute vocal fold scar with local injection of basic fibroblast growth factor: a canine study," *Acta oto-laryngologica*, vol. 130, no. 7, pp. 844–850, 2010.

[156] E. R. Conroy, T. M. Hennick, S. N. Awan, M. R. Hoffman, B. L. Smith, and J. J. Jiang, "Effect of variations to a simulated system of straw phonation therapy on aerodynamic parameters using excised canine larynges," *Journal of voice*, vol. 28, no. 1, pp. 1–6, 2014.

[157] B. W. O'Malley Jr, G. S. Weinstein, and N. G. Hockstein, "Transoral robotic surgery (tors): glottic microsurgery in a canine model," *Journal of Voice*, vol. 20, no. 2, pp. 263–268, 2006.

[158] M. Zañartu, D. D. Mehta, J. C. Ho, G. R. Wodicka, and R. E. Hillman, "Observation and analysis of in vivo vocal fold tissue instabilities produced by nonlinear source-filter coupling: a case study," *The Journal of the Acoustical Society of America*, vol. 129, no. 1, pp. 326–339, 2011.

[159] B. A. Pickup and S. L. Thomson, "Flow-induced vibratory response of idealized versus magnetic resonance imaging-based synthetic vocal fold models," *The Journal of the Acoustical Society of America*, vol. 128, no. 3, pp. EL124–EL129, 2010.

[160] Z. Zhang, J. Neubauer, and D. A. Berry, "Influence of vocal fold stiffness and acoustic loading on flow-induced vibration of a single-layer vocal fold model," *Journal of sound and vibration*, vol. 322, no. 1-2, pp. 299–313, 2009.

[161] Z. Zhang, "Characteristics of phonation onset in a two-layer vocal fold model," *The Journal of the Acoustical Society of America*, vol. 125, no. 2, pp. 1091–1102, 2009.

[162] P. R. Murray and S. L. Thomson, "Synthetic, multi-layer, self-oscillating vocal fold model fabrication," *JoVE (Journal of Visualized Experiments)*, no. 58, p. e3498, 2011.

[163] M. Manti, M. Cianchetti, A. Nacci, F. Ursino, and C. Laschi, "A biorobotic model of the human larynx," in *2015 37th Annual International Conference of the IEEE Engineering in Medicine and Biology Society (EMBC)*, pp. 3623–3626, IEEE, 2015.

[164] P. R. Murray and S. L. Thomson, "Vibratory responses of synthetic, self-oscillating vocal fold models," *The Journal of the Acoustical Society of America*, vol. 132, no. 5, pp. 3428–3438, 2012.

[165] R. Mittal, B. D. Erath, and M. W. Plesniak, "Fluid dynamics of human phonation and speech," *Annual Review of Fluid Mechanics*, vol. 45, pp. 437–467, 2013.

[166] J. Flanagan and L. Landgraf, "Self-oscillating source for vocal-tract synthesizers," *IEEE Transactions on Audio and Electroacoustics*, vol. 16, no. 1, pp. 57–64, 1968.

[167] K. Ishizaka and J. L. Flanagan, "Synthesis of voiced sounds from a two-mass model of the vocal cords," *Bell system technical journal*, vol. 51, no. 6, pp. 1233–1268, 1972.

[168] M. Hirano, "Morphological structure of the vocal cord as a vibrator and its variations," *Folia Phoniatrica et Logopaedica*, vol. 26, no. 2, pp. 89–94, 1974.

[169] B. H. Story and I. R. Titze, "Voice simulation with a body-cover model of the vocal folds," *The Journal of the Acoustical Society of America*, vol. 97, no. 2, pp. 1249–1260, 1995.

[170] M. de Oliveira Rosa, J. C. Pereira, M. Grellet, and A. Alwan, "A contribution to simulating a three-dimensional larynx model using the finite element method," *The Journal of the Acoustical Society of America*, vol. 114, no. 5, pp. 2893–2905, 2003.

[171] X. Zheng, S. Bielamowicz, H. Luo, and R. Mittal, "A computational study of the effect of false vocal folds on glottal flow and vocal fold vibration during phonation," *Annals of biomedical engineering*, vol. 37, no. 3, pp. 625–642, 2009.

[172] H. E. Gunter, "Modeling mechanical stresses as a factor in the etiology of benign vocal fold lesions," *Journal of biomechanics*, vol. 37, no. 7, pp. 1119–1124, 2004.

[173] Q. Xue, R. Mittal, X. Zheng, and S. Bielamowicz, "A computational study of the effect of vocal-fold asymmetry on phonation," *The Journal of the Acoustical Society of America*, vol. 128, no. 2, pp. 818–827, 2010.

[174] C. Laschi and M. Cianchetti, "Soft robotics: new perspectives for robot bodyware and control," *Frontiers in bioengineering and biotechnology*, vol. 2, p. 3, 2014.

[175] T. Ranzani, M. Cianchetti, G. Gerboni, I. De Falco, and A. Menciassi, "A soft modular manipulator for minimally invasive surgery: design and characterization of a single module," *IEEE Transactions on Robotics*, vol. 32, no. 1, pp. 187–200, 2016.

[176] S. Cantournet, R. Desmorat, and J. Besson, "Mullins effect and cyclic stress softening of filled elastomers by internal sliding and friction thermodynamics model," *International Journal of Solids and Structures*, vol. 46, no. 11-12, pp. 2255–2264, 2009.

[177] L. Mullins, "Softening of rubber by deformation," *Rubber chemistry and technology*, vol. 42, no. 1, pp. 339–362, 1969.

[178] J. Diani, B. Fayolle, and P. Gilormini, "A review on the mullins effect," *European Polymer Journal*, vol. 45, no. 3, pp. 601–612, 2009.

[179] R. W. Ogden, *Non-linear elastic deformations*.
Courier Corporation, 1997.

[180] M. Mooney, "A theory of large elastic deformation," *Journal of applied physics*, vol. 11, no. 9, pp. 582–592, 1940.

[181] R. Rivlin, "Large elastic deformations of isotropic materials iv. further developments of the general theory," *Philosophical Transactions of the Royal Society of London. Series A, Mathematical and Physical Sciences*, vol. 241, no. 835, pp. 379–397, 1948.

[182] R. Ogden, G. Saccomandi, and I. Sgura, "Fitting hyperelastic models to experimental data," *Computational Mechanics*, vol. 34, no. 6, pp. 484–502, 2004.

[183] A. Gent, "A new constitutive relation for rubber," *Rubber chemistry and technology*, vol. 69, no. 1, pp. 59–61, 1996.

[184] A. Gent, "Elastic instabilities of inflated rubber shells," *Rubber chemistry and technology*, vol. 72, no. 2, pp. 263–268, 1999.

[185] A. Gent, "Elastic instabilities in rubber," *International Journal of Non-Linear Mechanics*, vol. 40, no. 2-3, pp. 165–175, 2005.

[186] L. M. Kanner and C. O. Horgan, "Elastic instabilities for strain-stiffening rubber-like spherical and cylindrical thin shells under inflation," *International Journal of Non-Linear Mechanics*, vol. 42, no. 2, pp. 204–215, 2007.

[187] Y. Fu and Y. Xie, "Stability of localized bulging in inflated membrane tubes under volume control," *International Journal of Engineering Science*, vol. 48, no. 11, pp. 1242–1252, 2010.

[188] J. Rodríguez and J. Merodio, "A new derivation of the bifurcation conditions of inflated cylindrical membranes of elastic material under axial loading. application to aneurysm formation," *Mechanics Research Communications*, vol. 38, no. 3, pp. 203–210, 2011.

[189] A. Eriksson and A. Nordmark, "Instability of hyper-elastic balloon-shaped space membranes under pressure loads," *Computer Methods in Applied Mechanics and Engineering*, vol. 237, pp. 118–129, 2012.

[190] G. Mao, T. Li, Z. Zou, S. Qu, and M. Shi, "Prestretch effect on snap-through instability of short-length tubular elastomeric balloons under inflation," *international Journal of Solids and structures*, vol. 51, no. 11-12, pp. 2109–2115, 2014.

[191] S. Kyriakides and C. Yu-Chung, "The initiation and propagation of a localized instability in an inflated elastic tube," *International Journal of Solids and Structures*, vol. 27, no. 9, pp. 1085–1111, 1991.

[192] L. Hines, K. Petersen, and M. Sitti, "Inflated soft actuators with reversible stable deformations," *Advanced Materials*, vol. 28, no. 19, pp. 3690–3696, 2016.

[193] W. Sun, H. Wang, and J. Zhou, "Actuation and instability of interconnected dielectric elastomer balloons," *Applied Physics A*, vol. 119, no. 2, pp. 443–449, 2015.

[194] I. R. Titze, "Mechanical stress in phonation," *Journal of Voice*, vol. 8, no. 2, pp. 99–105, 1994.

[195] M. L. Fackler and J. A. Malinowski, "Ordnance gelatin for ballistic studies. detrimental effect of excess heat used in gelatin preparation.," *The American journal of forensic medicine and pathology*, vol. 9, no. 3, pp. 218–219, 1988.

[196] R. Schrieber and H. Gareis, *Gelatine handbook: theory and industrial practice*. John Wiley & Sons, 2007.

[197] eng.cam.ac.uk/, "International standard atmosphere." [Online; accessed 05-Nov-2019].

[198] T. Martonen, Z. Zhang, and R. Lessmann, "Fluid dynamics of the human larynx and upper tracheobronchial airways," *Aerosol science and technology*, vol. 19, no. 2, pp. 133–156, 1993.

[199] C. Andaloro and I. La Mantia, "Anatomy, head and neck, larynx arytenoid cartilage," in *StatPearls [Internet]*, StatPearls Publishing, 2019.

[200] H. Eckel, C. Sittel, P. Zorowka, and A. Jerke, "Dimensions of the laryngeal framework in adults," *Surgical and Radiologic Anatomy*, vol. 16, no. 1, pp. 31–36, 1994.

[201] M. A. Frable, "Computation of motion at the cricoarytenoid joint," *Archives of Otolaryngology*, vol. 73, no. 5, pp. 551–556, 1961.

[202] W. S. Selbie, S. L. Gewalt, and C. L. Ludlow, "Developing an anatomical model of the human laryngeal cartilages from magnetic resonance imaging," *The Journal of the Acoustical Society of America*, vol. 112, no. 3, pp. 1077–1090, 2002.

[203] I. R. Titze and E. J. Hunter, "A two-dimensional biomechanical model of vocal fold posturing," *The Journal of the Acoustical Society of America*, vol. 121, no. 4, pp. 2254–2260, 2007.

[204] E. J. Hunter, I. R. Titze, and F. Alipour, "A three-dimensional model of vocal fold abduction/adduction," *The Journal of the Acoustical Society of America*, vol. 115, no. 4, pp. 1747–1759, 2004.

[205] A. Hu, T. Wilson, H. Ladak, P. Haase, and K. Fung, "Three-dimensional educational computer model of the larynx: voicing a new direction," *Archives of Otolaryngology–Head & Neck Surgery*, vol. 135, no. 7, pp. 677–681, 2009.

[206] H. Hiramatsu, R. Tokashiki, M. Nakamura, R. Motohashi, T. Yoshida, and M. Suzuki, "Characterization of arytenoid vertical displacement in unilateral vocal fold paralysis by three-dimensional computed tomography," *European Archives of Oto-Rhino-Laryngology*, vol. 266, no. 1, p. 97, 2009.

[207] D. C. for Life Science, "Dbcls sra." `https://sra.dbcls.jp/`.
[Online; accessed 27-Sep-2020].